UNIVERSITY OF CALIFORNIA

SANTA CRUZ

THE DESIGN AND CONSTRUCTION OF A BIOMIMETIC PEROXYNITRITE-GENERATING PLATFORM: AN ANALYTICAL TOOL TO STUDY THE DYNAMIC CHEMISTRY OF PEROXYNITRITE

Dissertation submitted in partial satisfaction
of the requirements for the degree of

DOCTOR OF PHILOSOPHY

in

CHEMISTRY AND BIOCHEMISTRY

by

Tara Renee deBoer

June 2015

The Dissertation of Tara R. deBoer
is approved by:

_____
Professor Theodore R. Holman, Chair

_____
Professor Pradip K. Mascharak, Advisor

_____
Professor Scott R.J. Oliver

_____
Tyrus Miller
Vice Provost and Dean of Graduate Students

Table of Contents

Appendix B. Synthesis and Construction of Silver(I)-Carboxy-methyl Cellulose Dressings Designed for Trackable Therapeutic Release

List of Figures

Chapter 1.

Chapter 2

Figure 2.13. Plot illustrating the $O_2^{\bullet-}$ flux profile from XO-CAT•SG discs. Points shown were calculated based on the concentration of uric acid present at the corresponding time point. Aliquots of 100 μL were collected from a well of 24-well plate that contained a single XO-CAT•SG discs and 150 μM solution of hypoxanthine every 5 minutes.

Figure 2.14. Plot of corresponding data points collected from three independent wells that contain a single XO-CAT•SG discs and 250 μM solution of hypoxanthine. Each point represents a single aliquot taken at a given time from one of the three wells.

Figure 2.15. Prototype of the PN-generating platform constructed within the wells of a multi-well platform.

Figure 2.16. Mass spectra of collected samples where the $NO:O_2^{\bullet-}$ flux ratio in three adjacent wells within a first-generation PN-generating platform were modulated from 1:1 (top left), 2:1 (middle) and 1:2 (top right) and the corresponding chemical structures are highlighted in the bottom panel.

Chapter 3.

Chapter 4.

Chapter 5.

Appendix A.

Appendix B.

List of Tables

Chapter 2

Chapter 3

Chapter 5

Abstract

THE DESIGN AND CONSTRUCTION OF A BIOMIMETIC PEROXYNITRITE-GENERATING PLATFORM: AN ANALYTICAL TOOL TO STUDY THE DYNAMIC CHEMISTRY OF PEROXYNITRITE

Tara deBoer

Peroxynitrite is a reactive nitrogen species that has remained at the center of controversy since the time of its discovery in the early 1990's. The reactive nature of PN required unique chemical synthetic approaches and techniques to be developed to study the chemistry of this species. Unfortunately, many of these sources are highly alkaline, produce unwanted byproducts, and can be difficult to control. With these shortcomings in mind, a multi-well platform was designed and constructed that is capable of evolving sustained levels of peroxynitrite precursors nitric oxide and superoxide under controlled conditions. Nitric oxide and superoxide rapidly react in the wells of the platform to generate peroxynitrite *in situ*. This thesis describes the design process and construction of this biomimetic two-component peroxynitrite-generating system.

In Chapter 2 the fabrication and characterization of the platform is discussed in detail and concludes with results obtained were intrinsic platform probe uric acid was used to effectively demonstrate the control of the system. The work highlighted in Chapter 3 establishes the application of the platform through the use of PN-target tyrosine. Investigation into PN-mediated nitration of free tyrosine and tyrosine-containing model peptides within the wells of the platform revealed extents of

nitration (~40 %) significantly greater than values previously reported in the literature where alternative sources of PN were employed. Chapter 4 describes our first attempts to study an unexplored chemistry between peroxynitrite and 3-nitrotyrosine within the wells of the platform. Results from this work revealed a unique dimer product that was characterized by detailed mass spectral analysis.

Based on the results of Chapters 2, 3 and 4, the designed platform has been firmly established as a powerful bioanalytical tool. Recognizing this potential, Chapter 5 describes preliminary results observed in recent studies investigating the metabolites of selected anti-inflammatory drugs upon exposure to peroxynitrite and its precursors nitric oxide and superoxide. Descriptions of the results are presented with the intentions of establishing a future direction for the peroxynitrite-generating platform.

For my family…I love you, love you, love you

Acknowledgements

I first want to thank my PI, Distinguished Prof. Pradip Mascharak for molding me into the scientist that I am today. When I came into his lab five years ago I had a very fundamental knowledge of chemistry, but had no idea what it meant to be a researcher. He has guided me throughout this entire graduate program while at the same time allowing me to flourish into an independent scientist. *My mind and perspective has been forever changed*.

I would also like to thank my committer members Prof. Scott Oliver and Prof. Fitnat Yildiz. Thank you Scott for listening to so many of my talks in group meetings and being a sounding board for me throughout these years expanding my understanding of materials science. A special thank you to the chair of my committee, Prof. Theodore Holman. Thank you for always sharing your time and perspective with me.

One of the most important aspects of science that I have had the privilege learning over the year is the significant of collaboration. One of the overwhelming themes of my projects in the lab required just that. For without many of the individuals that have helped me along the way I would not have accomplished nearly as much as I have been able to. First, I want to thank Dr. Nicole Fry for her endless patience and kindness. I had no formal training in inorganic synthesis prior to entering the Mascharak group and Nicole selflessly shared as much of her knowledge as our time together permitted. I would also like to thank Angel Resendez for the countless hours he spent working on my projects when he could have been working on his own. He synthesized a peroxynitrite probe for me when I was at a critical point in the development of the platform and has also more recently synthesized standards for the ongoing projects. Without him I would have a lot more work.

Also, a very special thank you to Rafael Palomino who synthesized every model peptide that will be discuss in the upcoming chapters of my thesis. The luxury of having him just two doors down from me to synthesize any peptide that I felt was needed to prove my point has been just that…a luxury. I also want to thank Angel and Rafael for also being such great friends and colleagues. Their excitement for science and unconditional friendship has made me a better scientist. While on that not, I would also like to thank Mrs. Palomino for her great friendship and support over the last five years

I would also like thank two very important undergraduate workers that I have had the privilege of working, Vu La and Sharon Idiga. Vu played a critical role in shaping the peroxynitrite-generating platform into what it has become today. He joined me when I was just a lost first-year graduate student and he probably taught me much more than I taught him. Coming full-circle, I worked with Sharon at the end my graduate career and she has really helped push me over the speed bumps of graduate school that seem to be more like mountains in your last year. It was really fun watching her grow as a young scientist and I cannot wait to see what the future brings for her.

While I was able to pick my undergrads, I did not pick who I entered graduate school with. But, luck for me I was paired with a great group of young scientist. I want to thank my cohort for numerous hours of engaging science and non-science based conversations. Especially, Christopher Murphy, Lily Le, and Michelle Herrick for a million and one reasons.

I would also like to thank current and past Mascharak group members. Especially, Dr. Margarita Gonzales and Dr. Brandon Heilman for truly influencing the way and the rate at which I approach a scientific problem. Also a special thank you to Dr. Indranil Chakraborty for all of his time and efforts in solving many of my crystal structures.

I also need to thank the entire UCSC Chemistry and Biochemistry Department for letting me around the labs and halls as if they were an extension of my lab. Thank you to all of the professors for maintaining an open door policy. A special thank you to Prof. Bakthan Singaram for his shared knowledge and time. A special thank you to the Chen, Bogomolni, Millhauser, Singaram, and Holman labs for allowing me to use their instruments and space. I am sure there is not one lab that I have not worked with, so thank you to all.

Last but not least, I want to thank my friends and family for always believing in me and accepting me. To my friends Gina Portillo, Megan Trinta, Nicole Caldera, Lauren Hensely, and G Kaur thank you for your endless positivity and encouragement. I also thank Brazer Bozlak for reminding me of who I am. To my family, I thank my sister her for strength and for so many things that cannot be put into words. I thank Miguel for being just like me. I thank Zooey for being my ray of sunshine even in the dark. And I especially thank my parents and grandparents for showing me what hard work and sacrifice looks like.

Chapter 1. Introduction

1.1 Background

The physiological role of nitric oxide (NO) has been extensively investigated over the past three decades and shown to be rich and diverse.[1-5] While fundamental signaling cascades mediated by NO continue to develop and transform, its role in innate immune response and inflammation has descended towards a unique chemistry distinct from other physiological pathways.[6] This divergence is regulated by reactive oxygen species superoxide ($O_2^{\bullet-}$) and transforms the role(s) of NO in the body. Under physiological conditions, the concentration of $O_2^{\bullet-}$ is tightly regulated by superoxide dismutase (SOD) and NO is present in pM to nM concentrations. However, the presence of pathogens or initiation of inflammatory pathways trigger enhanced release of NO that outcompetes SOD and reacts with $O_2^{\bullet-}$ at a diffusion-limited rate to form the reactive nitrogen species peroxynitrite (PN).[6,7] This reactive species directs oxidation and nitrosation of biomolecules and was initially believed to elicit purely cytotoxic responses in the body.[8,9] However, further exploration into the chemistry mediated by PN has exposed diverse and selective chemical modifications to lipids, proteins, and nucleic acids that have introduced the potential of this reactive species as a signaling counterpart of NO under explicit conditions of inflammation.[6] A loss or lack of control over the process of inflammation quickly transforms the effects of PN from cytoprotective (and regulator) to cytotoxic and perpetuating oxidation. The following sections will discuss the chemistry of PN with contrast to precursor NO and $O_2^{\bullet-}$ when required, because to understand the selective and

distinct chemistry of PN one must first understand the chemistry of its robust signaling counterpart NO.

1.2 Nitric Oxide

Nitric oxide is an uncharged odd electron gaseous molecule generated enzymatically in mammals by a family of Nitric Oxide Synthases (NOSs) that require oxygen and NADPH. There are three principal isoforms of NOS in our body, two constitutive forms (eNOS and nNOS) that associated with the plasma membrane in cells and generate pico- to nanomolar concentrations of NO (0.63 μmol kg^{-1} h^{-1}), and one inducible form (iNOS) that is known to be unregulated in macrophages and neutrophils to generate micromolar levels of NO.[10-12] The concentration and location of NO generation strongly dictates the cell signaling pathways induced by this gasotransmitter. However the electronic features of NO restrict its reaction to metal centers and molecules containing unpaired electrons (such as molecular oxygen or radical species).[13] While the prior reactions account for the majority of physiological responses mediated by NO, the primary focus of the proceeding work is related to the reactions of NO with O_2 and its reactive counterpart $O_2^{\bullet-}$.

The molecular orbital diagram of NO is shown in Figure 1.1 in contrast to those of molecular nitrogen and oxygen to highlight the electron configuration of the frontier orbitals. The bond order of N_2, NO, and O_2 are 3, 2.5 and 2 respectively, of NO (Figure 1.1).[13] It is the single electron in the π* orbital that contributes to the significant affinity of this species towards metal centers (even greater than that of O_2 and CO), showing highest affinity towards ferrous iron (Fe(II)). Direct reaction of NO

with the low-spin Fe(II) center of ubiquitous heme-containing enzyme souluble guanylyl cyclase (sGC) represents the primary signaling mechanism of NO in the body.[14-16] Coordination of NO to the metal center induces conformational modification of cGC that ultimately perpetuates a cascade of chemical signals that yield a physiological affect.[17] In contrast to the nitrosylation of enzymatic metal centers, reactions between NO and oxygen species yields secondary radicals and ions capable of inducing a broad spectrum of chemical modifications of lipids, nucleic acids, and proteins/enzymes.[13]

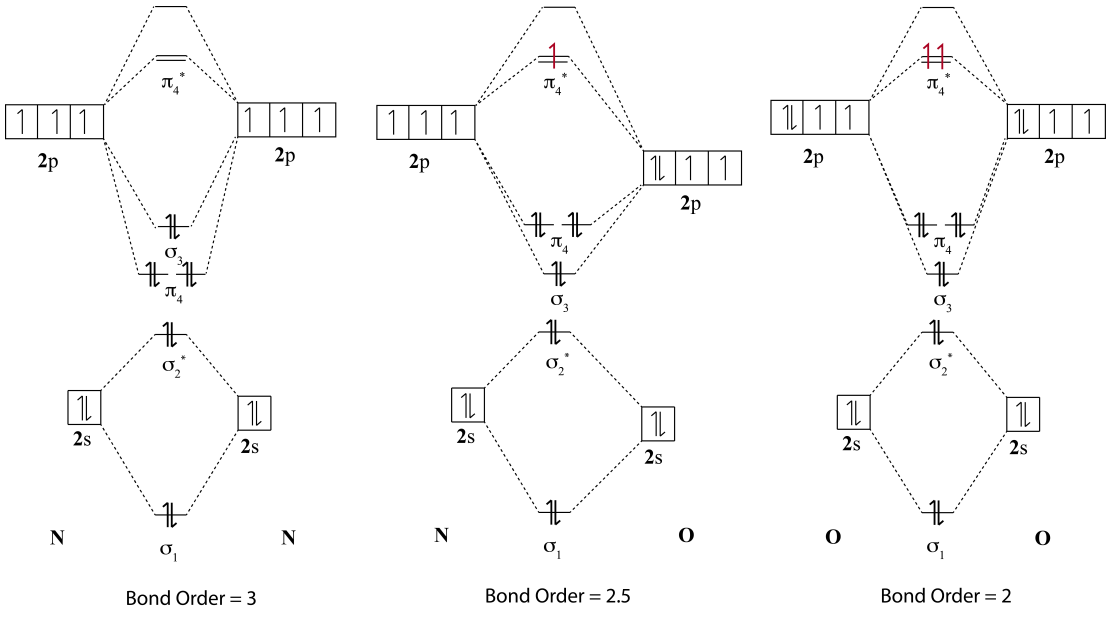

Figure 1.1. Molecular orbital diagrams of N_2 (*far left*), NO (*center*) and O_2 (*far right*) with the respective bond orders listed bellow the corresponding diagram.

1.2.1 Reactions of Nitric Oxide with Molecular Oxygen

In general, direct chemistry of NO is scarce because bonding to NO requires a molecule have an available unpaired electron (located with an orbital of appropriate symmetry and energy) to pair with the single electron of NO.[18] This requirement limits the number of biomolecules suitable for effective bonding with NO. Interestingly, NO itself does not fulfill this requirement because combination of two NO molecules (O=N−N=O) does not result in increased bond order compared to 2 free molecules. NO remains in its complete dissociated form at room temperature. However, O=N−N=O can be trapped at liquid nitrogen temperature and observed as a vibrant blue solid.[19]

The redox properties of NO also contribute to a general lack of reactivity.[13,20] The potentials of reduction or oxidation of NO under physiological concentrations and conditions are mostly biologically inaccessible in biology (Figure 1.2). While the seemingly inert nature of NO could raise question as to how this molecule acts as an important signaling molecule in the body, it is this passive character that establishes NO as potent and selective trigger in mammalian physiology. Under precise and coordinated conditions the chemistry of NO can expand through reaction with molecular oxygen to yield secondary species capabable of inducing nitrosylation at non-metal centers. Two such nitrosylating species, namely nitrogen dioxide ($^{\bullet}NO_2$) and dinitrogen trioxide (N_2O_3) are shown in Figure 1.3. Cysteine nitrosylation is an indirect NO-mediated post-translational modification. This reaction has been hypothesized

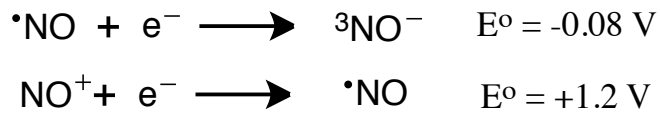

Figure 1.2. Oxidation and reduction reactions of NO with respective redox potential values (vs NHE).[13]

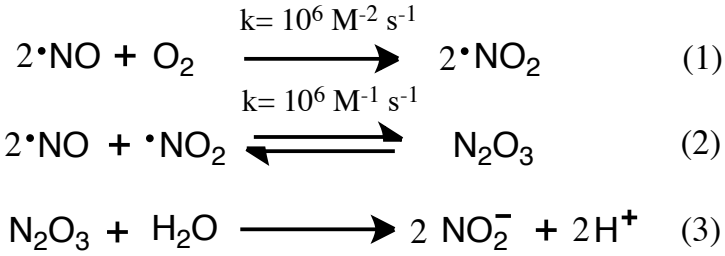

Figure 1.3. Chemical reactions associated with autooxidation of NO.

to be a biological signaling pathway within the body, parallel to phosphorylation.[21] The addition of a single nitroso group (N=O) to a cysteine residue can modify the electrostatic of a protein, modulating its activity. The mechanism of cysteine nitrosylation has been proposed to proceed through one of two pathways (Figure 1.4).[22,23] In the first, moderate oxidant $^{\bullet}NO_2$ reacts with the thiol/thiolate group of cysteine to form a thiyl radical that can then react in a radical terminating reaction with NO to yield S-nitrosylated cysteine (Cys-SNO). While in the second, nitrosating agent N_2O_3 is formed and homolytically cleaves along the N-N bond to from nitrosonium (nitrating unit, NO^+) and nitrite (NO_2^-), ultimately yielding Cys-SNO.

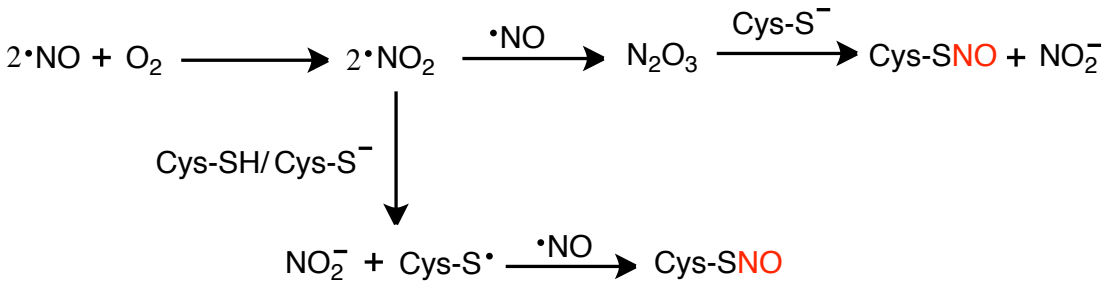

Figure 1.4. Cysteine nitrosylation pathways mediated by NO.

Nitrosylation of thiols is the principal metal-free signaling pathway mediated by NO. However, unlike signaling pathways mediated by phosphorylation this post-translational modification has been described as *prototypic redox-based signal*.[23] And, similar to the direct chemistry of NO (with metal centers) this indirect pathway exhibits a level of selectivity because only select thiol groups seem to be susceptible to such modifications.

1.2.2 Reactions of Nitric Oxide with Superoxide

While the reaction between NO and O_2 proceeds a reasonable rate ($k = \sim 10^6\ M^{-1}\ s^{-1}$),[13,18] this reaction and the chemistry associated with the secondary products formed are essentially absent in the presence of superoxide $O_2^{\bullet-}$. This free radical reacts at a diffusion-limited rate with NO to form peroxynitrite (PN, Figure 1.5). In contrast to O_2-dependent chemistry of NO, $O_2^{\bullet-}$-dependent chemistry is most commonly associated with inflammatory processes of the body.[6] It is for this reason that the remainder of the discussion will be focused around PN formed under conditions of inflammation.

The onset of inflammation, regardless of the trigger, is initiated with rapid recruitment of inflammatory cells such as macrophages and neutrophils that contain the essential machinery required to generate PN precursors NO and $O_2^{\bullet -}$.[24] NO is generated by Ca^{2+}-independent NOS isoform iNOS that generates sustained levels of NO (μM), in contrast to its constitutive isoforms that release NO under the strict regulation of Ca^{2+}.[11] Such variation suggests that iNOS acts as a pure source of NO. Similarly, NADPH oxidase (NADPHox), is a membrane-bound protein located in the plasma membrane of neutrophils, that transfers a single electron from NADPH to oxygen to generate $O_2^{\bullet -}$ at μM levels.[25] Evidence of PN formation *in vitro* was first revealed by Ischiropoulos *et. al.*, who reported rates of 0.11 nmol·10^6 cells^{-1}·min^{-1} of

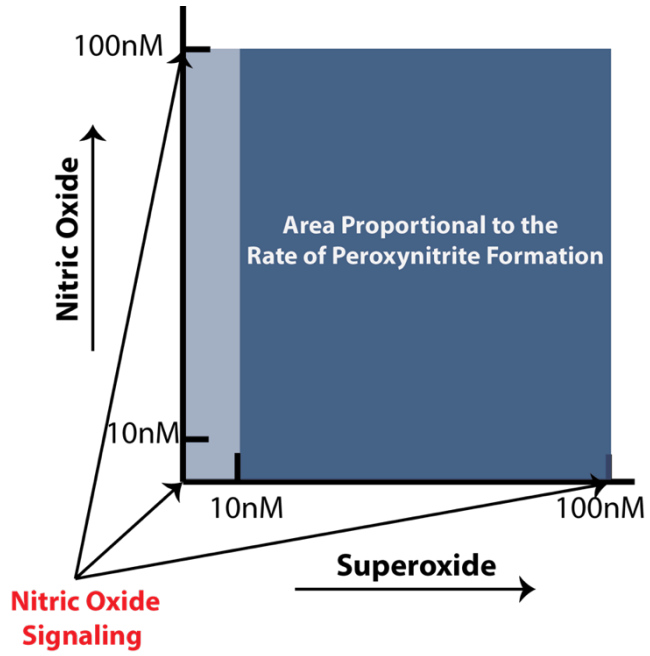

Figure 1.5. Graphical depiction describing the rate of PN formation based on the concentrations of NO and $O_2^{\bullet -}$ generated. The shaded areas represent the rate of PN formation, with the *light blue* representing physiological conditions and the *dark blue* representing inflammation.

PN from alveolar macrophages by activating the respective NO and $O_2^{\bullet-}$ sources.[26]

The radical terminating reaction between NO and $O_2^{\bullet-}$ is essentially irreversible with a ΔG equivalent to the hydrolysis of 2 ATP molecules.[19] Molecular orbital representations shown in Figure 1.6 illustrate the electronic interactions between the frontier orbitals (singly occupied molecular orbitals, SOMO, and highest occupied molecular orbitals, HOMO's). Bonding between the unpaired electrons of the π* orbitals of NO and $O_2^{\bullet-}$ yields a σ-bond between N and O atoms. Characterization of PN in solid and gaseous states by Raman spectroscopy and computational modeling, predict two rotamers species, each with 6 distinct vibrational modes.[27] The *cis* conformer is presumed to comparatively more stable than the *trans* because in the *cis* form the π*-orbitals of the terminal O of the $O_2^{\bullet-}$ unit overlap with the π*-orbitals of the terminal O in the NO unit to form a partial bonding π orbital (comparable to energy of H-bonding) in addition to the σ-bond between the N and O. This π-bonding orbital is absent in the molecular orbitals of the *trans* rotamer and instead contains a π*-orbital that contributes to a destabilization of the N-O bond.[28]

The electronic profiles of the two rotamers result in distinct chemical properties and explain the significantly low pK_a of the *cis* conformer (6.8), which is the lowest of any peroxide-containing molecules (pK_a of *trans*-PN reported to be 7.8).[19] Stability of *cis*-PN further contributes to a large energy barrier required for isomerization to *trans*-PN (36 kcal mol^{-1}, Figure 1.6). However, protonation of anionic PN to peroxynitrous acid (ONOOH) decreases the energy barrier from ~22 kcal mol^{-1} to approximately ~12 kcal mol^{-1}.[19]

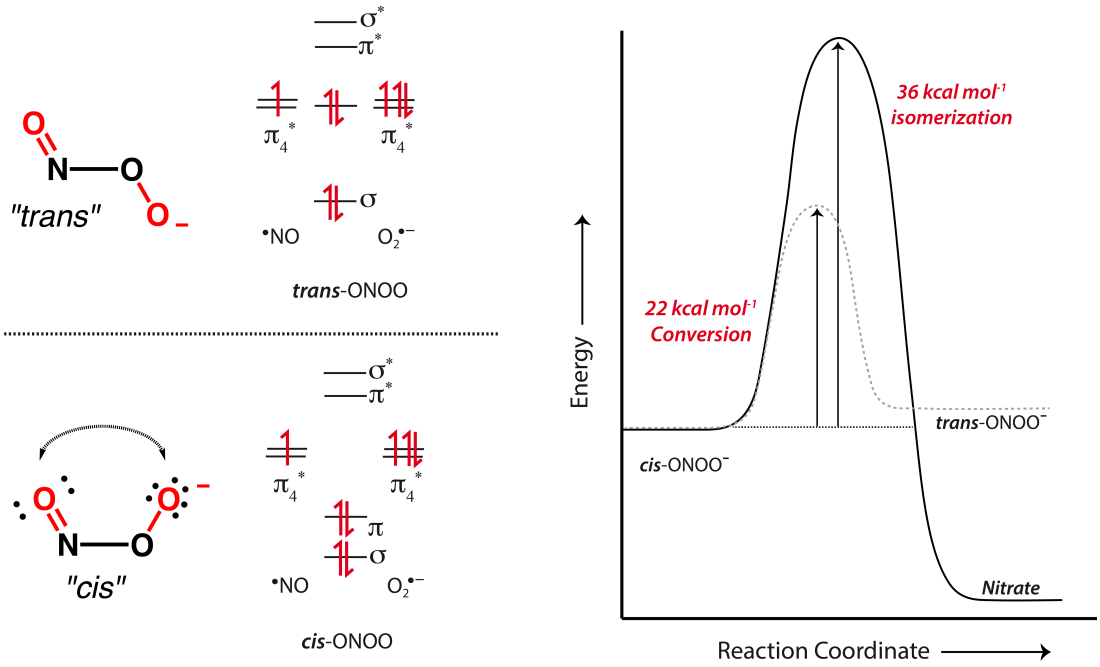

Figure 1.6. Molecular orbital representation of the frontier orbitals of NO and $O_2^{\bullet-}$ that combine to form the molecular orbitals of PN shown on the *left* and the energy diagram with representative energy barriers associated with isomerization of PN to nitrate and conversion of *cis*-PN to *trans*-PN shown on the *right*.

1.2.3 Peroxynitrite: *Direct* Reactions

While PN has been established as the reactive counterpart of NO this "reactive" nitrogen species reacts directly with bimolecules at a slow rate. Similar to NO, the chemistry of PN can be divided into two varieties: *direct* and *indirect*. Targets known to react directly with PN include sulfur containing amino acids, Fe-S clusters and Zinc fingers.[6] Such reactions proceed through one- and/or two- electron oxidation pathways. Reaction of PN with S-containing amino acid methionine (Met-S-CH_3) can yield both one- and two-electron products ethylene ($H_2C{=}CH_2$) or methionine

sulfoxide derivative Met-S(O)-CH_3.[29,30] Similarly reactions of PN with cysteine proceed through one- (via anionic peroxynitrous acid, ONOOH) and two-electron oxidation processes (via anionic PN) to yield sulfenic acid (R-SOH, Figure 1.7, where R represents the cysteine residue).[31-33] Results reported by Quijano *et. al*. established that pH strongly influence the incidence of one- or two-electron cysteine oxidation.[25] In this work it was shown that under alkaline conditions PN, predominately in its anionic form, oxidizes cysteine by a two-electron pathway that yields R-SOH and nitrite (NO_2^-) based on an absence of observed thiyl radical formation and minimal O_2 consumption. R-SOH is a relatively unstable oxidation product that can undergo further oxidation to yield cysteine (R-S-S-R), sulfenic acid (R-SO_2H) and sulfonic acid (R-SO_3H).[34] While under physiological to slightly acidic pH, cysteine was shown to undergo a one-electron oxidation that ultimately resulted in a relative decrease in thiol oxidation. This single electron oxidation process was based on observable thiyl (R-S$^\bullet$) and $^\bullet NO_2$ formation and increased O_2 consumption. Formation of $^\bullet NO_2$ under neutral/acid conditions was predicted because ONOOH, predominant under such conditions, has been hypothesized to form an intermediate state (ONOOH*) that can be described as a caged radical state [$OH^\bullet \cdots {}^\bullet NO_2$]*.[19,36,37] However, while the product profile upon reaction of cysteine with PN is rich and diverse, the rate of these reactions are only on the 10^3 order of magnitude (1.29 x 10^3 $M^{-1}s^{-1}$ reported for cysteine), [32] making them less likely substrates of PN under physiological conditions.

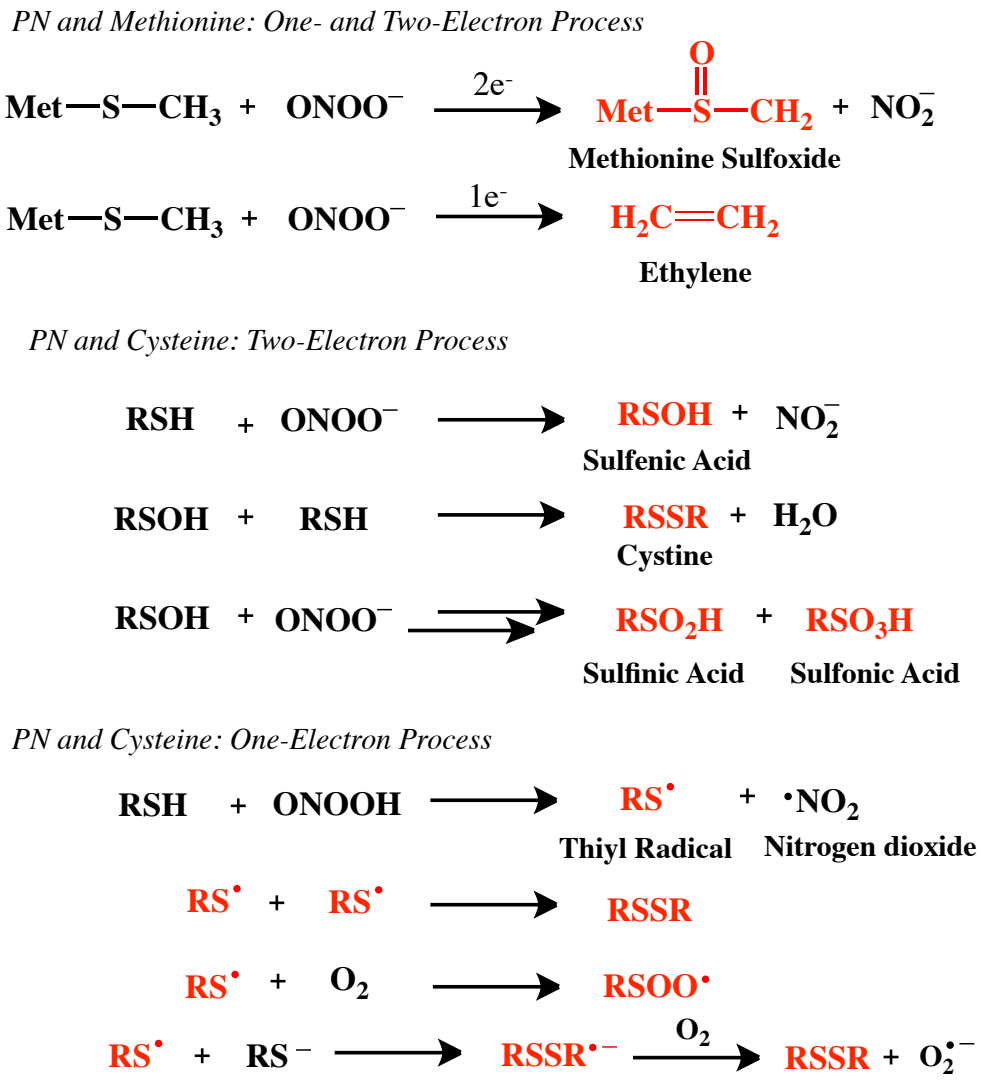

Figure 1.7. Reactions and corresponding products between S-containing amino acids methionine and cysteine (represented as R) with PN.

Additional targets known to react *directly* with PN includes are Zinc fingers and Fe-S clusters. While PN primarily reacts with thiolate ligands coordinating the Zn center of Zn finger through pathways aforementioned,[38] PN reacts directly with Fe center of Fe-S clusters.[6,39] In Fe-S clusters of the type $[4Fe{-}4S]^{2+}$, PN oxidizes the cluster such that an unstable oxidation product $[4Fe{-}4S]^{3+}$ is formed. To compensate

for oxidation, one ferrous iron is released and a resulting in a $[3Fe{-}4S]^{1+}$ unit (Figure. 1.8). As expected, degradation of the Fe−S clusters imposes deleterious affects on the activity of the protein or enzyme to which the metal cluster is located within. While a cubic Fe-S cluster (namely $[4Fe{-}4S]^{2+}$) was given as an example, rhombic clusters are susceptible to similar pathways.

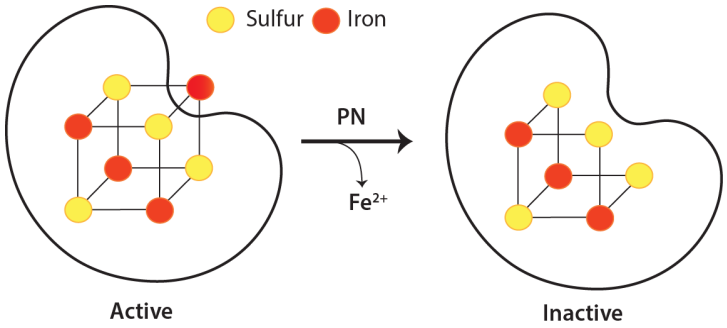

Figure. 1.8. Schematic of PN-mediated degradation of a cubic Fe-S cluster.

1.2.4 Peroxynitrite: Secondary Radical formation for *Indirect* Reactions

Interestingly, the biological targets susceptible to direct reaction with PN are also targets of NO. In fact, many of them are more sensitive to NO-mediated chemistry. In contrast, biotargets such as tyrosine and lipids that are modified through *indirect* pathways afford unique and characteristic products exclusive to PN.[40,41] The indirect reactions of PN are directed by secondary radical species $^{\bullet}OH$, $^{\bullet}NO_2$, and $CO_3^{\bullet-}$ (hydroxyl radical, nitrogen dioxide, and carbonate radical, respectively, shown in Figure 1.9) that are significantly more reactive than PN and NO.[6,42,43] The indirect chemistry and secondary players of PN are strongly dependent upon pH and CO_2 concentrations.

The spectrum of PN-derived species as a function of pH is quite diverse. Because the pK_a of PN (6.8) lies below the physiological pH, the ratio of peroxynitrous acid (ONOOH) to its conjugate base ($ONOO^-$) is strongly dependent on the local pH.[44] As observed in the PN-mediated modification of cysteine, both $ONOO^-$ and ONOOH exhibit unique chemical properties and initiate distinct chemical pathways. The relative ratios of $ONOO^-$ to ONOOH over a physiologically relevant pH range are shown in Figure 1.9. Values are reported in percentages, with the percent of $ONOO^-$ shown in red and the percent of ONOOH shown in blue. Under physiological conditions $ONOO^-$ predominates. This species can mediate divalent redox reactions, as discussed above, or react with carbon dioxide (CO_2) to generate intermediate species nitrosoperoxo-carbonate anion ($ONOOCO_2^-$).[44,45] This intermediate can homolytically cleave along the peroxo bond ($ONO\text{-}OCO_2$) to yield the strong oxidant $CO_3^{\bullet-}$ and the nitrating agent $^{\bullet}NO_2$.[46,47] Together these secondary radicals combine to orchestrate PN-mediated nitration reactions most commonly utilized as markers and indicators of PN formation in the body.

Under conditions of inflammation when the pH of local tissue can drop below 7.4, the ratio of $ONOO^-$ to ONOOH shifts towards unity. Compared to the chemistry of $ONOO^-$, the chemistry of ONOOH is much less diverse. Approximately 30% of ONOOH undergoes homolytic cleavage along the peroxo bond (ONO-OH) to yield reactive radicals hydroxyl radical ($^{\bullet}OH$) and $^{\bullet}NO_2$. However, based on the stability of $ONOO^-$ relative to ONOOH, increased abundance of ONOOH can also correlate to diminished PN reactivity.[47,48]

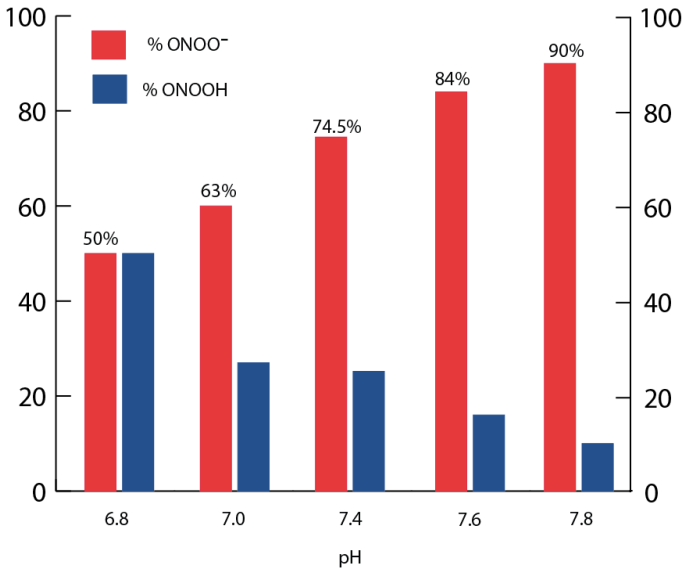

Figure 1.9. Bar plot highlighting the percentage of $ONOO^-$ or ONOOH as a function of pH.

While $^{\bullet}OH$ is a highly reactive oxidant, it indiscriminately reacts with biomolecules making its net oxidation impact minimal.[46,48] Because $^{\bullet}NO_2$ is also a product of ONOOH homolysis, this pathway also represents an option for PN-mediated nitration. However, this species can also act as an oxidant (Figure 1.10). The chemistry unique to PN most commonly proceeds through *indirect* pathways and yields distinct and characteristic products unlike non-specific oxidants such as $^{\bullet}OH$, the proceeding sections will highlight biotargets known to undergo selective modification by the secondary radicals of PN.

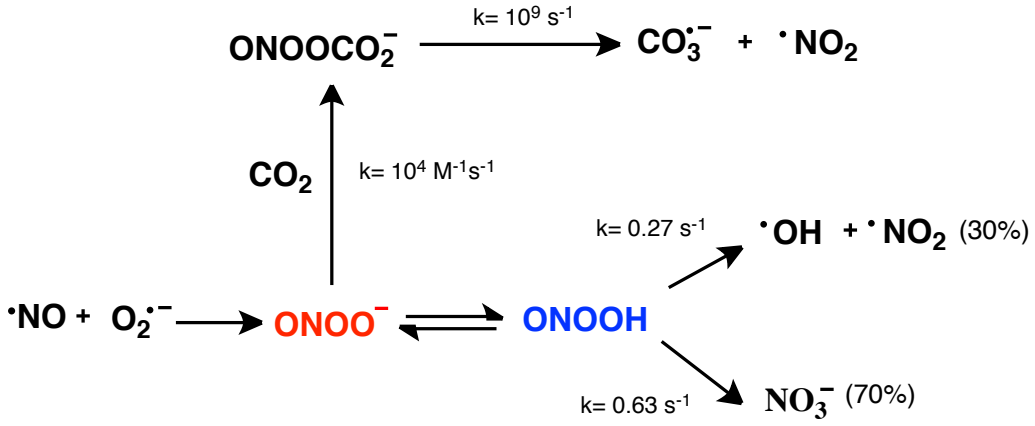

Redox Potentials of PN and its Seconday Radicals

$ONOO^{\bullet} \longrightarrow ONOO^{-}$ $E^{o} = 0.40\ V$

$^{\bullet}OH, H^{+} \longrightarrow H_2O$ $E^{o} = 2.31\ V$

$CO_3^{\bullet-}, H^{+} \longrightarrow HCO_3^{-}$ $E^{o} = 1.78\ V$

$^{\bullet}NO_2 \longrightarrow NO_2^{-}$ $E^{o} = 1.04\ V$

Figure 1.10. Reaction schematic showing the secondary products of PN that mediate *indirect* pathways. The respective redox potential of the secondary species are shown below.[13]

1.2.5 Peroxynitrite: Nitration and Oxidation Through *Indirect* Pathways

Nitration has become a signature of PN chemistry in the body. In fact, this post-translation modification was critical in establishing PN as a reactive product formed between NO and $O_2^{\bullet-}$.[40,41,49,50] Since this report in the early 1990's, both PN and tyrosine nitration have been studied together as a potential deleterious effect of NO. However decades of work have revealed the potential of this modification as a signaling modality analogous to that of phosphorylation.

The nitration of tyrosine by PN has been shown to be a highly selective modification that mediates both inactivation and enhancement of target biomolecule activity.[49,50] The apparent selectivity of this process was realized even in early studies attempting to simply identify this chemical modification. For example, work reported by McMillian-Crow *et. al.* showed that only three of nine tyrosine residues (Y34, Y45, and Y193) of manganese SOD (Mn-SOD) were susceptible to PN-mediated nitration.[51] Important to note that exposure of MnSOD to nitrating agent tetranitro-methane (TNM) caused nitration at all nine tyrosine residues. Y34 was observed to by the most prone to nitration and incidentally was found to be located within the active site of Mn-SOD, while other solvent-exposed tyrosine residues were found to be insensitive to PN-mediated nitration. This example is only one of many. It is this feature of PN that has raised interest in tyrosine nitration as a signaling possibility. However current work dedicated to identifying a de-nitration pathway is believed to be the missing key that will catapult this possibility into actuality. Additional proteomic work is currently underway to determine whether sequence and/or characteristic motifs direct nitration of particular tyrosine residues.

In general tyrosine pose as an ideal target of PN because it remains one of the few amino acid residues that can act as a redox centers capable of assisting in enzymatic catalysis and energy transfer processes through biostructures. Photosystem II, cytochrome *c* oxidase, and related oxygen reductases all employ tyrosine and its oxidant counterpart tyrosyl radical (Tyr-OH/ Tyr-O$^{\bullet}$) as a redox couple.[52] Similarly, the secondary radicals of PN ($^{\bullet}OH$, $^{\bullet}NO_2$, and $CO_3^{\bullet-}$) initiate nitration of tyrosine

through the oxidation of Ty-OH to from Tyr- O$^{\bullet}$. For this reason CO_2 has been shown to greatly enhance the extent of PN-mediated nitration; reaction of PN with CO_2 yields $ONOOCO_2^-$ that can homolyze to yield strong oxidant $CO_3^{\bullet -}$. However, similar to the reactive intermediate states proposed for the hemolysis along the peroxo bond of ONOOH, $ONOOCO_2^-$ has been proposed to react through a trapped state yielding nitration of tyrosine in a concerted fashion.[19,53] While this concerted state is most commonly depicted as complete homolysis that yields discrete $^{\bullet}NO_2$ and $CO_3^{\bullet -}$ radicals for simplification, two mechanistic pathways of nitration have been proposed

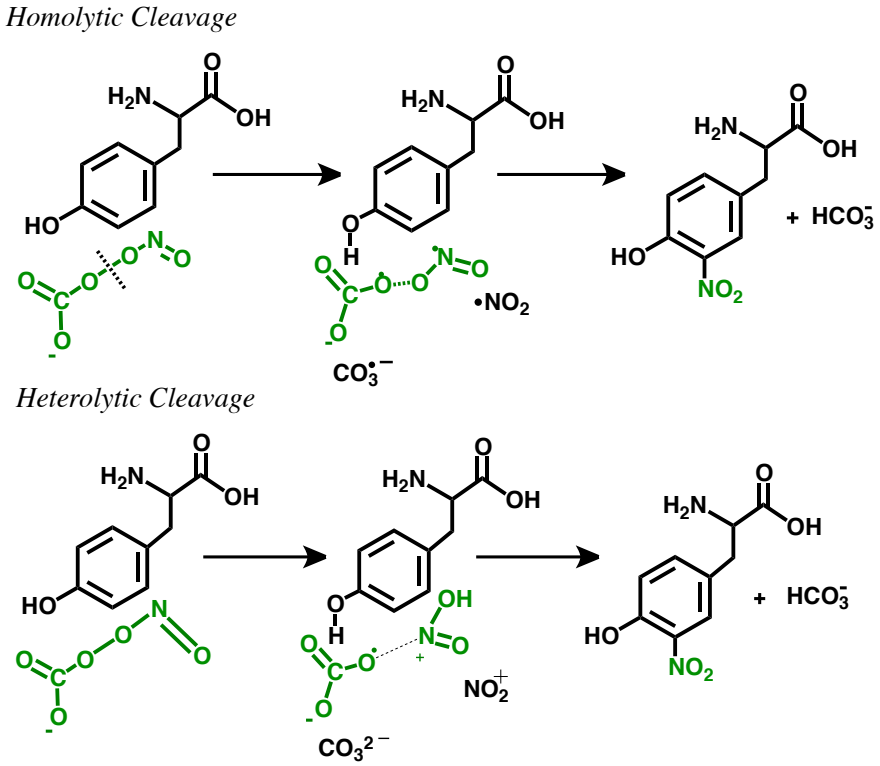

Figure 1.11. Reaction schematic illustrating the two proposed pathways of nitration mediated by $ONOOCO_2^-$.

that vary only in the decomposition of $ONOOCO_2^-$. The first predicts a more direct radical-radical interaction where homolytic cleavage of $ONOOCO_2^-$ along the peroxo O-O bond yields $^{\bullet}NO_2$ and CO_3^{2-}. The second proposed mechanism suggests a rearrangement event of $ONOOCO_2^-$ to the nitrocarbonate anion $O_2NOCO_2^-$ that yields nitrosyl cation (NO_2^+) and carbonate anion (CO_3^{2-}) via a heterolytic cleavage of the intermediate species.[19,25] Nitration of tyrosine yields 3-nitrotyrosine that has distinctly different physicochemical properties compared to tyrosine that ultimately results in the modulation of local structures and global protein/enzyme activity. The chemistry and effects of PN-mediated tyrosine nitration are discussed in more detail in chapter 3.

In addition to nitration, tyrosine can also undergo oxidation by PN to yield the dimer *o*,*o*'-dityrosine. Because this product is not exclusive to PN it will not be discussed in more detail. However it should be noted that formation of *o*,*o*'-dityrosine has been most notably observed in PN studies where the concentration of tyrosine is in great excess of PN (or low fluxes the reactive species are being generated).[54] While such conditions favor this dimerization event, product formation remains modest to minimal. In fact, our work has shown that tyrosine nitration is by far the favored product upon exposure of tyrosine to PN, and *o*,*o*'-dityrosine is only a mere byproduct. PN-mediated nitration of tyrosine has maintained the interest of the science community for many decades, but lipid nitration has more recently emerged as an equally powerful signaling option.

Unlike tyrosine, lipids are susceptible to both oxidation and nitration upon exposure to PN and such reactions afford a much more diverse product profile.[55,56] Polyunsaturated fatty acids (PUFAs) are the most susceptible to PN oxidation and can result in the formation of reactive lipid species that act as cell signaling molecules to mediate cellular inflammatory pathways. The general reactivity of PUFAs towards oxidation can be attributed to the *bis*-allylic protons of the methylene group(s) present between π-bonds.[33] Oxidation of PUFAs is initiated with a proton (-H) abstraction from a methylene carbon to yield an allylic radical. Resonance stabilization along the two π-bonds and methylene carbon offers multiple options for chemical additions along the PUFA chain, as highlighted by red asterisks in Figure 1.12.

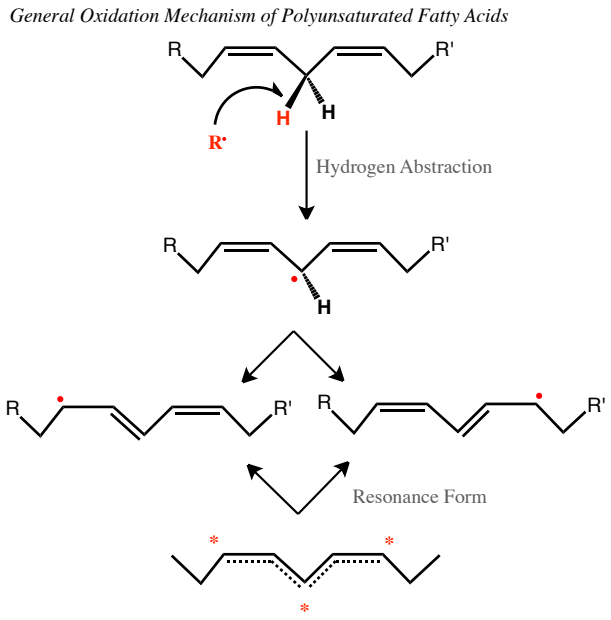

Figure 1.12. Schematic showing the general oxidation process of PUFA's, where R represents a generic oxidant source that yields a resonance stabilized allylic radical species.

Contrasting to all other PN-mediated modification discussed above, modifications of lipids by PN occur under local hydrophobic conditions, namely in the plasma membrane of cells. Interestingly, the chemistry of NO, O_2, $O_2^{\bullet -}$ and PN within the membrane can be considered comparatively more diverse than aqueous cellular milieu because the lifetime of radicals are extended in lipophilic environments due to a relatively lower abundance of antioxidants compared to the cytosol.[57]

Early work in the area of lipid signaling was focused on the chemistry of NO and O_2. Because NO is 10 times more soluble in hydrophobic milieu and non-poplar uncharged diatomic O_2 is also present in higher concentrations relative to aqueous media, autooxidation of NO in lipid membranes produces sufficient concentrations of $^{\bullet}NO_2$. This oxidant and nitrating species can react with lipids to form nitroalkenes via radical mechanism (Figure 1.13), although electrophilic mechanisms have also been proposed.[58]

Similar to the addition of a nitro group to the phenol moiety of tyrosine, nitration of PUFAs alters the chemical properties and reactivity of a lipid. Nitrated unsaturated fatty acids are potent electrophiles that are capable of undergoing reverse nitroalkylation reactions through Michael additions to form carbon-carbon and carbon-heteroatom bonds.[59] β-nitroalkyl radical has also been identified as a predominant species susceptible to such modifications (Figure 1.13).[57] Nitroalkenes and reactive radical lipid species react with nucleophilic thiols and amino acids residues of proteins (and glutathione). These electrophilic adducts act as *tags* that initiate redox-sensitive pathways, highlighted in Figure 1.13.[57]

Nitrogen Dioxide-Mediated Nitration

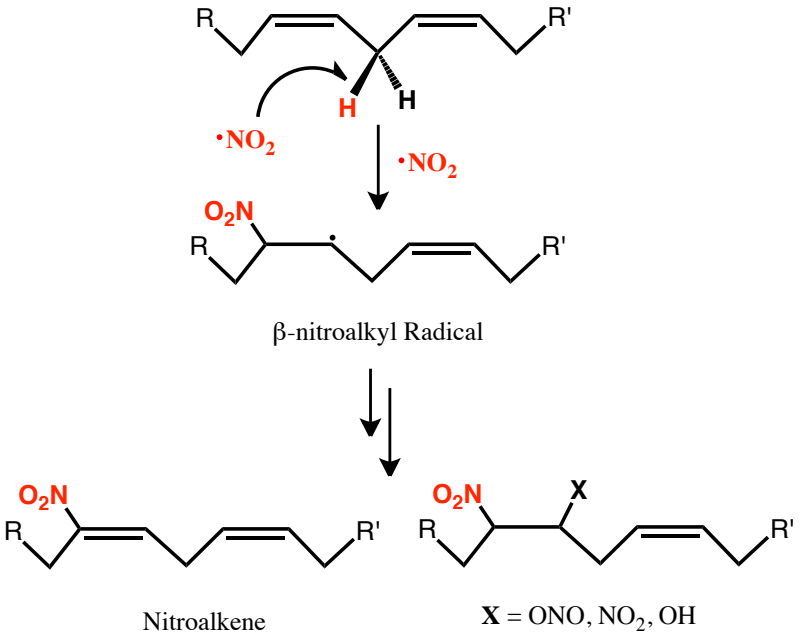

Figure 1.13. Radical mechanism between PUFA and $^{\bullet}NO_2$ that yields reactive nitroalkene lipids and β-nitroalkyl radical species.

Under ischemic and inflammatory conditions where oxygen tension can decrease and $O_2^{\bullet-}$ and NO production are enhanced, PN can also mediate formation of nitroalkenes and β-nitroalkyl radical. In contrast to tyrosine nitration, there is a lack of CO_2 dependence on the nitration of fatty acids suggesting a ONOOH-directed pathway. However, secondary radicals of PN that may form at the surface of membrane are capable of diffusing into the lipophilic membrane and may also contribute to lipid oxidation and nitration.

While oxidized fatty acids are strongly associated with cellular injury, nitration of lipids to form nitroalkenes have been linked to dynamic signaling events. Examples of the signaling action of nitroalkenens include cGMP-dependent vasorelaxation,[60]

upregulation HO-1,[61] inhibition of NF-κB,[62] PPAP activation,[63] and Keap1/Nrf2 activation.[64] The general effects of these signaling actions are aimed at controlling inflammatory responses. In fact, nitroalkenes have also been reported to inhibit inflammatory cell function. Most notably, nitroalkenes act to presumably attenuate PN production through inhibition of $O_2^{\bullet -}$ production in neutrophils and down-regulation of iNOS expression in activated macrophages.[65] Together these signaling features illuminate the truly intricate and dynamic role NO, O_2, $O_2^{\bullet -}$, and PN in the body. Under inflammatory conditions all factors, including their secondary products, work closely together to maintain balance.

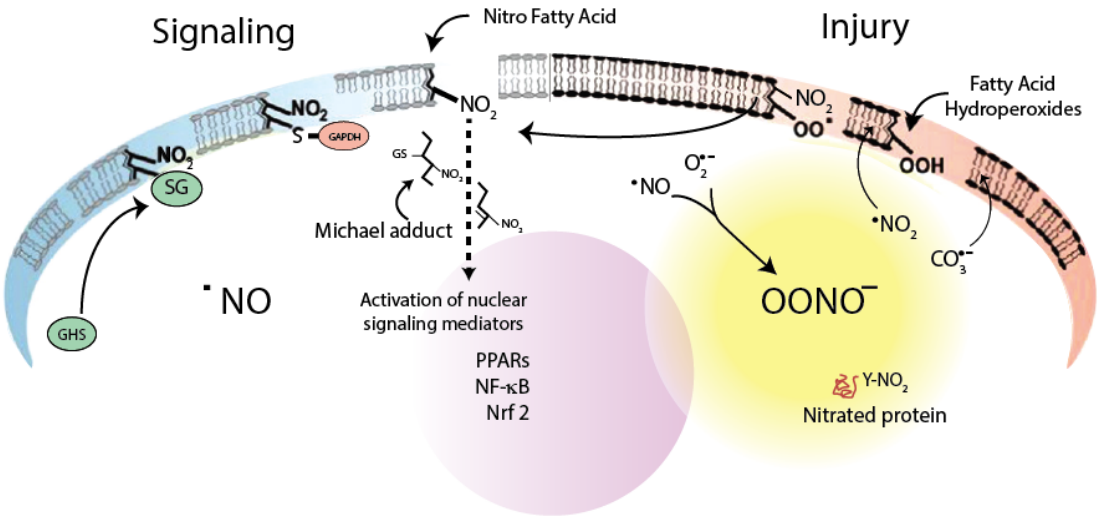

Figure 1.14. Schematic representation of *signaling* and *injury* pathways mediated by NO and PN. Under physiological conditions NO predominantly dictates the nitration of fatty acids that can then facilitate "signaling" cascades such as cGS-dependent vasodilation. Inflammatory conditions induce the formation and release of nitroalkenes that act to balance inflammatory responses through pathways such as Nrf-2 that initiate transcription of the antioxidant response elements (ARE) pathway.

1.3 Direction of Research

In the preceding sections the dynamic nature of PN has been described. Under no circumstances does PN exist in the body without the presence of NO, O_2, or $O_2^{\bullet-}$. However for many decades now PN has been studied as though it is a discrete individual species. Initial advances in this area utilized creative synthetic sources of PN to elicit and study the chemistry of this reactive nitrogen species. The synthetic methods employed in these early years of research were innovative and insightful, and elucidated fundamental chemical properties of PN. However, transition from purely chemical-based investigations to biochemical studies illuminated technical gaps associated with synthetic PN sources. The goal of the current thesis is to address this technological gap through the design and construction of a platform capable of evolving sustained levels of NO, $O_2^{\bullet-}$, and PN simultaneously under controlled conditions. In chapter 2 the design strategies of the platform and its detailed characterization are discussed. This chapter concludes with the first study attempting to establish this platform as a bioanalytical tool using intrinsic reporter molecule uric acid. Chapters 3, 4, and 5 describe reactions of PN with selected substrates to firmly establish the utility of the two-component PN-generating platform as an effective system to explore the chemistry of PN. While chapter 3 focuses on an established reaction between PN and tyrosine, chapters 4 and 5 include substrates of PN previously unexplored. In addition to PN-specific chemistry, chapter 5 also highlights the capacity of the platform to simultaneously probe the chemistry of NO and $O_2^{\bullet-}$.

1.4 References

1. Ignarro, L.J.; Buga, G.M.; Wood, K.S.; Byrns, R.E.; Chaudhuri, G., *Proc. Natl. Acad. Sci. U.S.A.* **1987**, *84*, 9265-9269.
2. Radomski, M.W.; Palmer, R.M.; Moncada, S., *Proc. Natl. Acad. Sci. U.S.A.* **1990**, *87*, 5193-5197.
3. Hill, B.G.; Dranka, B.P.; Bailey, S.M.; Lancaster, J.R.; Darley-Usmar, V.M., *J. Biol. Chem*. **2010**, *285*, 19699-19704.
4. Vincent, S.R, Prog. Neurobiol., **2010**, *90*, 264-255.
5. Thomas, D.D; Ridnour, L.A.; Isenberg, J.S.; Flores-Santana, W.; Switzer, C.H.; Donzelli, S.; Hussain, P.; Vecoli, C.; Paolocci, N.; Colton, C.A.; Harris, C.C; Roberts, D.D; Wink, D.A., *Free Radic. Biol. Med*., **2008**, *45*, 18-31.
6. Pacher, P., Beckman, J. S., and Liaudet, L. (2007) *Physiol. Rev.* **87**, 315-424
7. Beckman, J.S.; Koppenol, W.H., *Am. J. Physiol,*, **1996**, *271*, C1424-C1437.
8. Szabó, C.; Ischiropoulos, H.; Radi, R., *Nat. Rev. Drug. Discov.*, **2007**, 6, 662-680.
9. Koppenol, W.H., Moreno, J.J., Pryor, W.A., Ischiropoulos, H., and Beckman, J.S., *Chem. Res. Toxicol.*, **1992**, *5*, 834-842.
10. Förestermann, U.; Sessa, W.C., *Eur. Heart J.*, **2012**, *33*, 829-837.
11. Nathan, C.; Xie, Q.-w., *Cell*, **1994**, *23*, 915-918.
12. Carnicer, R.; Crabtree, M.J.; Sivakumaran, V.; Casadei, B.; Kass, D.A., *Antioxid. Redox Signal.,* **2013**, *18*, 1078-1099
13. Toledo, J.C.; Augusto, O., *Chem. Res. Toxicol*., **2012**, *25*, 975-989.

14. Arnold, W.P.; Mittal, C.K.; Katsuki, S.; Murad, F,. *Proc. Natl. Acad. Sci. U.S.A.*, **1977**, *74*, 3203-3207.

15. Wolin, M.S.; Wood, K.S.; Ignarro, L.J., *J. Biol. Chem*., **1982**, *257*, 3312-3320.

16. Nathan, C., *J. Clin Invest.*, **1997**, *100*, 2417-2423.

17. Stasch, J.-P.; Becker, E.M.; Alonso-Alija, C.; Apeler, H.; Dembowsky, K.; Feurer, A.; Gerzer, R.; Minuth, T.; Perzborn, E., Ple, U.; Schröder, H.; Schroeder, W.; Stahl, E.; Steinke, W.; Straub, A.; Schramm, M., *Nature*, **2001**, *410*, 212-215.

18. Lancaster, J.R., *Nitric Oxide*, **1997**, *1*, 18-30.

19. Beckman, J.S., *Chem. Res. Toxicol.,* **1996**, *9*, 836-844.

20. Stamler, J.S.; Singel, D.J.; Loscalzo, J., *Science*, **1992**, *258*, 1898-1902.

21. (a) Mannick, J.B.; Schonhoff, C.M., *Arch. Biochem. Biophys.*, **2002**, *408*, 1-6. (b) Monteiro, H.P., *Free Radic. Biol. Med*., **2002**, *33*, 765-773. (c) Monteiro, H.P.; Arai, R.J.; Travassos, L.R., *Antiox. Redox Sign.*, **2008**, *10*, 844-879.

22. Stamler, J.S., *Cell*, **1994**, *78*, 931-936.

23. Stamler, J.S.; Lamas, S.; Fang, F., *Cell*, **2001**, *106*, 675-683.

24. (a) Salvemini, D.; Doyle, T.M.; Cuzzocrea, S., Biochem. Soc. T., 2006, 34, 965-970. (b) Murphy, K.; Travers, P.; Walport, M. *Immunology,* 7th ed., New York and London, Garland Science Taylor & Francis Group.

25. Babior, B.M., *Blood*, **1999**, *35*, 1464-1476.

26. Ischiropoulos, H.; Zhu, L.; Beckman, J.S., *Arch. Biochem. Biophys.,* **1992**, *298*, 446-451.

27. Tsai, J.-H. M.; Harrison, J.G.; Martin, J.C.; Hamilton, T.P.; de Woerd, M.; Jablonsky, M.J.; Beckman, J.S., *J. Am. Chem. Soc.,* **1994**, *116*, 4115-4116.

28. Koppenol, W.H.; Klasinc, L., *Int. J. Quant. Chem.*, **1993**, *20*, 1-6.

29. Alverez, B.; Radi, R., *Amino Acids*, **2003**, *25*, 295-311.

30. Pryor, W.A.; Jin, X.; Squadrito, G.L., *Proc. Natl. Acad. Sci. USA*, **1994**, *91*, 11173-111177.

31. Schöneich, C., *BBA Proteins Proteome*, **2005**, *1703*, 111-119.

22. Quijano, C.; Alvarez, B.; Gatti, R.M.; Agusto, A.; Radi, R., *Biochem. J.*, **1997**, *332*, 167-173.

33. Radi, R.; Beckman, J.S.; Bush, K.M.; Freeman, B.A., *J. Biol. Chem*., **1991**, *266*, 4244-4250.

34. Quijano, C.; Alvarez, B.; Gatti, R.M.; Agusto, A.; Radi, R., *Biochem. J.*, **1997**, *332*, 167-173.

35. Beckman, J.S.; Beckman, T.W.; Chen, J.; Mashall, P.A.; Freeman, B.A., *Proc. Natl. Acad. Sci. USA*, **1994**, *87*, 1620-1624.

36. Crow, J.P.; Spruell, C.; Chen, J.; Gunn, C.; Ischiropoulos, H.; Smith, C.D.; Radi, R.; Koppenol. W.H.; Beckman, J.S., *Free Radic. Biol. Med*., **1994**, *16*, 331-338.

37. Kalyanaraman, H.; Karoui, H.; Singh, R.J.; Felix, C.C, *Anal. Biochem.*, **1996**, *241*, 75-81.

38. Oteiza, P.I., *Free Radic. Biol. Med.*, **2012**, *53*, 1748-1759.

39. Py, B.; Barras, F., *Nat. Rev. Microbiology*, 2010, 8, 436-446.

40. Radi R., *Proc. Nat. Acad. Sci.*, **2004**, *101*, 4003-4008.

41. Bartesaghi, S.; Wenzel, J.; Trujillo, M.; López, M.; Joseph, J.; Kalyanaraman, B.; Radi, R., *Chem. Res. Toxicol*., **2010**, *23*, 821, 835.

42. Ferer-Sueta, G.; Radi, R., *ACS Chem Biol*., **2009**, *4*, 161-177.

43. Goldstein, S.; Merényi, G., *Methods Enzymol.,* **2008**, *436*, 50-57.

44. Gupta, D.; Harish, B.; Kissner, R.; Koppenol, W.H., *Dalton Trans.*, **2009**, 5730-5736.

45. Augusto, O.; Bonni, M.G.; Amanso, A.M.; Linares, E.; Santos, C.C.X., De Menezes, S.L., *Free Radic. Biol. Med.,* **2002**, *32*, 841-859.

46. Trujillo, M.; Naviliat, N.; Alverez, M.N.; Peluffo, G.; Radi, R., *ANALUSIS*, **2000**, *28*, 518-527.

47. Koppenol, W.H., *Free. Radic Biol. Med.,* **1998**, *25*, 385-391.

48. (a) Coddington, J.W.; Hurst, J.K.; Lymar, S.V., *J. Am. Chem. Soc*., **1999**, *121*, 2438-2443. (b) Crow, J.P.; Pruell, C.; Chen, J. Gunn, C.; Ischiropoulos, H.; Tsai, M.; Smith, G.D.; Radi, R.; Koppenol, W.H.; Beckman, J.S., *Free Radic. Biol. Med.*, **1994**, *16*, 331-338.

49. (a) Radi, R. *Accounts Chem. Res.*, **2013**, *46*, 550-559. (b) Schöneich, C., *BBA Proteins Proteome*, **2005**, *1703*, 111-119.

50. Ischiropoulos, H., Arch. Biochem. Biophys., **2009**, *484*, 117-121.

51. McMillan-Crow, L.A.; Crow, J.P.; Thompson, J.A., *Biochemistry-US*, **1998**, *37*, 1613-1622.

52. Warren, J.J.; Winkler, J.R.; Gray, H.B., *FEBS Lett.*, **2012**, *586*, 596-602.

53. Santos, C.X.C.; Bonni, M.G.; Augusto, O., *Arch. Biochem. Biophys.*, **2000**, *377*, 146-152.

54. Pfeiffer, S.; Schmidt, K.; Mayer, B., *J. Biol. Chem.*, **2000**, *275*, 6346-6352.

55. Szabo, C., *Toxicol Lett.,* **2003**, *140-141*, 105-112.

56. Szabo, C., *Shock*, **1996**, *6*, 79-88.

57. Freeman, B.A.; Baker, P.R.S.; Fancisco, S.J.; Woodcock, S.R.; Napolitano, A.; Ischia, M., *J. Biol. Chem.,* **2008**, *283*, 15515-15519.

58. Rubbo, H.; Trostchansky, A.; O'Donnel, V.B., *Archives of Biochem. Biophys.*, **2009**, *484*, 167-172.

59. Rubbo, H.; Radi, R., *BBA-Gen. Subjects*, **2008**, *1780*, 1318-1324.

60. Villacorta, L.; Zhang, J.; Garcia-Barrio, M.T.; Chen, X.-L.; Freeman, B.A.; Chen, Y. E.; Cui, T., *Am. J. Physiol. Heart and Circulatory Physiol*., **2007**, *293*, H770-H776.

61. Ischiropoulos, H.; Beckman, J.S*., J. Clin. Invest.*, **2003**, *111*, 163–169.

62. Baker, P.R.; Lin, Y.; Schopfer, F.J.; Woodcock, S.R.; Groeger, A.L.; Batthyany, C.; Sweeney, S.; Long, M.H.; Iles, K.E.; Baker, L.M.; Branchaud, B.P.; Chen, Y.E.; Freeman, B.A., *J. Biol. Chem.*, **2005**, *280*, 42464–42475.

63. Balazy, M.; Lesaki, T.; Park, J.L.; Jiang, H.; Kaminski, P.M.; Wolin, M.S., J. *Pharmacol. Exp. Ther.*, **2001**, *299*, 611–619.

64. Kang, K.W.; Choi, S.H.; Kim, S.G., *Nitric Oxide*, **2002**, *7*, 244-253.

65. Koeck, T.; Fu, X.; Hazen,, J.W.; Crabb, J.W.; Stuehr, D.J.; Aulak, K.S., J. Biol. Chem., **2004**, *279*, 27257-27262

Chapter 2. Construction of a Two-Component System that is Capable of Generating the Reactive Nitrogen Species Peroxynitrite *In Situ*

2.1 Background

The synthetic history of peroxynitrite (PN) is rich and dates back as early as the late 1920's when it was observed that passing ozone through an azide solution yielded a yellow solution of oxoperoxonitrate (-1).[1] Over the course of the past 40 years numerous synthetic chemical approaches and systems have been reported in the literature in attempts to generate pure and abundant amounts of PN, a few of which will be highlighted bellow.[2,3] However in all attempts, regardless of the reactants chosen or synthetic apparatus employed, the resultant product solution required rapid basification to stabilize and extend the lifetime of the PN.[4] Under alkaline conditions, the conjugate base ($ONOO^-$) of peroxynitrous acid (ONOOH) predominates. This anion, present in its stabilized *cis* conformation, resists pathways of interconversion to the *trans* conformer (due to a significant energy barrier of 30kcal/mol) that more easily isomerizes to less reactive nitrate.[5] For this reason all synthetic methods suffer from the same inherent pitfall, they all afford an alkaline stock solutions of PN.

While classic synthetic methods were designed to produce bulk amounts of PN that could be used to rapidly nitrate tyrosine residues within proteins and enzymes as positive standards in studies requiring the use of 3-nitrotyrosine antibodies, some argued that the physiological existence of this reactive species in the body was questionable at best. In the mid to late 1990's, a succession of reports were published in the *Journal of Biological Chemistry* disputing the physiological relevance peroxynitrite in the body on the basis of conflicting results that confirmed and repudiated the proposed footprint of the reactive species *in vivo*, namely PN-mediated

nitration of tyrosine. [6-8] Significance of these works run deeper than the obvious claim or challenge of a seemingly simple chemical process, but will not be discussed here. However, an objective observation that was made clear through these studies was that the *not all source of peroxynitrite are created equal.*

2.1.1 Synthesis of Peroxynitrite: Modified Quenched-Flow System

Since its first report in 1974, the quench-flow reactor apparatus method has been one of the most commonly utilized procedures for large-scale production of PN.[4] This process requires the rapid mixing of an acidified solution of hydrogen peroxide and sodium nitrite, followed by rapid quenching and basification. The resulting solution must then be purified to remove excess H_2O_2 by passing the solution through a MnO_2 column and can then be stored at -20° C until use. While the first report of this synthesis by Jolly and coworkers employed a pressurized quenched flow reactor, a modified system proposed by Beckman and coworkers quickly became the standard for generating "authentic" PN because it requires only Erlenmeyer flasks and a house vacuum line.[2] A description of this apparatus is shown in Figure 2.1. In the first Erlenmeyer flask hydrochloric acid and H_2O_2 are held and rapidly mixed with sodium nitrite at *Junction 1*. The reaction proceeds until the solution reaches *Junction 2* where it is then quenched and basified prior to collection. The authors note that in the first minutes of the reaction the resultant solution is wasted until the solution is visibly pale yellow, indicating PN formation. At the onset of a color change the reaction mixture is finally collected in the collection flask.

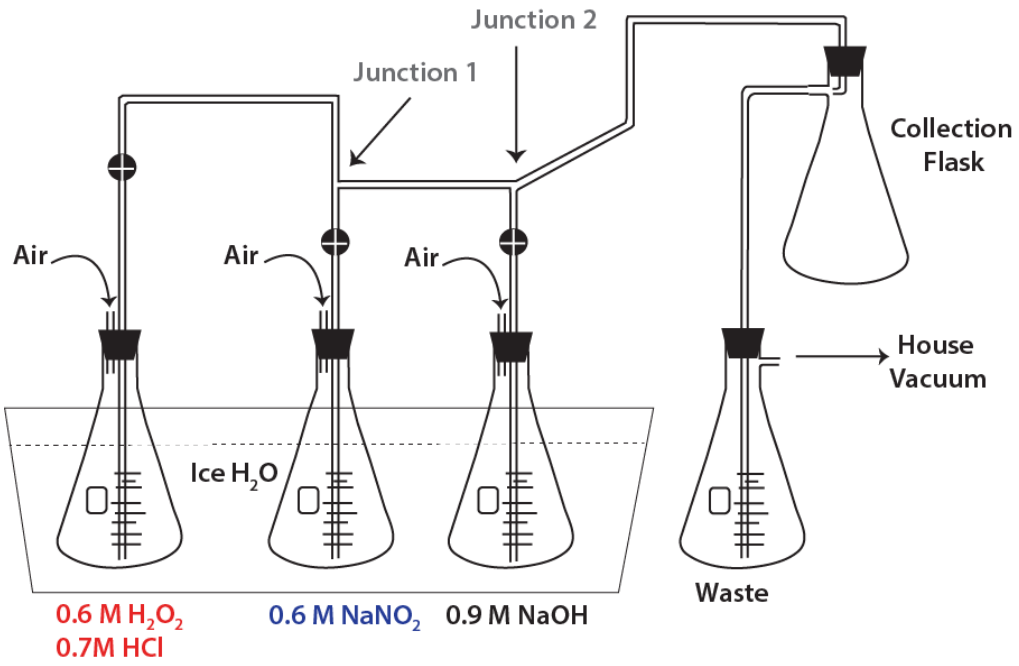

Figure 2.1. Illustration depicting the modified quenched-flow system most commonly used to synthesize PN in bulk.

The synthesis of PN through the reaction of nitrite (NO_2^-) with H_2O_2 was realized after it was observed that a mixture of acidified H_2O_2 and nitrous acid nitrated aromatic compounds. Under acidic conditions nitrite (pK_a= 4.3) is protonated to form nitrous acid, and this molecule lies in an equilibrium state between its acid form and a species more closely representative of a nitrosyl cation (Figure 2.2). The nitrosyl is a potent nitrosating agent that rapidly reacts with H_2O_2 to produce PN.

$$NO_2^- + H^+ \longrightarrow \underset{\text{Nitrosyl cation-}\textit{like}\text{ species}}{[HO\text{-------}NO]} + H_2O_2 \longrightarrow \underset{\text{Peroxynitrite Anion}}{ONOO^-}$$

Figure 2.2. Chemical description of the reaction between nitrous acid and hydrogen peroxide to form PN

Optimization of quenched flow systems have largely contributed to significant enhancements in the yield of this reaction. Unfortunately increased concentrations of PN can actually increase its rate of decomposition in stock solutions. While nitrate has most commonly been highlighted as a significant decomposition product of PN, the reactive species largely decomposes to nitrite under alkaline conditions. Formation of nitrite in stock solutions of PN is proposed to form through a succession of reactions initiated by the oxidation of peroxynitrite anion ($ONOO^-$) by peroxynitrous acid (ONOOH, Reaction 1, Figure 2.3). The result of this disumation reaction is the formation of nitrogen dioxide ($^{\bullet}NO_2$) and nitrosyldioxyl radical ($ONOO^{\bullet}$) that ultimately produce dinitrogen trioxide (N_2O_3). Under the alkaline milieu of the authentic PN solution N_2O_3 will finally decompose to yield two equivalents of nitrite (NO_2^-). In fact, it has been reported that authentic PN solutions stored in at -20° C slowly concentrate over time, yielding significant concentrations of PN and even higher concentrations of NO_2^- contaminant. For this reason authentic PN solutions are typically prepared at lower concentrations.

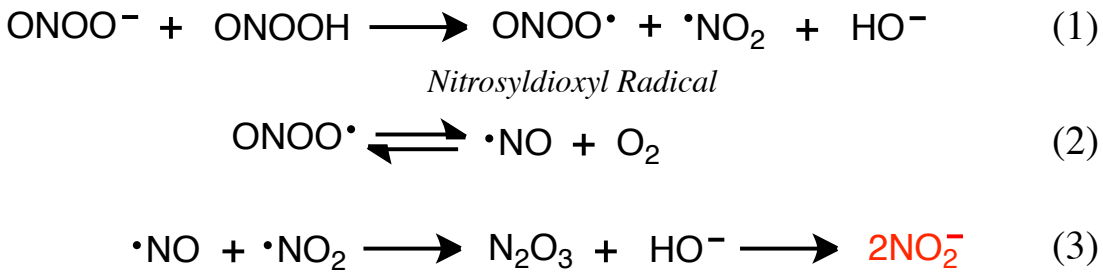

Figure 2.3. Proposed reaction pathway of authentic PN decomposition to NO_2^-

2.1.2 Synthesis of Peroxynitrite: Potassium Superoxide and Nitric Oxide Gas

An obvious option for synthesizing PN is through combination of its fundamental components superoxide ($O_2^{\bullet-}$) and nitric oxide (NO). Beckman and coworkers exploited this possibility by synthesizing the potassium salt of PN through the reaction of potassium superoxide (KO_2) with gaseous NO.[2] The synthesis procedure first calls for the preparation of a KO_2 solution, prepared by adding a degassed pH 12 potassium sodium hydroxide solution to solid KO_2 under inert conditions. NO is then bubbled through the solution until it appears light yellow in hue. Air-free conditions are required for the successful synthesis of PN by this method because O_2 can react with NO to produce unwanted byproducts that not only inhibit PN formation but also yield secondary products that are capable of actively decomposing PN as it forms. For the latter reason, a modified version of this procedure has been proposed, where an alkaline NO saturated solution (~1.7 mM) replaced NO bubbling into the KO_2 solution. However, when the efficiency and reproducibility of PN formation of this method are compared to the modified quenched flow system a large disparity is realized. This inadequacy arises from a significant lack of quantitation of both the $O_2^{\bullet-}$ and NO sources given their inherent instability. The former creates much more variability than the latter. KO_2 rapidly reacts with H_2O to yield O_2 and KOH, resulting in uncertainty in the starting quantities of $O_2^{\bullet-}$ and introducing O_2 into the system that can react with NO and inhibit PN formation.

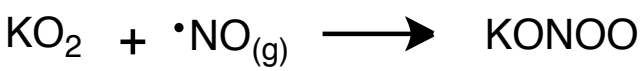

Figure. 2.4. Potassium peroxynitrite synthesis reaction

2.1.3 Synthesis of Pure Tetraethylammonium Peroxynitrite

In attempts to provide a source of PN for quantitative measurements Hansert and coworkers reported the synthesis of a "pure" PN source, namely tetramethyl-ammonium peroxynitrite ($[(CH_3)_4N][ONOO]$).[9] The tetramethylammonium salt was described as a pure, stable, bright yellow solid that could be stored in its solid form for upwards of a month at -20° C under inert conditions (N_2 atmosphere). However, immediate decomposition is noted when the solid was added to most solvents, emphasizing the advantage of this PN salt source to be in minimization of contaminants for biochemical experiments. This advantage is not to be undermined, given the strong reactivity of some contaminants in PN sources such as ozone and hydrogen peroxide (H_2O_2).

The reaction is completed under inert atmosphere and requires the use of air-free glassware. All solutions were first flushed with N_2 for at least 30 min to drive out O_2 that could react with both superoxide and nitric oxide and diminish the yield of $[(CH_3)_4N][ONOO]$. The synthetic process begins with the metathesis reaction to prepare the $O_2^{\bullet-}$ starting salt $[(CH_3)_4N][O_2]$ from tetramethylammoium hydroxide pentahydrate ($[(CH_3)_4N][OH]\bullet 5H_2O$) and potassium superoxide (KO_2) that is carried out in the solid-phase under vacuum (Figure 2.1). The finely ground salts required extensive mixing for upwards of 3 days to form $[(CH_3)_4N][O_2]$, but upon completion a pale yellow solid was observed and extracted using anhydrous ammonia. The final superoxide salt was purified which was then crystalized from a concentrated ammonia solution. In the final phase of the synthesis, 60 mg of $[(CH_3)_4N][O_2]$ was

added to a Schlenk flask in a dry box. The flask was then removed from dry box and kept under continuous N_2 pressure. Anhydrous ammonia was added (~30mL) to the solid and then dried and purified NO gas was bubbled through the $[(CH_3)_4N][O_2]$ solution to produce $[(CH_3)_4N][ONOO]$.

$$[(CH_3)_4N]\cdot 5H_2O + 11KO_2 \longrightarrow \underset{\text{Superoxide Salt}}{[(CH_3)_4NH_2][O_2]} + 11KOH + 7\frac{1}{2}O_2$$

$$[(CH_3)_4NH_3][O_2] + {}^{\bullet}NO_{(g)} \longrightarrow \underset{\substack{\text{Bright Yellow-Orange}\\ \text{"Pure" Peroxynitrite Salt}}}{[(CH_3)_4NH_3][ONOO]}$$

Figure 2.5. Representative chemical equations describing the synthesis of "pure" tetramethylammonium peroxynitrite.

In general, this synthetic procedure is time-consuming and hazardous. Not every lab is equipped with a solid-state reactor, required for $[(CH_3)_4N][O_2]$ synthesis. The authors therefore suggest alternative options such as a rotovap. Unfortunately, this substitution requires increased mixing time to reach completion, extending the first step of the synthesis from 3 days to ~7 days. Hazards associated with strong oxidant KO_2 and corrosive $[(CH_3)_4N][OH]$ should also be noted. Extreme care must be taken when working with both reagents. It was reported that initial use of anhydrous $[(CH_3)_4N][OH]$ resulted in a "large explosion" during the metathesis reaction that required the use of the pentahydrate form, which can be hydroscopic. Unfortunately, KO_2 reacts vigorously with H_2O. Taken together, it is quite evident that attempts to

synthesis PN by this method would (should) only be suitable for research groups equipped with proper synthetic capabilities.

2.1.4 3-Morpholinosydnonimine (SIN-1)

Sydnonimine 3-morpholinosydnonimine (SIN-1, Lisidomine) was first reported as the active metabolite of vasodilatory drug Molsidomine in the 1980's.[10] Initial insight into the chemical pathway of NO release from SIN-1 was somewhat obscure. It was however established and widely accepted that many sydnonimines promote NO-dependent pathways that ultimately led to vasodilation and inhibit platelet aggregation effects in the body. Later, attempts to uncover the mechanistic chemical pathway of NO release from SIN-1 by Feelisch and coworkers unexpectedly revealed the potential of this pharmaceutical to generate PN.[11,12]

NO release from SIN-1 begins with a base-catalyzed ring-opening step that generates the reactive metabolite SIN-1A (Figure 2.6). SIN-1A is then oxidized to form an unstable hydrazinium radical cation intermediate that rapidly releases NO and a proton (H^+) to yield N-morpholinoacetoaminonitrile (SIN-1C). It is this oxidation process that dictates the capacity of SIN-1 to transform from an NO to a PN donor. When the predominant electron acceptor (oxidant) is oxygen, $O_2^{\bullet-}$ is generated and rapidly reacts with NO to generate PN. Such conditions are relevant in biochemical systems, but become irrelevant in cellular assays where numerous electron acceptors are present.[13] Unfortunately, these descriptions represent extremes of a continuum. For this reason use of SIN-1 as a PN donor could be difficult to control and afford numerous complications.

Similar to the previous sources, SIN-1 requires optimal condition to maximize the formation of PN. For biochemical applications, acidic anaerobic solutions of SIN-1 are prepared to inhibit activation. The acidity of the stock SIN-1 solution and required basicity for the transformation of SIN-1 to active SIN-1A must be carefully accounted for to assure adequate PN formation. In general, ideal conditions for optimal PN formation from SIN-1 must be carefully defined in every experiment to account for the potential non-innocent molecules that could inadvertently act as oxidants that could compete with oxygen. Interestingly, under the most ideal conditions alternative complications must be considered such as anoxia and acidification as a result of rapid reduction of oxygen and production of H^+ in the chemical pathway towards NO release from SIN-1.

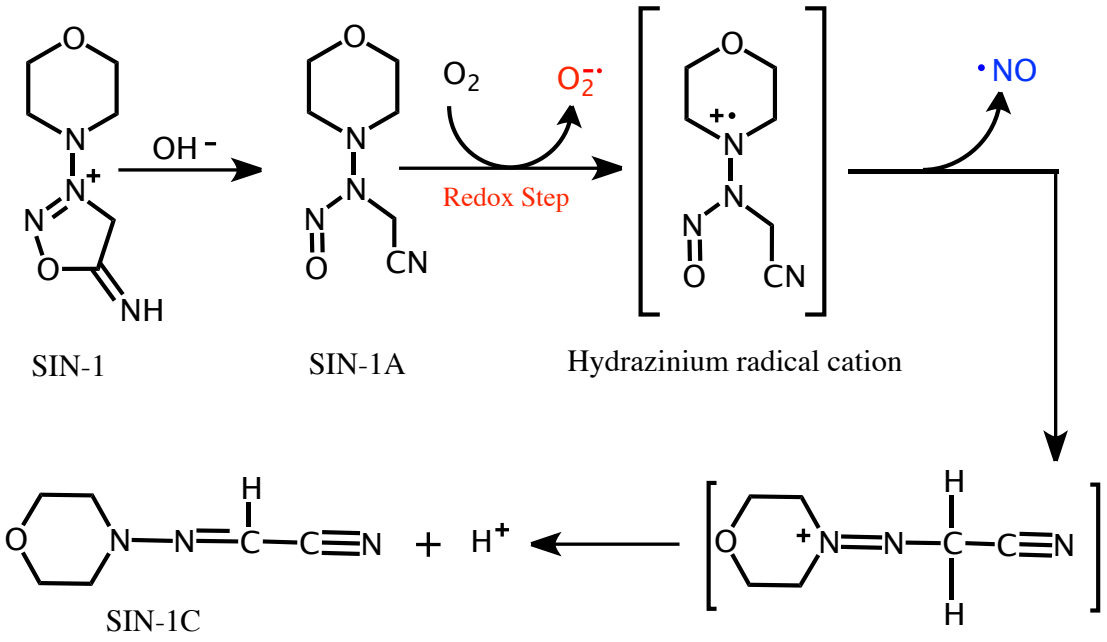

Figure 2.6. Chemical pathway of SIN-1 decomposition to yield NO and $O_2^{\bullet -}$.

2.1.5 Generation of Peroxynitrite *in Situ*

The biomimetic *in situ* co-generation of PN from independent NO and $O_2^{\bullet-}$ sources has been attempted previously. Based on the rate of reaction between NO and $O_2^{\bullet-}$ (1.9×10^{10} M^{-1} s^{-1}) one may presume that formation of PN by this method would not only be ideal but preferred. However, review of the literature reveals a scarcity of studies utilizing *co-generative* sources of PN. This paucity arises from a strong dependence of PN formationon a near unity flux ratio of rates of NO and $O_2^{\bullet-}$ release from their respective sources. Successful generation of PN by this method has been achieved,[14] but lack of standardization deterred its use compared to the alternative quench flow PN systems.

Lack of standardization largely stems from the variability in the release rates of NO as a function of the NO donor chosen. Diazeniumdiolates (NONOate) and S-nitrosothiols are classes of NO donors that have been successfully employed in the *in situ* generation of PN when paired with enzymatic generation of $O_2^{\bullet-}$ (by xanthine oxidase). Selection of an NO donor requires serious scrutiny, because the NO release profile can be greatly dependent upon the milieu of the desired experimental system. For example, the half-lives of spermine-NONOate and DETA-NONOate are 39 min and 20 h, respectively, at pH 7.4 at 37° C. [14]

Because co-generative methods represent the most desirable source of PN, we set out to assemble a two-component PN generating system that could be used as a tool to study the complex chemistry of PN under conditions most closely representative of *in vivo* evolution of PN.[15] Our design strategy included the following three steps: (1)

identify an NO donor that releases NO in a quantitative and controlled fashion over a wide pH range and solvent system, (2) design individualized NO and $O_2^{\bullet-}$ donor systems that affords minimal to no unwanted contaminants into experimental milieu, and (3) create a platform capable of evolving NO, $O_2^{\bullet-}$, and PN side-by-side under controlled conditions.

The photoactive metal nitrosyl $[Mn(PaPy_3)(NO)]ClO_4$ (Mn(NO), where $PaPy_3$= *N,N*-bis-(2-pyridylmethyl)amine-*N*-ethyl-2-pyridine-2-carboxamide, was selected as the NO donor because it releases NO quantitatively under the strict control of light (Figure 2.7). Unlike alternative NO sources where NO release is dependent upon thermal or pH stimuli, the activity of Mn(NO) is independent of the chosen buffer system, eliminating variability in NO release as a function of a desired experimental system. The metal nitrosyl was then incorporated into an inert inorganic silicate frame to prevent release of the metal nitrosyl or its resultant photoproduct. The final product was a hard glass-like xerogel that release only NO.

Selection of a compatible $O_2^{\bullet-}$ source that offered a level of control comparable to the light-activated metal nitrosyl proved to be much more complicated. The xanthine oxidase system was ultimately chosen as the ideal $O_2^{\bullet-}$-generating system. The reactive oxygen species is only released upon addition of a xanthine oxidase substrate, affording a level of control comparable to the light-trigger of Mn(NO).The xanthine oxidase was also encapsulated within a silicate frame.

Xanthine oxidase evolves $O_2^{\bullet-}$ as it turns over its purine substrates hypoxanthine and xanthine and ultimately affords uric acid. Throughout this process a total of 4

electrons are available for the single-electron reduction of oxygen to from $O_2^{\bullet-}$. However, in addition to these single-electron processes, two-electron reduction of oxygen can also occur to generate peroxide anions (O_2^{2-}). For this reason catalase was also incorporated into the $O_2^{\bullet-}$-generating silicate to sequester O_2^{2-}.

The release profile of NO and $O_2^{\bullet-}$ from their respective sources were established and tuned to yield a NO:$O_2^{\bullet-}$ flux ratio near 1. With successful matching of the NO:$O_2^{\bullet-}$ flux ratio the individual silicate systems were then combined. Initial prototypes of the system were assembled in scintillation vials, but it quickly became apparent (based on the design of the individual NO and $O_2^{\bullet-}$ sources) that a multi-well platform could easily be created where adjacent lanes could be dedicated to studying the chemistry of PN and its precursors simultaneously. PN generation within the wells of the platform was established and quantified using PN probe coumarin-7-boronic acid (CBA). Finally, intrinsic probe uric acid confirmed PN formation in the wells and highlighted the ability of the system to tuned to any desired flux ratio. This allows for a more complete study of PN chemistry in a single multi-well plate. The design, construction, and characterization of the PN-generating platform are discussed in detail in the subsequent sections.

2.2. Synthesis and Characterization of the Nitric Oxide-Evolving Unit

General synthesis of the Mn(NO) encapsulated silicate piece (Mn(NO)•SG) requires the incorporation of a desired amount of the metal nitrosyl (the synthesis of which has been reported previously)[16,17] into a homogenized tetramethyl orthosilicate

(TMOS) sol-gel mixture in the dark. After the solid is completely dissolved, an aliquot of the resulting solution is plated into a single well of a multi-well plate. The sol-gel layers are then dried and aged within the wells of the plate at 4° C in the dark. Drying and aging times vary depending upon the dimensionality of the well. Successful synthesis of Mn(NO)•SG affords a sol-gel disc that releases NO only upon illumination. Release of NO from the disc is observable due to the inherent color difference of the metal nitrosyl (green) and its photoproduct (yellow-brown).

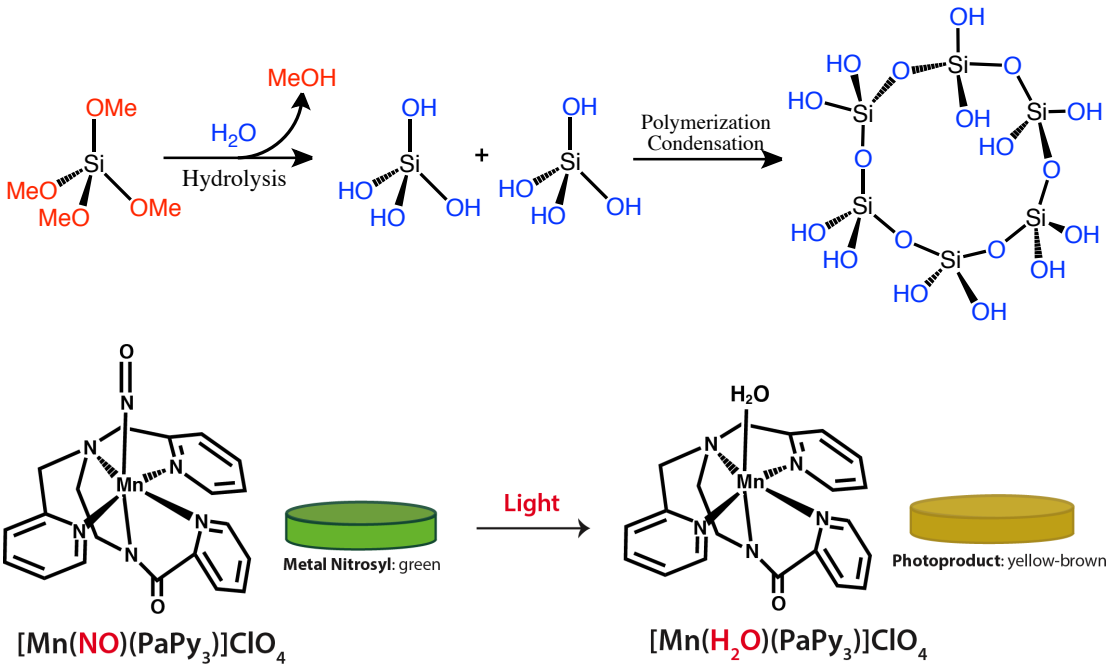

Figure 2.7. Schematic representative of the synthetic process required for the synthesis of Mn(NO)•SG. The chemical synthesis of sol-gel is shown in the top panel and chemical structures of Mn(NO) and the Mn photoproduct in the bottom panel.

The first-generation plates, that will be discussed throughout this chapter, were constructed by dissolving 6 mg of Mn(NO) into 1.1mL of a homogenous sol-gel solution, prepared by mixing 0.400 mL Millipore and 0.700 mL TMOS rapidly for ~1 h, in the dark. Following thorough mixing, 0.075 mL aliquots were poured into the wells of a 96-well plate (well diameter 6.35 mm) and stored at 4°C for 48 h in the dark. The release of NO from the final Mn(NO)•SG pieces were then measured using an inNO electrode. Figure 2.X shows the profile of NO release from the sol-gel discs. A steady increase in the rate of NO release is observed in the first 3 minutes of illumination. The NO release rapidly plateaus at minute three. This steady-state is maintained until 12 min when the flux of NO release begins to decrease (not shown in the NO amperogram in Figure 2.8). Mn(NO)•SG discs were expended at 15 min in these studies.

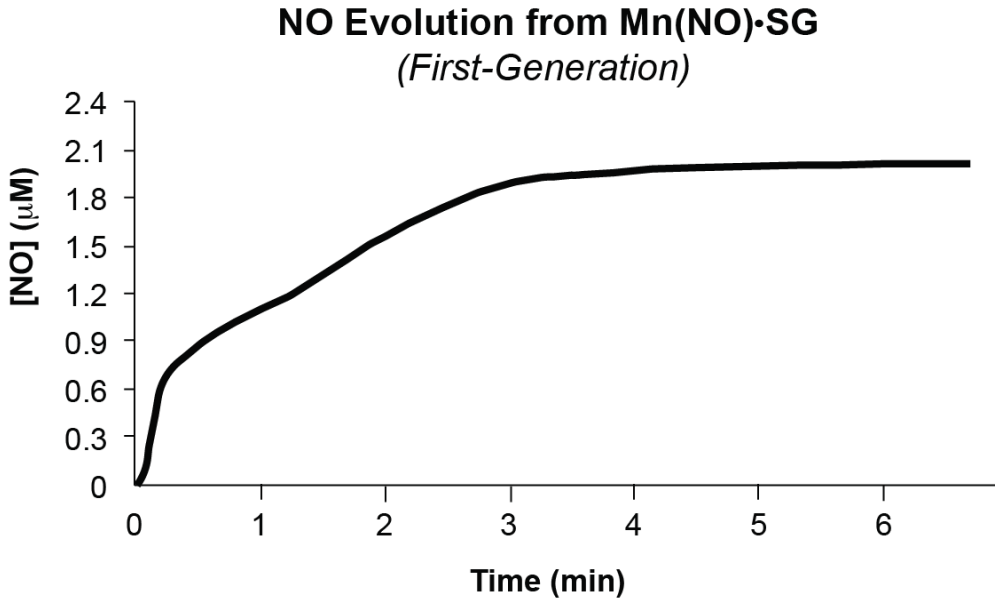

Figure 2.8. Recorded amperogram highlighting the profile of NO release from the first-generation Mn(NO)•SG disc prepared in the wells of a 96-well plate.

The versatility of the Mn(NO)•SG design to afford any desired concentration of NO was established with the synthesis of a second generation sol-gel prepared in a 24-well plate well with a diameter of 15.6 mm (just over 2.5 times the diameter of a single well in a 96-well plate). In short, to a stock solution of hydrolyzed TMOS, a batch of 14 mg of Mn(NO) was added and allowed to stir until the nitrosyl was completely dissolved. A batch of 600 μL of this stock Mn(NO) solution was then added to individual wells and allowed to dry and age for 1 week at 4 °C in the dark. Figure 2.9 shows the profile of NO release from the sol-gel discs, where a steady increase in NO release is observed for the first 5 min of illumination (compared to 3 minutes observed by the first-generation Mn(NO)•SG discs) followed by a steady-state interval from 10 to 20 minutes and a gradual decrease NO flux after 20 minutes.

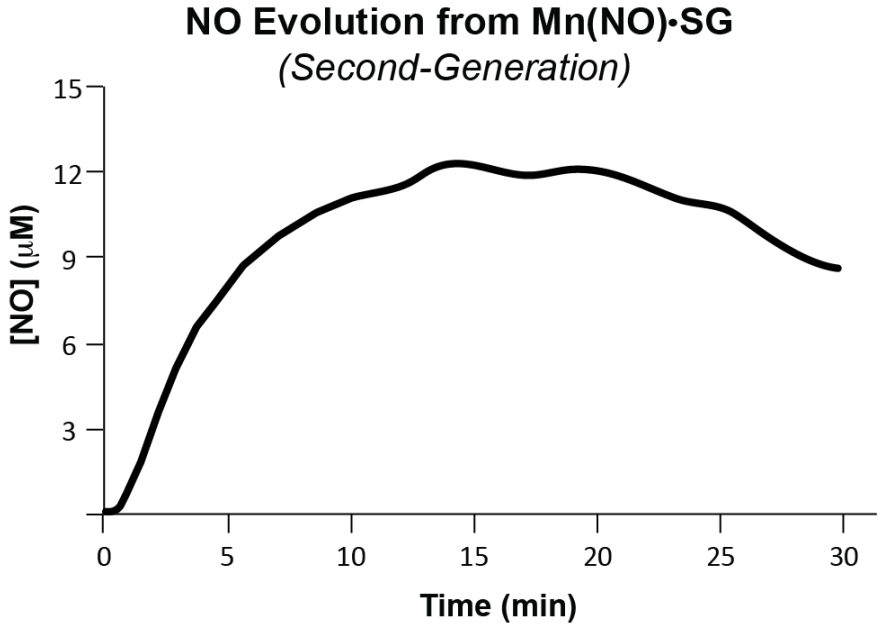

Figure 2.9. Recorded amperogram highlighting the profile of NO release from the first-generation Mn(NO)•SG disc prepared in the wells of a 48-well plate.

2.3 Synthesis of the Superoxide-Evolving Unit

In general, enzyme immobilization became a hot area of research in the early 1990's as the food and pharmaceutical industries realized the potential of exploiting enzymatic transformations as a cost effective substitution to synthetic processes. Through the immobilization of enzymes within material frames, large-scale reactors were designed that harnessed the remarkable efficiency and specificity of enzymes to maximize yields and profits.[18] While there are many methods of enzyme immobilization, an optimal method should be selected based on the activity, dimensions, and isoelectric point of the enzyme.

Our design strategy for the encapsulation of xanthine oxidase and catalase was inspired by techniques reported by Zink and Valentine.[19] Because both xanthine oxidase and catalase are relatively large (both ~270 kDa, xanthine oxidase 7.5 nm diameter) and robust enzymes, an entrapment method employing a silicate frame was selected. The xanthine oxidase and catalase encapsulated sol-gel discs (XO-CAT•SG) are synthesized in two phases. First, a stock solution of TMOS sol-gel is prepared by combing 3.15g of TMOS, 0.676 g MilliQ water and 1 drop of a pH 1.4 hydrochloric acid solution into a scintillation vial. The mixture is then sonicated at 4 °C until the final homogenous sol-gel mixture (TMOS•SG) is obtained. This stock solution can be used immediately or stored at -20 °C for upwards of 2 month. In the second and final stage of XO-CAT•SG synthesis a stock solution of XO and CAT is prepared by dissolving 4 mg of each enzyme gently into 1 mL of pH 7.8 phosphate buffer. The TMOS•SG mixture, XO-CAT stock solution and 3 mL of pH 7.8 phosphate buffer

are placed in an ice bath and allowed to cool for 15 minutes. After this cooling period, a batch of 1.2 mL of phosphate buffer is added to 1 mL of the TMOS•SG mixture. The pH of this solution is adjusted from ~2 to ~5, and the mixture is quickly mixed. To this solution 0.800 mL of the XO-CAT stock solution are added, mixed, and quickly plated into the wells of a multi-well plate. Within seconds of plating, the stock enzyme sol-gel solution gels and becomes a firm layer at the bottom of the respective wells. The sol-gel layers are then dried and aged at 4 °C to assure full immobilization of XO and CAT into the silicate frame (Figure 2.10).

The process of sol-gel synthesis is highly pH-dependent.[20] Acidic conditions catalyze the hydrolysis of TMOS yielding a fluid sol-gel solution that gradually increases in viscosity as the pH is progressively increases. Further, the role of pH plays a significant role in the encapsulation of XO and CAT, because the activity and the structure of an enzyme are largely affected by pH conditions. Excessively acidic

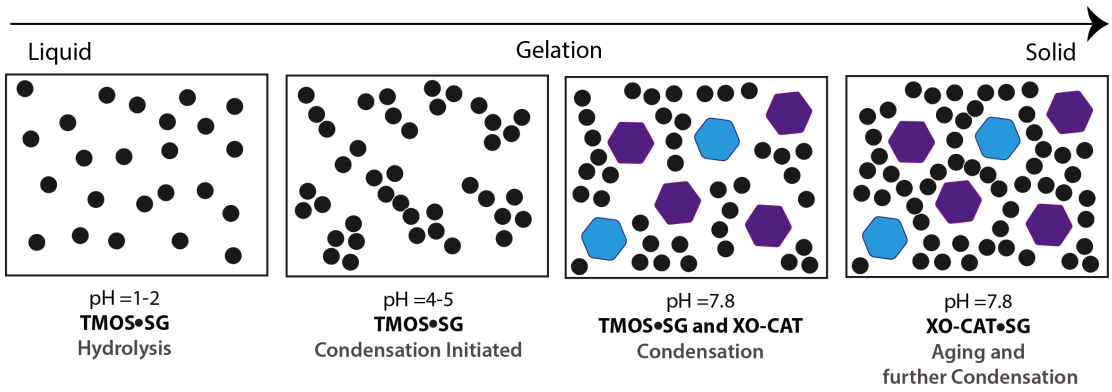

Figure 2.10. Schematic representation of the encapsulation process, where small black spheres represent hydrolyzed silicon species and purple and blue hexagons represent large enzymes xanthine oxidase and catalase.

or alkaline environments can be detrimental to an enzyme and result in its denaturation and subsequent inactivation. However, successful and optimal encapsulation of an enzyme into inorganic or polymers frames can result in increased activity and longevity of an enzyme. This feature was observed in the case of the XO-CAT•SG, where even after long periods of storage the enzyme activity remains intact. Further, a single XO-CAT•SG disc can be used for multiple times before a diminishment in the enzyme activity is observed.

In the present work, two generations of XO-CAT•SG pieces were synthesized and their enzyme activities were measured. In the first case, 0.150 mL aliquots of the enzyme encapsulated sol-gel solution were added to the wells of a 96-well plate and in the second 0.600 mL were added to the wells of a 24-well plate. The activity of encapsulated XO was determined within the wells by incubating the sol-gel pieces with 250 μM HX and monitoring the rate of uric acid formation over 45 min using electronic absorption spectroscopy. 100 μL aliquots were taken from the wells and quantitatively diluted in a cuvette. However, to determine the rate of superoxide release from XO-CAT•SG pieces, standard discs were prepared directly into cuvettes allowing for continuous and real-time monitoring of substrate turnover by electronic absorption spectroscopy because both substrates of XO (hypoxanthine and xanthine) and its product (uric acid) display unique λ_{max} values (250, 230, and 290 nm, respectively, Figure 2.11). The rate of $O_2^{\bullet-}$ generation can be deduced from analyzing and quantifying the rate of uric acid formation. Additional experiments with the $O_2^{\bullet-}$ probe nitroblue tetrazolium (NBT) were performed to corroborate the rate

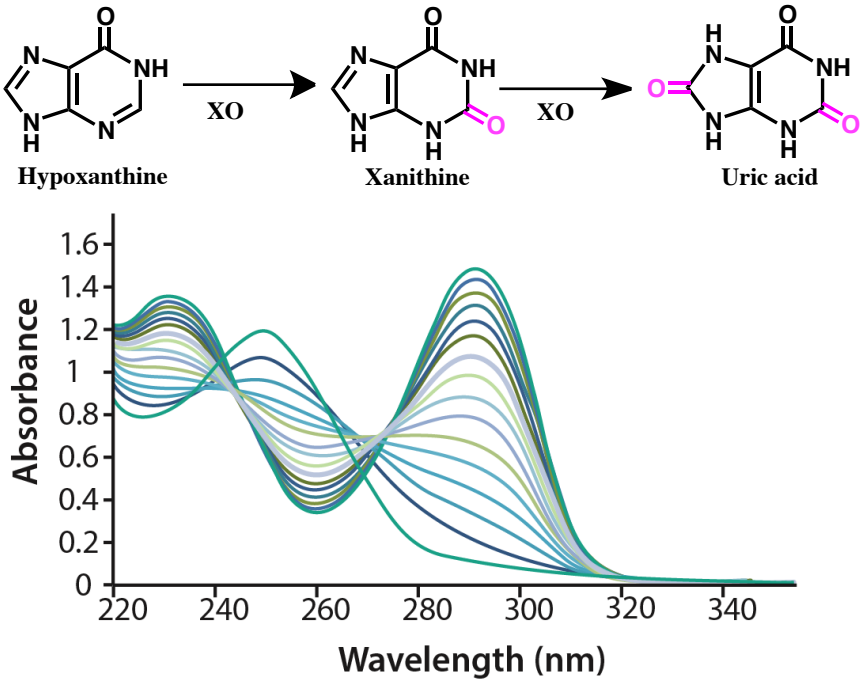

Figure 2.11. The electronic absorption spectrum collected when XO substrate was added to a XO-CAT•SG piece that was prepared in a 3 mL cuvette.

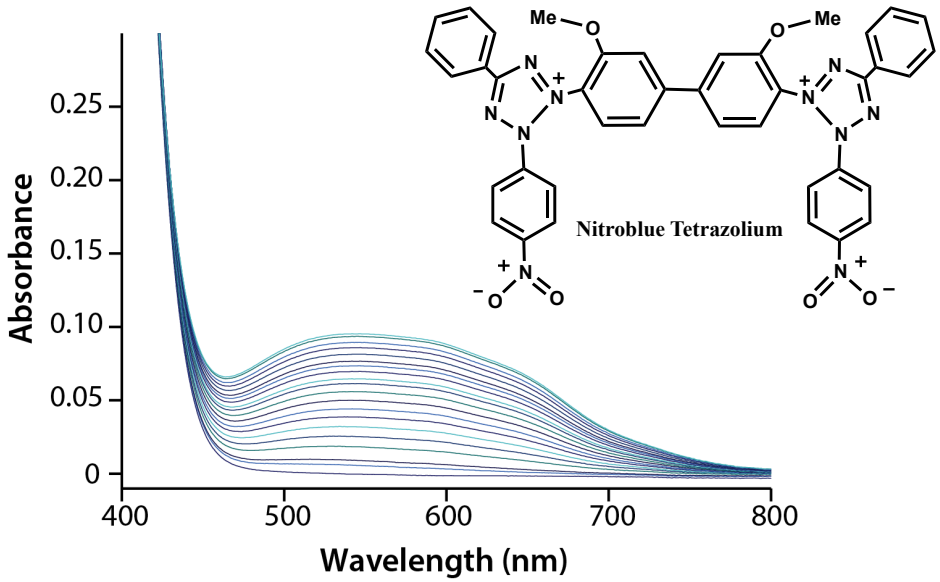

Figure 2.12. The electronic absorption spectrum collected of the same XO-CAT•SG presented in Figure 2.11, with incorporation of NBT to colorimetrically detect $O_2^{\bullet -}$.

of release based on uric acid formation. Detection of $O_2^{\bullet-}$ formation is observable spectrophotometrically with the growth of a peak at 550 nm indicative of $O_2^{\bullet-}$-dependent NBT oxidation. First-generation XO-CAT•SG discs yielded a $O_2^{\bullet-}$ release rates of ~0.6 μM min^{-1}, while with the second-generation discs this rate was increased to ~5 μM min^{-1} (Figure 2.13).

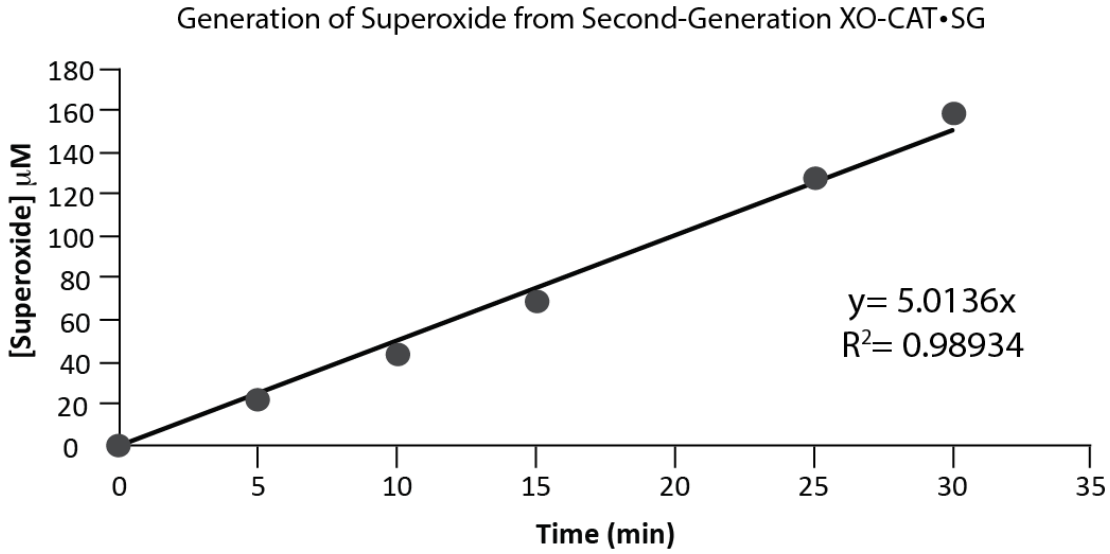

Figure 2.13. Plot illustrating the $O_2^{\bullet-}$ flux profile from XO-CAT•SG discs. Points shown were calculated based on the concentration of uric acid present at the corresponding time point. Aliquots of 100 μL were collected from a well of 24-well plate that contained a single XO-CAT•SG discs and 250 μM solution of hypoxanthine every 5 minutes.

Reproducibility of $O_2^{\bullet-}$ release from the enzyme-loaded sol-gel discs were also established using similar techniques required to standard the flux profile. When three second-generation XO-CAT•SG discs were taken from three different batches and

allowed to evolve $O_2^{\bullet-}$ in the wells of a 24-well plate for 35 minutes a linear trend was observed (Figure 2.14). Aliquots were taken from the three wells over the 35 minute time period at various time points and plotted against the observed concentration of $O_2^{\bullet-}$, results are shown in Figure 2.14.

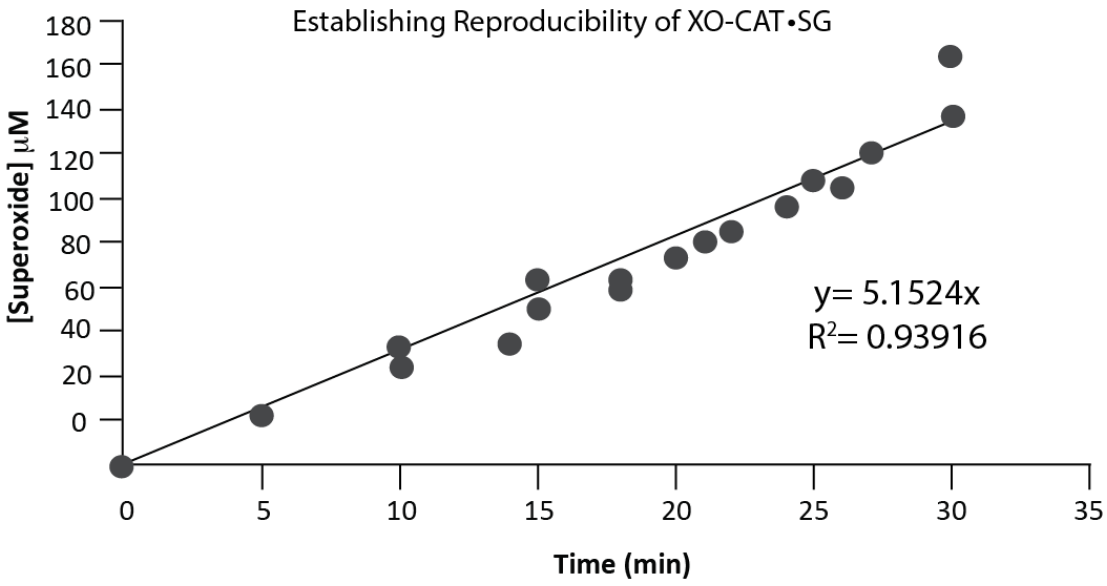

Figure 2.14. Plot of corresponding data points collected from three independent wells that contain a single XO-CAT•SG discs and 250 μM solution of hypoxanthine. Each point represents a single aliquot taken at a given time from one of the three wells.

2.4. Determination of NO and $O_2^{\bullet-}$ Flux Ratios

It should be noted that although the flux profiles of NO and $O_2^{\bullet-}$ vary, the relative concentrations of both species are within the same order of magnitude throughout the desired experimental window. For example, the NO flux profile from the second-generation Mn(NO)•SG discs displays sharp release rate immediately following exposure to light. The concentration in the well (within a 24-well plate) is brought

rapidly to ~ 12 μM NO and maintained at this concentration for ~15 min (in the absence of $O_2^{\bullet-}$). In comparison the XO-CAT•SG sol-gel pieces generates ~5 μM min^{-1} in a linear fashion immediately following addition of hypoxanthine to the well (24-well plate). However, the independent chemistry of NO and $O_2^{\bullet-}$ affords important insight into the possibility that the designed sol-gel sources could effectively afford PN.

In he case of the light-triggered release of NO from the encapsulated metal nitrosyl a rapid burst of NO was observed in the amperogram as shown in Figure 2.9, and the concentration of NO was sustained in the absence of $O_2^{\bullet-}$ and alternative NO sinks such as a metal or thiol. Maintaining a slight increased flux of $O_2^{\bullet-}$ relative to NO is required for generating high levels of PN over the defined time interval of the system. While excess NO in the wells could equate to secondary side reactions, increased levels of $O_2^{\bullet-}$ rapidly disproportionates to form hydrogen peroxide (H_2O_2). H_2O_2 can then be scavenged by CAT and turned over to molecular oxygen, essentially inhibiting any potential chemistry of $O_2^{\bullet-}$. In general, the disproportionation reaction of $O_2^{\bullet-}$ is the most prevalent pathway of this reactive oxygen species in the absence of NO. Numerous control studies that will be discussed in the following chapters strongly support the absence of any chemistry mediated by $O_2^{\bullet-}$, suggesting that this radical species is minimally reactive.

The balance among NO, $O_2^{\bullet-}$, and H_2O_2 was confirmed through the use of PN probe coumarin-7-boronic acid (CBA).[21] In these studies, individual Mn(NO)•SG and XO-CAT•SG pieces were allowed to evolve NO and $O_2^{\bullet-}$, as discussed above, in the

presence of the PN scavenger. Minimal to no turn-on in fluorescence was observed that would be indicative of PN formation. In comparison a turn-on in fluorescence was observed when Mn(NO)•SG and XO-CAT•SG pieces were incorporated together within a single well, evolving NO and $O_2^{\bullet-}$ simultaneously.

Control studies were also performed where a XO-CAT•SG disc was prepared without the addition of CAT and this resulted in a mild turn on fluorescence. This result was expected because CBA also react with H_2O_2. However the presence of CAT into the $O_2^{\bullet-}$-generating sol-gel disk significantly eliminated this interaction. Given this control, it is now confirmed that the fluorescence observed in the wells where both NO and $O_2^{\bullet-}$ are generated from their corresponding sol-gel pieces arises from the reaction of PN with CBA.

2.5 Platform Construction

A quick recap of the work shows that two of the three original aims defined in the early stages of the system development were met through the design and synthesis of the Mn(NO)•SG and XO-CAT•SG discs. To address the final aim: *assemble a platform capable of offering evolving of NO, $O_2^{\bullet-}$, and PN side-by-side* we chose to incorporate Mn(NO)•SG and XO-CAT•SG into multi-well plates.

Although in the above sections the synthesis and characterization of Mn(NO)•SG and XO-CAT•SG discs were described where first-generation pieces were prepared in the wells of 96-well plates and second-generation pieces were prepared in the wells of 24-well plates, but these sol-gel pieces could be prepared in any dimension well within a multi-well plate. Given the dynamic chemistry of PN and its precursors, we

chose to build the final PN-generating system within the wells of a multi-well plate. The high-throughput nature of multi-well plates presented as an ideal platform to construct the desired PN-generating system because numerous experimental conditions can be studied at a single time.

Because the sol-gel discs are prefabricated they can be incorporated into a multi-well plate to afford side-by-side lanes of wells that contain one or both varieties of sol-gel discs. A final platform construct is shown in Figure 2.15, where two potential combinations of plate design are highlighted. First, the lanes of truncated multi-well prototype are designated in various colors to represents those wells designed to afford NO (green), PN (blue), or $O_2^{\bullet -}$ (light brown) depicting the capacity of the platform to

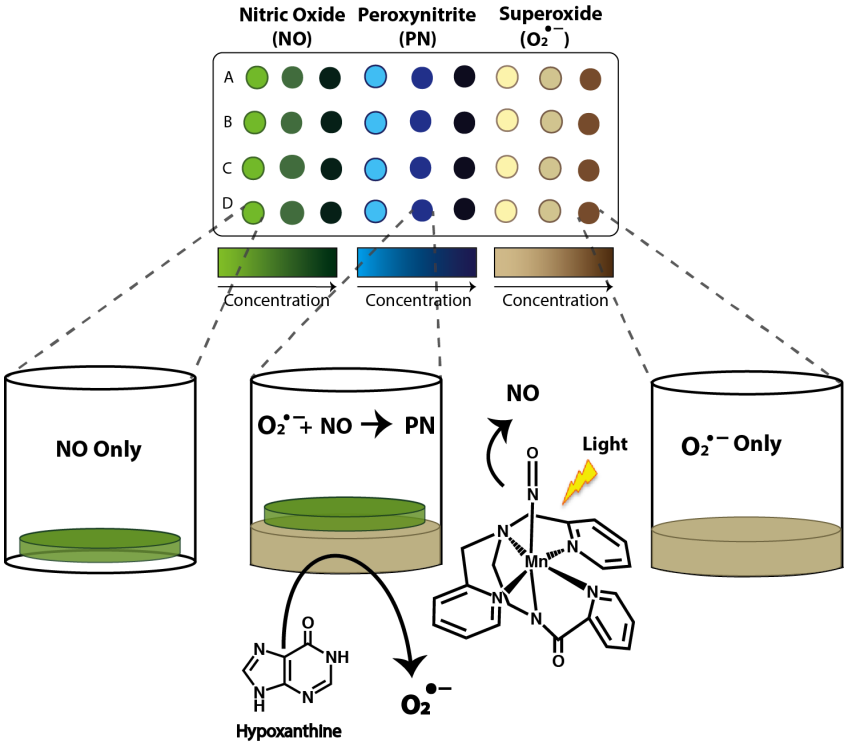

Figure 2.15. Prototype of the PN-generating platform constructed within the wells of a multi-well platform.

study the chemistry of all three reactive species simultaneously. Second, color gradients representative of relative changes in concentration of any one species allows one to explore variations in an observed chemistry based on concentration.

While these two features are highlighted in the prototype schematic they represent only two of the numerous experimental conditions that can be manipulated in the multi-well platform to study a vast spectrum of NO, $O_2^{\bullet -}$, and PN chemistry. For example, the well content can be modulated to explore CO_2-dependence, effects of pH, and roles of antioxidants on a particular PN-mediated reaction. The combinations of conditions within a multi-well PN-generating platform are seemingly endless, and introduce a level of quantitation and control not offered previously with earlier PN sources.

2.6 Establishing and Quantifying the Release of Peroxynitrite

To quantify the concentration of PN with respect to time in the PN-generating wells, coumarin-7-boronic acid (CBA) was employed.[21] Unlike alternative dye systems that react with secondary products of PN, CBA is directly oxidized by PN to from the fluorescent product 7-hydroxycoumarin. The quantification was performed in a single first-generation plate (96-well plate) where PN was generated side-by-side in five wells. In these wells containing 250 mM HX and 25 mM CBA, PN was allowed to evolve for defined time intervals (6, 5, 4, 3, and 2 min), at which point the contents of the well were removed and analyzed by fluorescence spectroscopy (Figure 2.16). The fluorescence data revealed that PN evolved in these wells at the rate of ~150 nM min^{-1}. This rate is physiologically significant because comparable

steady-state concentrations of PN are generated under pro-inflammatory conditions within the body.[3,22] However, when comparable studies were performed using the second-generation platform (24-well plate) a rate ~4 μM min^{-1} was achieved, mimetic of inflammatory conditions.

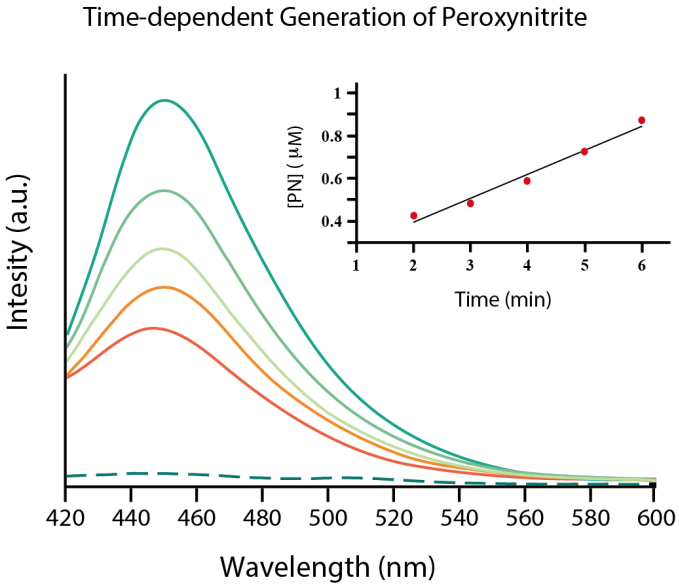

Figure 2.16. Fluorescence spectrum of the PN-mediated oxidation of non-fluorscent boronic acid derivative CBA to its oxidized fluorescent 7-hydroxycoumarin product.

From this point forward when reference is made to the first-generation PN platform, it is comprised of a prefabricated XO-CAT•SG disc layered at the bottom of a well in a 96-well plate with a prefabricated Mn(NO)•SG placed on the top of this $O_2^{\bullet-}$-generating unit. A second-generation PN platform will refer to the same construct but within a the wells of a 24-well plate. In both systems, the addition of

hypoxanthine and exposure to light initiates the release of NO, $O_2^{\bullet-}$, and PN. Table 2.1 displays the parameters of each platform.

Table 2.1. Parameters of the designed PN-generating platforms.

System	Platform	PN Flux	Time of PN Evolution
First-generation	96-well	150 nM min^{-1}	15 minutes
Second-generation	24-well	4 μM min^{-1}	30 minutes

2.7 Probing the Bioanalytical Utility of the Platform

The formation of PN in the wells was further evaluated using the intrinsic reporter molecule uric acid, an oxidation product formed by the $O_2^{\bullet-}$-generating XO system. This purine derivative is a known antioxidant that reacts with NO, $O_2^{\bullet-}$, and PN to afford characteristic products 6-aminouracil, allantoin, and triuret, respectively, that can be easily distinguished by mass spectrometry. Using these unique products we confirmed the flux ratio of NO to $O_2^{\bullet-}$ ($NO:O_2^{\bullet-}$) and demonstrated the effective tuning capacity of this relative flux ratio. When standard first-generation PN-generating wells, PN was allowed to evolve under standard 1:1 $NO:O_2^{\bullet-}$ flux conditions and aliquots of the well contents were collected at 6 min and analyzed by mass spectrometry. PN formation was confirmed by the presence of triuret at 147 m/z (Figure 2.16).[23] Furthermore, the absence of 6-aminouracil and allantoin indicated that PN is the predominant reactive species within the well. When flux ratios of $NO:O_2^{\bullet-}$ was modulated from 1:1 to 2:1 a peak corresponding to 6-aminouracil formation (NO-specific oxidation product of uric acid) was observed at 127 m/z. Modulation of flux ratio to 1:2 yielded a strong peak corresponding to allantoin

formation ($O_2^{\bullet-}$ specific oxidation product of uric acid) at 159 m/z (Figure 2.16). These results establish the tunable control of NO:$O_2^{\bullet-}$ flux ratios of the PN-generating platform to study the dynamic chemistry of PN and its precursors, unachievable through the use of authentic PN solutions or SIN-1.

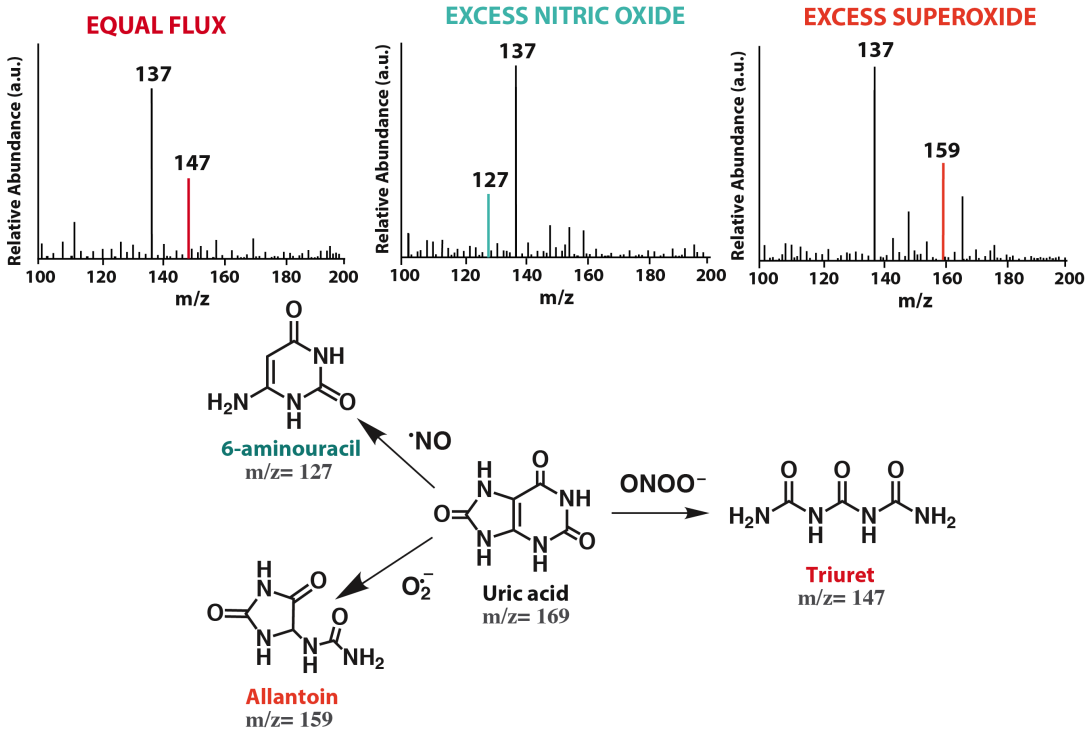

Figure 2.16. Mass spectra of collected samples where the NO:$O_2^{\bullet-}$ flux ratio in three adjacent wells within a first-generation PN-generating platform were modulated from 1:1 (top left), 2:1 (middle) and 1:2 (top right) and the corresponding chemical structures are highlighted in the bottom panel.

2.8 Conclusion

In conclusion, two varieties of PN-generating platforms were successfully designed and constructed that are capable of evolving NO, $O_2^{\bullet-}$, and PN *in situ* under very controlled conditions. The first-generation platform was established to release sub-

μM concentrations of PN representative of pro-inflammatory or physiological concentrations, while the second-generation displayed conditions representative of inflammatory responses (5 μM min^{-1}). The design of individual NO- and $O_2^{\bullet-}$-generating sources, namely Mn(NO)•SG and XO-CAT•SG, introduces a level of versatility that can be harnessed to create a diverse array of conditions to study the dynamic and vast chemistry of PN in a quantitative and controlled fashion.

2.9 Methods

Preparation of First-Generation Mn(NO)•SG Discs. The NO releasing sol-gel was prepared by adding 6 mg of Mn(NO) to 1.10 mL of a homogenized sol-gel mixture (0.400 mL Millipore and 0.700 mL TMOS) in the dark. This stock solution was then thoroughly mixed and added as 75 μL portions to a 96-well plate and stored at 4°C for 48 h in the dark. The release of NO from the Mn(NO) sol-gel pieces were tested within the wells of the plate with an iNO NO monitoring system (Innovative Instruments) over 15 min upon exposure to 10mW visible light.

Preparation of First-Generation XO-CAT•SG Discs. A stock sol-gel mixture was prepared by HCl-catalyzed (pH 1.4) hydrolysis of TMOS. Homogeneity of the solution was reached after sonication for ~20 min at 4 °C. To 1 mL of this solution 1.2 mL of 0.01 M PBS (pH 7.8) and 0.800 mL portions of 4 mg/mL XO and 4mg/mL CAT solution were added. The XO-CAT sol-gel solution was then plated as 0.150 mL aliquots into a 96-well plate and allowed to gel at 4 °C for 48 h. At the end of this gelation period, the multi-well plate was placed in a desiccator for an additional 48 h

at 4 °C to age. The activity of the XO-CAT•SG disc was determined within the wells by incubating the sol-gel pieces with 150 mM HX and monitoring the rate of uric acid formation over 45 min using electronic absorption spectroscopy (Carey 5000 spectrophotometer).

Preparation of Second-Generation Mn(NO)•SG Discs. The NO releasing sol-gel was prepared by adding 14 mg of Mn(NO) to 1.10 mL of a homogenized sol-gel mixture (0.400 mL of Millipore water and 0.700 mL of TMOS) in the dark. This stock solution was then thoroughly mixed and added as 0.600 mL portions to a 24-well plate and stored at 4°C for ~1 week in the dark. The release of NO from the Mn(NO) sol-gel pieces were tested within the wells of the plate with an iNO NO monitoring system over 30 min upon exposure to 10mW visible light.

Preparation of Second-Generation XO-CAT•SG Discs. A stock sol-gel mixture was prepared by HCl-catalyzed (pH 1.4) hydrolysis of TMOS. Homogeneity of the solution was reached after sonication for ~20 min at 4 °C. To 1 mL of this solution 1.2 mL of 0.01 M PBS (pH 7.8) and 0.800 mL portions of 4 mg/mL XO and 4 mg/mL solution were added. The XO-CAT sol-gel solution was then plated as 0.800 mL aliquots into a 24-well plate and allowed to gel at 4 °C for ~1.5 weeks. The activity of XO-CAT•SG discs was determined within the wells in which they were plated, by incubating the sol-gel pieces with 250 mM HX and monitoring the rate of uric acid formation over 45 min using electronic absorption spectroscopy.

Coumarin-7-boronic acid synthesis. Commercially available 7-hydroxycoumarin was first converted to the corresponding triflate in good yield. Using palladium-

mediated Alcaraz-Vaultier borylation, diisopropylaminoborane was utilized as the boron source for the conversion of the triflated intermediate to coumarin-7-boronic acid. Fluorescence Spectroscopy (λ_{ex} = 332 nm, λ_{em} = 440 nm, slit width = 10 nm).

2.10 References

1. Glue, K.; Roell, E, *Z. Anorg. Allg. Chem.,* **1929**, *179*, 233- 266.

2. Koppenol, W.H.; Kissner, R.; Beckman, J.S., *Methods Enzymol*., **1996**, *269*, 296-

3. Alvarez, M. N.; Trujillo, M.; Radi, R., *Methods in Ezymology* **2002**, *359*, 353-366.

4. Reed, J.W.; Ho, H.H.; Jolly, W.L., *J. Am. Chem. Soc.*, **1974**, *96*, 1248-1249.

5. Beckman, J.S., *Chem. Res. Toxicol.*, **1996**, *9*, 836-844.

6. Pfeiffer, S.; Mayer, B., *J. Biol. Chem.*, **1998**, *273,* 27280-27285.

7. Reiter, C. D.; Teng, R.; Beckman, S. J., *J. Biol. Chem.*, **2000**, *275*, 32460-32466.

8. Goldstein, S.; Czapski, G.; Lind, J.; Merenyi, G., *J. Biol. Chem.*, **2000**, *275*, 3031-3036.

9. Bohle, S.; Glassbrenner, P.A.; Hansert, B., *Methods. Enzymol*., **1996**, *269*, 302-311

10. Soulère, L.; Bringaud, F.; Hoffman, P., *J. Heterocyclic Chem.,* **2003**, *40*, 943-947.

11. Feelisch, M.; Ostrowski, J.; Noack, E., *J. Cardiovasc.Pharmacol*., **1989**, *14*, S13.

12, Feelisch, M., *Naunyn-Schiedeberg's Arch. Pharmacol.* 1998, *358*, 113-122.

13. Singh, R.J.; Hogg, N.; Joy, J.; Konorev, E.; Kalyanaraman, B., *Arch. Biochem. Biophys*., **1999**, *361*, 331-339.

14. Alverez, M.N.; Trujillo, M; Radi, R., Methods Enzymol., 2002, 359, 353- 366.

15. deBoer-Maggard, T.R.; Resendez, A.; Mascharak, K, P. *ChemBioChem.*, **2013**, *14*, 2106-2109.

16. Ghosh, K.; Eroy-Reveles, A. A.; Holman, T. R.; Olmstead, M. M.; Mascharak, P. K., *Inorg. Chem*., **2004**, *43*, 2988-2997.

17. Eroy-Reveles, A.A.; Leung, Y.; Mascharak, P.K., *J. Am. Chem. Soc.,* **2006**, *128*,

7166-7167.

18. Wei, Y.; Xu, J.; Feng, Q.; Dong, H.; Lin, M., *Mater. Lett.,* **2000**, *44*, 6-11.

19. (a) Yamanaka, S.A.; Nguyen, N.P.; Ellerby, L.M.; Dunn, B.; Valentine, J.S.; Zink, J.I., *J. Sol-Gel Techn.,* **1994**, *2*, 827-829. (b)Yamanaka, S.A.; Nishida, F.; Ellerby, L.M.; Nishida, C.R.; Dunn, B.; Valentine, J.S.; Zink, J.I., *Chem Mat.*, **1992**, *4*, 495-497.

20. Jeffrey Brinker, George W. Scherer, Sol-Gel Science, Academic Press, 1990.

21. Zielonka, J.; Sikora, A.; Kalyanaraman, B., *J. Biol Chem* **2010**, *285*, 14210-14216.

22. Pacher, P.; Beckman, J.S.; Liaudet, L., *Physiol Res.* **2007**, *87,* 315-424.

23. Kim, K. M.; Henderson, G. N.; Frye, R. F.; Galloway, C. D.; Brown, N. J.; Segal, M. S.; Imaram, W.; Angerhofer, A.; Johnson, R. J., *J. Chromatogr. B.*, **2009**, *877*, 65-70.

Chapter 3. Establishing the Utility of the Peroxynitrite-Generating Platform by Probing Peroxynitrite-Mediated Nitration of Tyrosine

3.1 Background

In the previous chapter, the successful construction of a PN-generating platform is described. This platform is capable of affording PN *in situ*, where NO and $O_2^{\bullet-}$ are generated from independent sources.[1] Great attention was placed on designing, synthesizing, and characterizing this unique system. The utility of the platform still needed to be established. We decided to explore the application of the platform to demonstrate the hallmark nitration of tyrosine.[2,3] Over the course of the last decade, the nitration of tyrosine has become the center of inflammation-mediated disease states ranging from atherosclerosis to Alzheimer's disease.[4,5] And perhaps more noteworthy is the hypothesis that tyrosine nitration is strongly mediated by PN.[5-10]

In the early 1990's seminal work by Beckman and coworkers showed that PN selectively nitrated one of the four tyrosine residues of superoxide dismutase (SOD) by crystallographic analysis.[11] Since this report, the vast majority of PN research has been dedicated to understanding not only the pathophysiological significance of PN-mediated nitration but also the potential of this post-translational modification as a physiological or developmental signaling pathway. The latter are of research has introduced the question, can PN-mediated nitration of tyrosine be the new phosphorylation?[12,13] Estévez and coworkers have recently provided support to this possibility, when it was shown that the extent of tyrosine nitration within fetal rat hearts varied with developmental progress described as "temporal patterns of tyrosine nitration."[14]

Interestingly, as the connection between PN and both physiological and pathophysiological continues to strengthen little to no work has been completed to advance the synthetic technologies of PN generation. For this reason we chose to study the chemistry of PN-mediated nitration of tyrosine within our designed PN-generating platform. The results described below established our platform as a powerful tool that could be employed to study a vast array of NO, $O_2^{\bullet-}$, and PN chemistry.

3.1.1 Mechanism of PN-mediated Nitration

3-Nitrotyrosine, the product of tyrosine nitration, has long been identified through immunblotting of tissue samples collected from patients known to have suffered from sustained or chronic inflammation.[15] While alternative modes of tyrosine nitration such as the nitrite (NO_2^-) and myeloperoxidase (MPO) pathway have been elucidated,[16] PN remains the most widely accepted mediator of this post-translational modification. The nitration of tyrosine by PN proceeds through two distinct paths. The first and most direct path is through the homolytic cleavage of peroxynitrous acid (ONOOH, highlighted in blue in Figure 3.1) to form the strong oxidant hydroxyl radical ($^{\bullet}OH$, E° = 2.31 V) and the nitrating agent nitrogen dioxide ($^{\bullet}NO_2$). The second path involves the formation of reactive intermediate anion nitrosoperoxocarbonate ($ONOOCO_2^-$, highlighted in gray in Figure 3.1). Homolytic cleavage of this intermediate species yields strong oxidant carbonate radical ($CO_3^{\bullet-}$, E° = 1.78 V) and nitrating agent $^{\bullet}NO_2$. However, both paths ultimately induce the oxidation of tyrosine to from a tyrosyl radical (Tyr-O$^{\bullet}$) that can then rapidly

combine with $^{\bullet}NO_2$ to form the nitrated product 3-nitrotyrosine (3-NT) as shown in Figure 3.2.

The second pathway most commonly predominates under physiological conditions where the pH is 7.4 and CO_2 can be present in mM concentrations. If we were to assume that oxidants $^{\bullet}OH$ and $CO_3^{\bullet-}$ and nitrating agent $^{\bullet}NO_2$ were generated as discrete secondary radicals from PN decomposition, comparison of the oxidant capacity predicts that nitration of tyrosine would be most favored under more acidic conditions where the formation of strong oxidant $^{\bullet}OH$ would be maximized. Yet the contrary is observed. This contradiction can be fully rationalized when we consider the continuum of PN breakdown that are taking place under various experimental conditions. For example, a closer look at the ONOOH-derived pathway shows that while $^{\bullet}OH$ and $^{\bullet}NO_2$ correspond the radicals required for nitration of tyrosine this homolytic decomposition occurs secondary (30%) to isomerization of the acid to nitrate (70%).[17] While isomerization can also occur through the $ONOO^-$, protonation of the anion results in a significant diminution in the energy barrier associated with this pathway (Figure 3.1, bottom panel), ultimately decreasing the lifetime of PN.

For this reason the CO_2-directed nitration pathway is believed to lead to maximal nitration of tyrosine through the formation of the $ONOOCO_2^-$ intermediate upon reaction of PN with CO_2 (Figure 3.1). Two mechanistic pathways of nitration have been proposed that vary only in the mode of decomposition of $ONOOCO_2^-$.

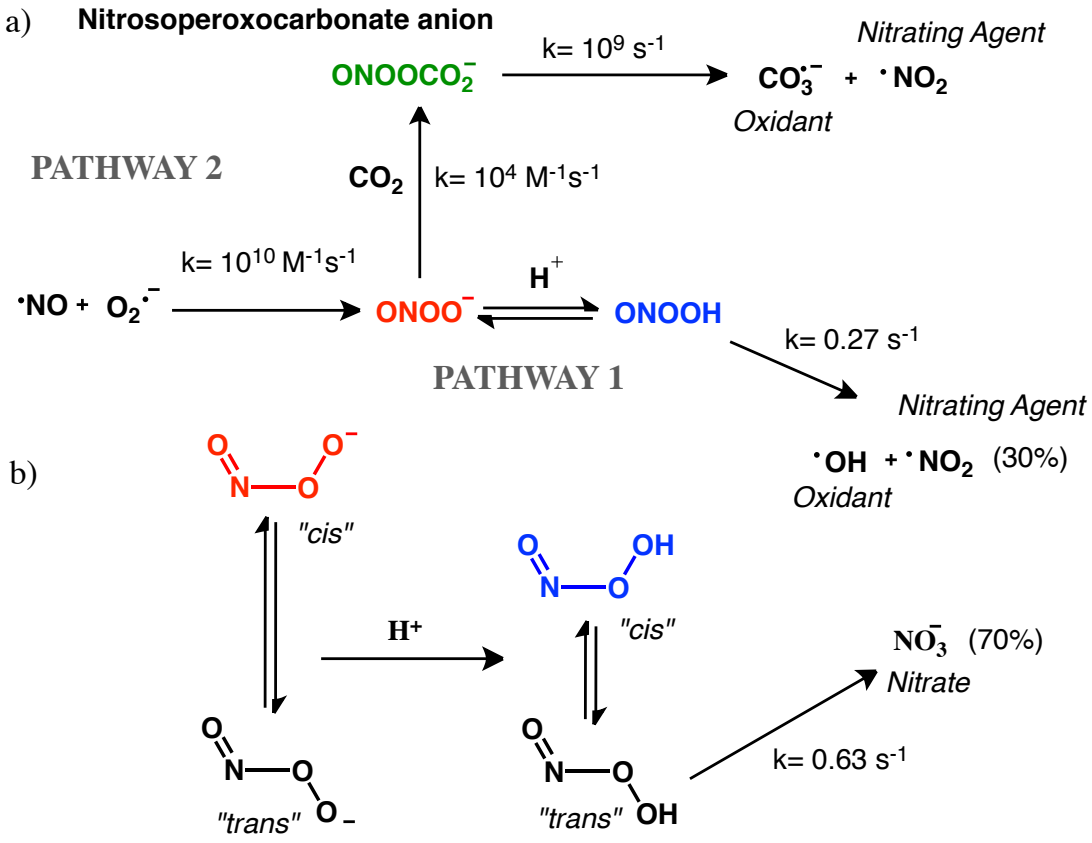

Figure 3.1. Reaction schemes highlighting the chemical pathways that promote or inhibit nitration of tyrosine by PN. The fundamental nitrating pathways are shown in (a), while the competing isomerization pathway that leads to nitrate formation is shown in (b).

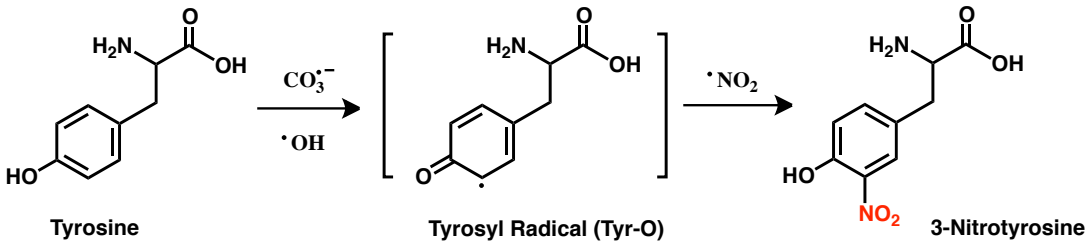

Figure 3.2. Representative mechanism of PN-mediated nitration of tyrosine

The first predicts a more direct radical-radical interaction where homolytic cleavage of $ONOOCO_2^-$ along the peroxo O-O bond yields $^{\bullet}NO_2$ and CO_3^{2-}. In constrast, the second proposed mechanism suggests a rearrangement event of $ONOOCO_2^-$ to the nitrocarbonate anion $O_2NOCO_2^-$ that yields nitrosyl cation (NO_2^+) and carbonate anion (CO_3^{2-}) via a heterocleavage of the intermediate species.[18,19] Regardless of the pathway it has been accepted that the presence of CO_2 significantly enhances the nitration of tyrosine by PN through the formation of $ONOOCO_2^-$.

3.1.2 Detection of 3-Nitrotyrosine (3-NT)

Because tyrosine nitration was chosen as a probe to measure the efficiency of PN formation within the wells, it is relevant to discuss the modes of detection that can be employed. Electronic absorption spectroscopy has been one of the primary tools of 3-NT detection, because the addition of a nitro group to the phenol moiety of tyrosine results in significant changes in the absorption profile of tyrosine. The nitro group itself can be considered a chromophore that displays a strong absorbance at 220 nm.[20] Attachment of the chromophore to the phenol moiety of tyrosine results in a shift of the λ_{max} value of unmodified amino acid from 280 nm to ~350 nm, under slightly acidic conditions. Further, modulation in the pH can assist in confirming the addition of the nitro group to tyrosine because the absorbance band of 3-NT shifts towards lower energy wavelengths (450 nm) under basic conditions. These characteristic absorption profiles can be further exploited in the detection of 3-NT by high-pressure liquid chromatography that are equipped with multi-channel diode array detectors.

The second most common technique employed to detect nitration of tyrosine or a tyrosine residue is mass spectrometry.[21] However, it is important to note there could be significant variability in the relative intensities of the peaks that correspond to the parent and fragmentation species depending upon the mass spectrometer chosen. One common variation often observed is the relatively abundance of the parent peak corresponding to the nitrated product or its fragmentation peak. For example the mass spectrum of 3-NT contains a large 181 m/z peak that corresponds to a loss of a $-NO_2$ group and a much smaller parent ion peak at 227 m/z. For this reason it is strongly recommended to pair HPLC and MS methods to assure that the fragmentation peaks observed in MS spectrum are solely the fragmentation species and not unreacted tyrosine (($[M+H]^+$ = 182 m/z). As expected, the mass spectrum of crude samples consists of both 181 m/z and 182 m/z peaks when obtained from a Micromass ESI-MS.

3.1.3 Experimental Rationalization

Because of the intricate details of the mechanistic pathways that govern nitration of tyrosine by PN it is necessary to establish the utility of the designed PN-generating platform. A single plate could be constructed to corroborate the effects of pH and the presence of thiols on the PN-mediate nitration of tyrosine. The following sections highlight the results observed in our platform. These results have been compared with results obtained from alternative PN sources when appropriate.

3.2 Tyrosine Nitration in the PN-Generating Platform

The process of establishing the utility of our two-component PN-generating platform began with experiments designed to monitor the effect of pH on the nitration of free tyrosine by PN. The formation and quantification of 3-NT formed was first evaluated by electronic absorption spectroscopy (λ_{max} = 356 nm). Standard solutions of 3-NT were prepared to optimize the extinction coefficient of this species under the defined experimental conditions and calculated to be 4015 $M^{-1}cm^{-1}$. As predicted, it was observed that increased acidity of the well content from pH 7.4 to 7.0 to 6.5 resulted in a general diminution of tyrosine nitration by PN (Table 3.1). As expected, decrease in the pH towards the pK_a of PN (6.8), inhibits the formation of $ONOOCO_2^-$ (Figure 3.1) and diminishing the extent of tyrosine nitration. Mass spectrometry (ESI, positive ion mode) corroborates 3-NT formation with the presence of the corresponding peak at 227 m/z $[M+H]^+$. Control studies were completed at pH 7.4 where the flux ratio of NO: $O_2^{\bullet-}$ was varied from 1:1 to 1:2. Such changes resulted in a near elimination in tyrosine nitration as the flux ratio reached 1:2.

Table 3.1. Percent nitration of tyrosine under various pH conditions
(Values calculated based on total PN concentration)

Sample	pH	Percent Nitration
Tyrosine	7.4	38.5 ± 0.4 %
Tyrosine	7.0	30.4 ± 0.4 %
Tyrosine	6.5	22.2 ± 0.3 %

The significance of these results is two fold. First, they validate the efficacy of PN formation in the wells of the platform because exposure of 1 mM of tyrosine to PN in the wells PN for 30 min afforded 46.5 μM of 3-NT (38.5 ± 0.4% nitration based on PN concentration). This yield is particularly notable when compared to ~1% tyrosine nitration obtained with 1 mM of SIN-1 (and comparable CO_2 concentration and pH) after 12 h as reported by Mayer and coworkers.[25] Second, it established the flexibility of the system to study PN-related chemistry under a spectrum of pH conditions. This feature of the platform posed as a large obstacle for alternative two-component options because many NO donors are highly pH sensitive and only release optimal fluxes of NO under strict conditions.[26]

3.3 Nitration of Peptide Y1 and Effects of CO_2

To extend the biochemical complexity of the PN substrate within the prefabricated platform, we designed and synthesized a model peptide **Y1** (sequence AAAAAKKAAA**Y**AAAKK) that contained a single tyrosine residue amenable to nitration. Exposure of **Y1 (**0.25 mM) to PN (0.250 mM hypoxanthin (HX), and 4 mM $NaHCO_3$) within the wells of a second-generation PN-generating platform (24-well plate) afforded similar extent of nitration compared to those observed in the studies where free L-tyrosine was subjected to the same conditions (37.2 ± 1.1 % Y1, compared to 38.5 ± 0.4 % free L-tyrosine). Nitration of the single tyrosine residue within the peptide was first verified by electronic absorption spectroscopy; a peak centered at 370 nm indicated the formation of 3-NT (Figure 3.3). Mass spectral

results confirmed the presence of this modification with a mass increase of 46 Da ($-NO_2$) indicative of nitration of the model peptide ($[M+3H]^{3+}$ = 521 m/z). The sodium adduct was also observed at 529 m/z. All discussed peaks are shown in Figure 3.4 in addition to a large 506 m/z corresponds to the $[M+3H]^{3+}$ peak of the unmodified parent peptide.

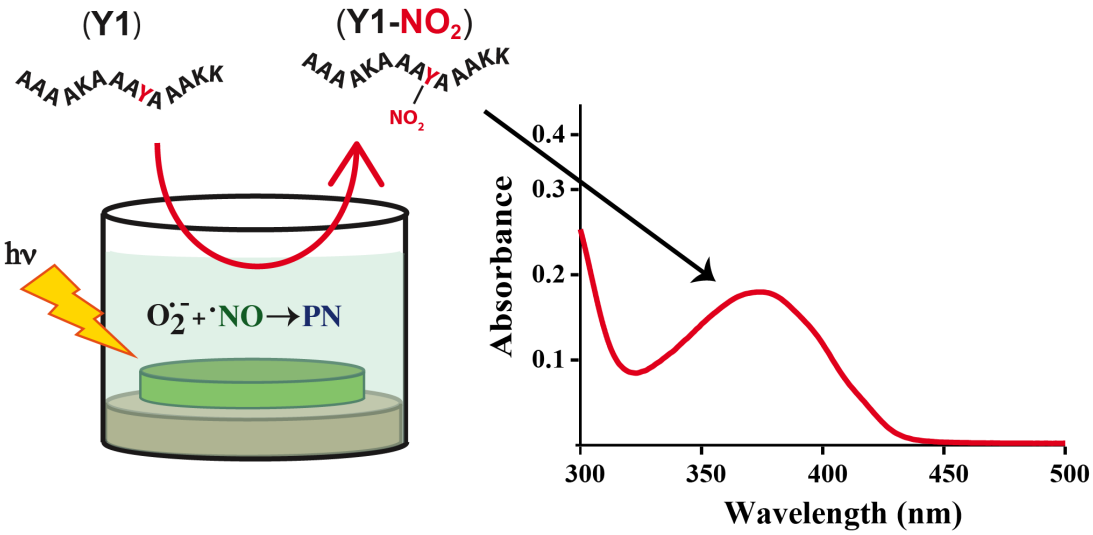

Figure 3.3. (Left) Illustration highlighting a single PN-generating well. (Right) The electronic absorption spectrum of the well content collected after Y1 was exposed to PN for 30 min. The absorbance band highlighted in red corresponds to the absorption band of the nitrated tyrosine residue within **Y1**.

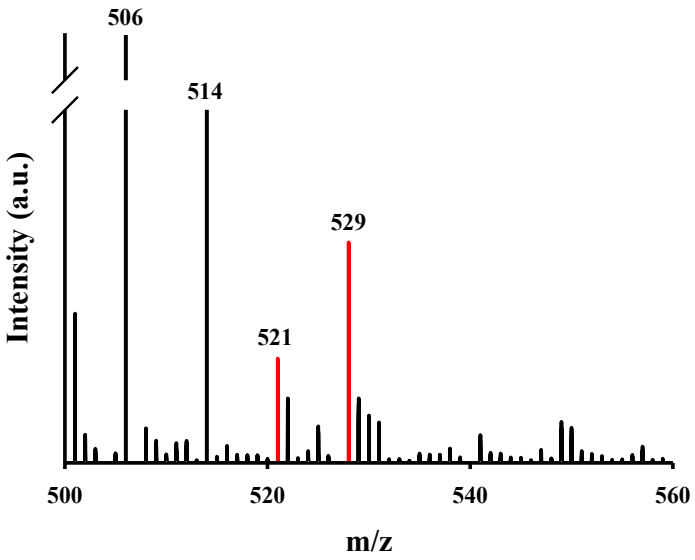

Figure 3.4. Mass spectrum of the well content collected after **Y1** was exposed to PN. The two peaks highlighted in red correspond to the $[M+3H]^{3+}$ (521 m/z) and $[M+Na]^{3+}$ (529 m/z) of the nitrated **Y1** peptide.

To observe the effects of CO_2 on PN-mediated nitration of tyrosine we modulated the $NaHCO_3$ concentration (source of CO_2) within three PN- generating wells. As discussed above, the presence and concentration of CO_2 mediates PN-dependent nitration through the formation of intermediate $ONOOCO_2^-$ that decomposes to yield $CO_3^{\bullet-}$ and $^{\bullet}NO_2$.[27] Indeed, alteration of the CO_2 concentration within the wells of our platform resulted in significant changes in the extent of nitration of the tyrosine residue of **Y1**. With a CO_2 concentration of ~100μM, a modest increase in nitration was observed compared to wells where no $NaHCO_3$ was incorporated (Table 3.2). However, when the concentration of CO_2 was approximately tripled, a significant increase in nitration was observed (~4.5 fold). Taken together these results confirm the flexibility of the PN-generating platform.

Table 3.2. Percent nitration of **Y1** at pH 7.4 under various $NaHCO_3$ concentrations (Values calculated based on total PN concentration)

Sample	Percent Nitration	[$NaHCO_3$]
Y1	2.8 ± 0.5 %	0 mM
Y1	7.7 ± 0.9 %	1.25 mM
Y1	37.2 ± 1.1 %	4.0 mM

3.4 Nitration of Peptide Y1 and Intermolecular Effects of Glutathione

Next, to investigate the effects of antioxidants on the nitration of tyrosine within the designed peptide, we added the biologically relevant antioxidant thiol glutathione (GSH) into the PN-generating wells. Similar to the experimental system described above, three wells were prepared with 0.25 mM of the peptide, 0.4 mM HX, and 4 mM $NaHCO_3$ and supplemented with glutathione (1 mM, comparable to biological levels). After 30 min of undulation and illumination, the reactions was terminated and the well contents were assembled as discussed above. Incorporation of GSH did not inhibit tyrosine nitration within **Y1** and instead resulted in a slight (~1.1-fold, 39.2 ± 1.2%) enhancement. Analysis of the well content collected from this experiment by mass spectrometry revealed the selective nitration of **Y1**, indicated by the presence of a peak at 521 m/z. Although control studies performed in the absence of **Y1** showed a small peak at 353 m/z correlating to the nitration of GSH in addition to a moderately strong peak at 360 m/z $[M+Na]^+$ due to S-nitrosylated GSH, the presence of **Y1** in the well resulted in the small peak at 360 m/z $[M+Na]^+$ only (Figure 3.5).

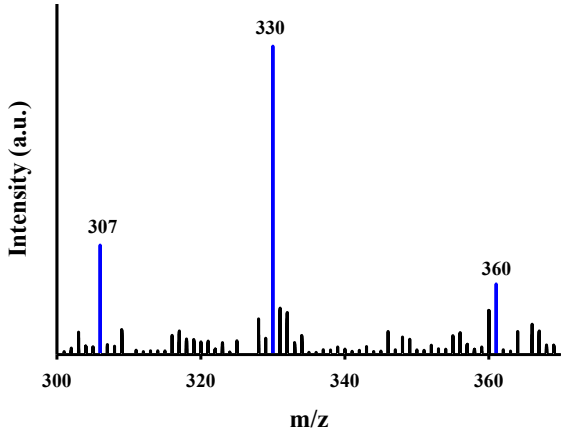

Figure 3.5. Partial mass spectrum collected from the well content where **Y1** was exposed to PN in the presence of GSH

The slight *enhancement* in the extent of nitration of **Y1** in the presence of GSH was proposed to be due to the extended lifetime of NO within the wells of our platform. The photorelease of NO from the Mn(NO)•SG piece is fast compared to the initial release of $O_2^{\bullet -}$ from the XO/CAT•SG disk that requires diffusion of HX (XO substrate) through the sol-gel matrix in the larger well. Therefore in the first minute or so of the experiment when the release rates are slightly unmatched, NO chemistry predominates and results in the nitrosylation of GSH.[28,29] The resulting S-nitrosylated glutathione product (S-nitrosoglutathione, GSNO) acts as a NO storage in the platform (much like in the body), extending the effective concentration of this precursor within the wells. This hypothesis is supported by mass spectral results of the well content where a peak corresponding to GSNO was observed (Figure 3.5). Extension of the lifetime of NO in the wells by this route allows for a higher concentration of PN at the later part of the reaction and results in the moderately higher yield of nitrated product under such conditions.

3.5 Nitration of Peptide Y1 and Intramolecular Effects of Thiols

The observed enhancement in nitration of **Y1** in the presence of thiol GSH prompted us to design a series of peptides to study *intramolecular* effects of thiols on the nitration of tyrosine within our platform. Four model peptides were synthesized (primary sequence of tyrosine and cysteine-containing peptides are shown in Table 3.3), three of which contained a single cysteine and a single tyrosine separated by varied 8, 4, and 0 amino acids between them (**CY1**, **CY2** and **CY3**, respectively) and one control peptide that contained only a single cysteine residues (**C1**).

It has been observed that the relative proximity of thiols to tyrosine residues within peptide and proteins can influence the extent of tyrosine nitration by PN and contribute to the general selectivity of this dynamic process through an intramolecular radical transfer pathway.[30,31] As expected, when tyrosine and cysteine residues were placed directly adjacent to each other in peptide **CY3** a significant attenuation in nitration of the tyrosine residues was observed compared to **CY1** and **CY2** (Table 3.3). However, separation of these residues by four or eight amino acids yielded no significant change in nitration of the tyrosine compared to **Y1**. The presence of a cysteine residue directly adjacent to the induced tyrosyl in **CY3** acts as a "radical sink," inhibiting the nitration process and enhancing the reactivity of the thiol residue.[32-35] The absorption spectra of **CY1**, **CY2**, and **CY3** are shown in Figure 3.6.

Table 3.3. Intramolecular effects of cysteine on nitration of tyrosine in designed peptides (Values calculated based on total PN concentration)

Peptide	Sequence	Percent Nitration
CY1	AAA**C**AAAKKAAA**Y**AAAKK	39.1 ± 1.5 %
CY2	AAAKAAA**C**KAAA**Y**AAAKK	41.7 ± 1.8 %
CY3	AAAKKAAA**CY**AAAKK	4.8 ± 0.7 %

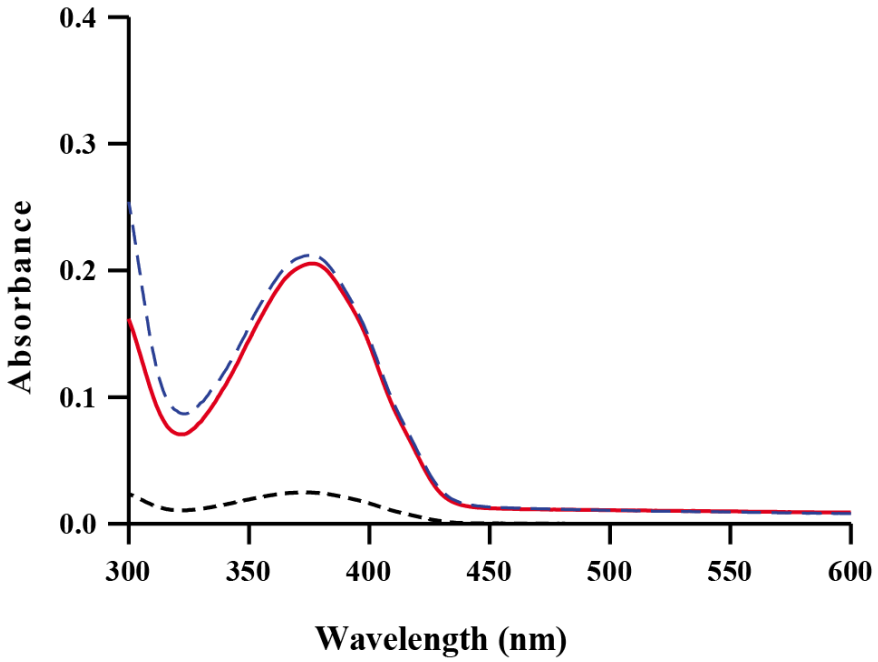

Figure 3.6. Electronic absorbance spectrum of model peptides **CY1 (solid red)**, **CY2 (dotted blue)**, and **CY3 (dotted black)** following exposure of each to PN within the wells of the platform.

This radical transfer between the tyrosyl radical and cysteine residue was further emphasized in mass spectral results. Mass spectral data collected from the **CY3** study contained peaks corresponding to 16 Da (−O), 30 Da (−NO), and 46 Da ($-NO_2$) mass additions to the parent peptide (Figure 3.7). While the 30 Da and 46 Da mass additions (representing nitrosylation and nitration respectively) were observed in all three peptide studies, the relative intensity of the peaks varied. In the mass spectra of **CY1** and **CY2**, the 46 Da a mass addition was the predominant peak, whereas in **CY3**, the 30 Da a mass addition was observed to be significantly greater than the nitrosylation peak.

The electronic spectrum collected of the well content from the **CY3** study also showed a significant diminution of the absorbance band corresponding to the nitrated tyrosine (λ_{max}= 370 nm), indicating that the 46 Da mass addition observed in the mass spectrum was largely a result of S-nitration of the cysteine residue within the peptide. The mass addition of 16 Da to the **CY3** peptide is a unique product that was not observed in **CY1** and **CY2** studies and likely corresponds to the oxidation of the thiol group to a sulfenic acid (−SOH). It is important to note here that the extent of nitration within peptide **CY1** and **CY2** (where the cysteine and tyrosine residues were 4 or 8 residues apart) were not significantly different (Table 3.3). Furthermore, the relative nitration of **CY1** and **CY2** was similar to that observed when **Y1** peptide was exposed to PN in the presence of GSH. The absorption spectra of respective control **CY1** studies are shown in Figure 3.8.

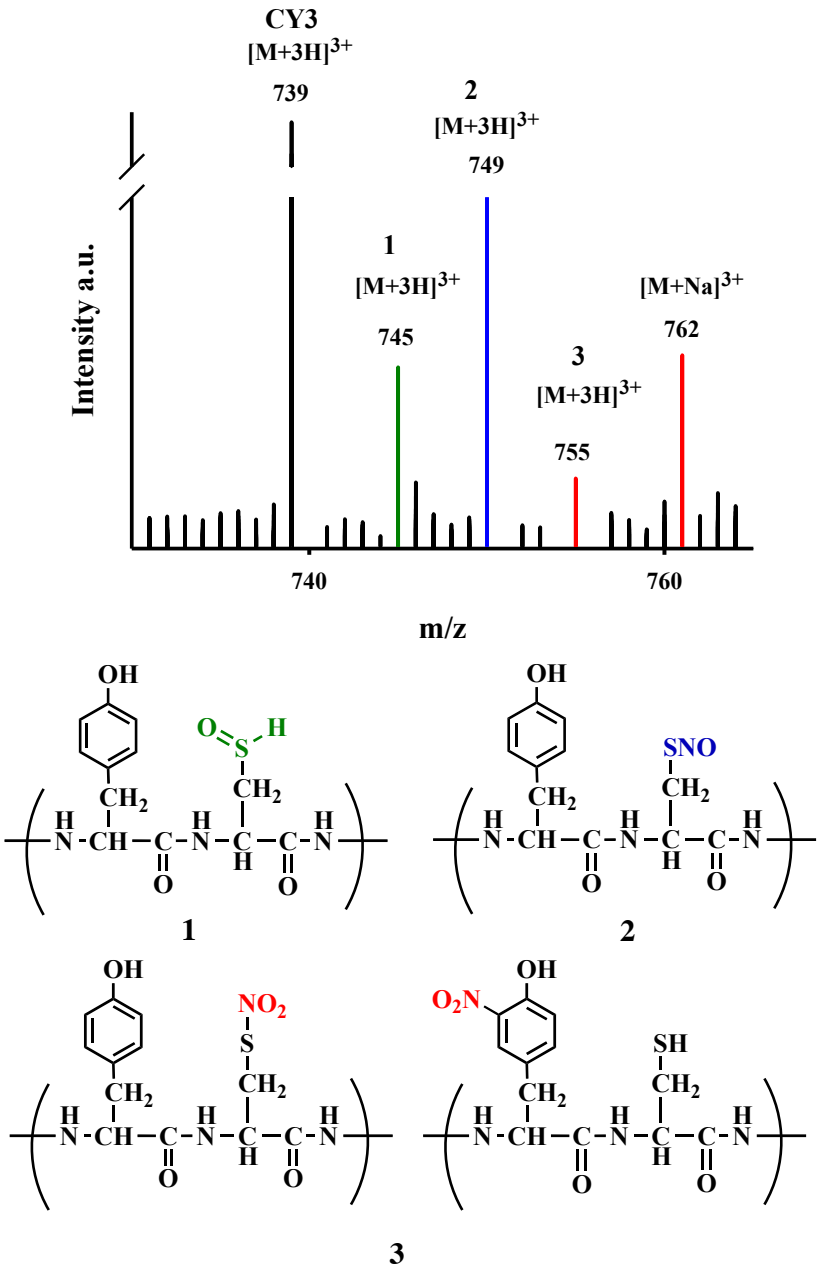

Figure 3.7. (**Top**) Mass spectrum of the well content collected after **CY3** was exposed to PN for 30 min. The mass spectral data showed mass additions of 16 Da, 30 Da, and 46 Da corresponding to possible peaks 745 m/z (green), 749 m/z (blue), and 755 m/z (red), respectively. (**Bottom**) Structures representative of the potential products associated with the observed additions in the mass spectrum.

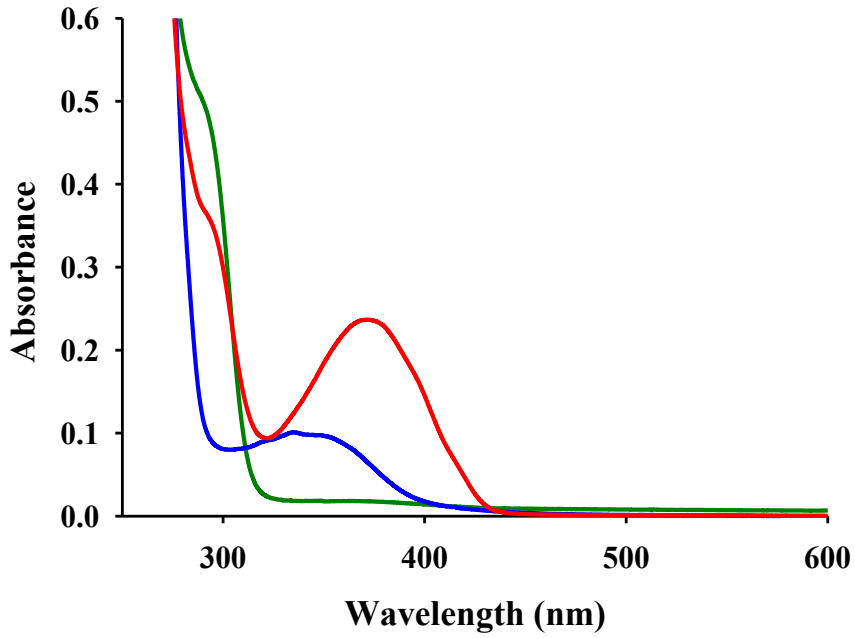

Figure 3.8. Electronic absorption spectrum of **CY1** peptide in the presence of NO (blue line), $O_2^{\bullet-}$ (green line) and PN (red line).

3.6 Conclusion

Taken together, the body of work discussed above demonstrates the utility of the two-component PN-generating platform as a convenient tool to study the reactions of PN with a wide range of substrates under controlled conditions. Previously, poor nitration yields by *in situ* generated PN compared to yields generated upon exposure to authentic PN has been rationalized by Ingold and coworkers to be a result of varied rates of radical formations by the respective sources.[36] A rapid rate of NO photorelease from Mn(NO)•SG and careful matching of the flux ratio of NO and $O_2^{\bullet-}$ make this platform a valuable tool to study *the effects of continuous exposure of a substrate to PN*. The efficient nitration of tyrosine and tyrosine-containing

peptides by physiologically relevant concentration of PN within the wells provide strong evidence in favor of the utility of this platform in future studies on PN chemistry.

3.7 Methods

All chemicals used were analytical or ACS grade and received from chemical suppliers, unless otherwise stated. Platform components tetramethoxyorthosilicate (TMOS), hypoxanthine (HX), and xanthine oxidase (XO) were purchased from Sigma-Aldrich. All peptides synthesized were assembled on a Rink-amide ChemMatrix® resin purchased from Sigma-Aldrich, and required amino acids were purchased from AAPPTec.

Preparation of the PN-generating platform. Prefabricated 24-well plates were synthesized as previously described in the Chapter 2.[1] Five-fold increase of all components was required to compensate for the increased well size in the present work. In short, to a stock solution of hydrolyzed TMOS solution $[Mn(Papy_3)(NO)]ClO_4$ (Mn(NO)) was added and allowed to stirred until the nitrosyl was completely dissolved. A batch of 0.600 mL of this stock Mn(NO) solution was then added to individual wells and allowed to dry and age for 1 week prior to use. The final Mn(NO)-encapsulated sol-gel discs (Mn(NO)•SG) were stored at 4 ^{o}C in the dark prior to use.

In a second 24-well plate, a batch of 0.800 mL of a xanthine oxidase/catalase containing sol-gel (XO/CAT•SG) mixture were plated into individual wells and

allowed to dry and age for 1.5 weeks. Prior to their use, these enzyme encapsulated sol-gel discs were washed three times and their activity was evaluated by electronic absorption spectroscopy.[1] Construction of the PN-generating platform was completed by adding a single Mn(NO) sol-gel disc to each well of a 24-well plate with XO/CAT•SG layered at the bottom (Figure 3.3). Generation of PN within the wells was initiated with the addition of hypoxanthine (HX) and concomitant illumination of the plate with low power broadband light (10 mW, Electrofiberoptics Corporation 410 illumination). The release of PN from the individual wells was confirmed and quantitated to be 4.42 ± 0.22 mM per min using the PN probe coumarin-7-boronic acid.[37]

Peptide Synthesis and Purification. All peptides were synthesized using Fmoc synthesis on a Liberty 1 Peptide Synthesizer with Discover® microwave platform (CEM, Matthews, NC). The syntheses were performed on a 0.1 mmol scale, and monitored with PepDriver software. The deprotection of the Fmoc group was achieved using a solution of 20% piperidine in dimethylformamide (DMF). Solutions of 0.625 M diisopropylcarbodiimide and 1.25 M hydroxybenzotriazole in DMF were used to activate the carboxy-termini. All coupling reactions were performed at 4 equivalents of Fmoc-amino acid, and each amino acid was double coupled and capped with a 10% acetic anhydride solution. Fully synthesized peptides were washed with dichloromethane and split into two reaction vessels for cleavage.

A cleavage cocktail consisting of 15 ml of trifluoroacetic acid, 0.5 ml each of 1,2-ethanedithiol and liquefied phenol, and 1 ml of triisopropylsilane, was added to each vessel of dried resin and reacted for 2 h followed by filtration. The filtrate was added to 90 ml of cold, dry diethyl ether for precipitation. The precipitate was collected by centrifugation, and the ether was discarded. The resulting pellet was dissolved in 20 mL of 1:1 H_2O/acetonitrile (1% formic acid) and lyophilized.

Peptides were purified by RP-HPLC on a Vydac (Hesperia, CA) preparative C18 column. Fractions were collected and analyzed by electron spray ionization mass spectrometry (ESI-MS) on a Micromass (Wythenshawe, UK) ZMD mass spectrometer to confirm the correct molecular weight. Fractions containing the correct molecular weight were combined and lyophilized. Further purification was performed on a semi-preparative scale as needed. Peptides were quantified using UV absorbance at 280 nm.

Circular Dichroism. Far-UV CD measurements were performed with an AVIV 60DS spectrophotometer using a 0.1 cm path length cuvette. Peptides were prepared at 0.150 mM concentration in 50 mM phosphate-buffered saline (PBS) at pH 7.4. Spectra were recorded from 260 to 200 nm with a step size of 1 nm, a bandwidth of 1.5 nm, and an averaging time of 8 s. An average of 16 scans was obtained for each spectrum.

Nitration of free tyrosine by PN under varied pH conditions. In a prefabricated 24-well PN-generating plate, three wells were prepared under three pH conditions (0.01M phosphate buffer, pH 7.4, 7.0, and 6.5). To each well, stock solutions of

tyrosine, $NaHCO_3$ and hypoxanthine were added to achieve a final concentration of 1 mM, 1.25 mM and 0.4 mM, respectively. Immediately following the addition of these stock solutions, the multi-well plate was illuminated with a low power broadband light source and allowed to mix on a plate rocker for 30 min. Termination of the reaction was completed by simply removing the reaction mixture from the plate and then transferring the analyte into a 1 mL centrifuge tube. This solution was centrifuged down to ensure absence of free-floating particulates. Samples were then analyzed by electronic absorption spectroscopy (Cary 5000 Spectrophotometer) and ESI-MS to confirm and quantitate 3-NT formation.

Nitration of tyrosine by PN within a model peptide. In a prefabricated 24-well PN-generating platform, investigation into the nitration of a model tyrosine-containing peptide (**Y1**, sequence AAAAAKKAAA**Y**AAAKK) by PN was performed by preparing three wells with 0.25 mM of the peptide, 0.4 mM HX, and 4 mM $NaHCO_3$. The plate was allowed to undulate on a plate rocker for 30 min while being illuminated by a low power broadband light source. The well content was then transferred to a 0.5 mL Eppendorf tube, centrifuged, and then analyzed by electronic absorption spectroscopy and mass spectrometry. Additionally, the effect of CO_2 on this PN-dependent reaction was evaluated by modulating the concentration of $NaHCO_3$ (0 mM, 1.25 mM, and 4 mM) in wells prepared as described above.

Nitration of tyrosine by PN within Peptide Y1 in the presence of GSH. Similar to the experimental system described above, three wells were prepared with 0.25 mM of the peptide, 0.4 mM HX, and 4 mM $NaHCO_3$ and supplemented with

glutathione (1 mM). After 30 min of undulation and illumination, the reactions were terminated and evaluated as discussed above.

Modification of cysteine within a model peptide. In a prefabricated 24-well PN-generating platform, investigation on the modification of a model cysteine-containing peptide (**C1**, sequence AAAAAKKAAA**C**AAAKK) by PN was performed by preparing three wells with 0.25 mM of the peptide, 0.4 mM HX, and 4 mM $NaHCO_3$. Solutions were treated and evaluated as discussed above. Additionally, control wells were prepared where **C1** was exposed to NO only (these wells excluded HX). Cysteine nitrosylation was then quantified by electronic absorption spectroscopy (λ_{max} = 336 nm, ε = 920 $M^{-1}cm^{-1}$) and employed as a correction factor.

Nitration of tyrosine by PN within model peptides each containing a cysteine residue. Three peptides were designed with varied relative distance between a cysteine and tyrosine residues: **CY1**, sequence AAA**C**AAAKKAAA**Y**AAAKK; **CY2**, sequence AAAKAAA**C**KAAA**Y**AAAKK; and **CY3**, sequence AAAKK-AAA**CY**AAAKK. In the prefabricated 24-well PN-generating platform, the intramolecular effect of thiols on the nitration of tyrosine in these peptides by PN was monitored. Three wells were prepared with 0.25 mM of the peptide, 0.4 mM HX, and 4 mM $NaHCO_3$. Solutions were treated and evaluated as discussed above. Additional control studies were completed with peptide **CY1**, where the peptide was exposed to NO or $O_2^{\bullet -}$. All other previously described parameters and protocols were maintained in these studies unless otherwise noted. Control studies on the

effects of NO or $O_2^{\bullet-}$ were performed by removing the Mn(NO)•SG or XO/CAT•SG disc from the wells.

3.8 References

1. deBoer, T.R.; Resendez, A.; Mascharak, P.K., *ChemBioChem*, **2013**, *14*, 2106-2109.

2. Szabo, C.; Ischiropoulos, H.; Radi, R., *Nat. Rev. Drug Discov*., **2007**, *6*, 662-680.

3. Pacher, P.; Beckman, J. S.; Liaudet, L., *Physiol. Rev.,* **2007**, *87*, 315-424.

4. Greenacre, S.; Ischiropoulos, H., *Free Rad. Res.,* **2000,** *34*, 541-581.

5. Chan, P. H., *J. Cereb. Blood Flow Metab*., **2001**, *21*, 2-14.

6. Reynolds, R. M.; Berry, W. R.; Binder, I. L., *Biochemistry*, **2005**, *44*, 1690-1700.

7. Lee, R. J.; Kim, K. J.; Lee, J. S.; Kim, P. K., *Arch. Pharm. Res*., **2009**, *32*, 1109-1118.

8. Cantoni, O.; Palomba, L.; Guidarelli, A.; Tommasini, L.; Cerioni, L.; Sestili, P., *Environ. Health Perspect.*, **2000**, *110*, 823-82.

9. Torreilles, F.; Salman-Tabcheh, S.; Guerin, M. C.; Torreilles, J., *Brain Res. Rev.*, **1999**, *30*, 153-16.

10. Smith, M. A.; Richey Harris, P. L.; Sayre, L. M.; Beckman, J. S.; Perry, G., *J.*, *Neurosci.*, **1997**, *17*, 2653-2657.

11. Ischiropoulos, H.; Zhu, L.; Chen, J.; Tsai, M.; Martin, J.C.; Smith, C.D.; Beckman, J.S., *Archiv. Biochem. Biophys*., **1992**, *298*, 431-437.

12. Mannick, J.B.; Schonhoff, *Arch. Biochem. Biophys*., **2002**, *408*, 1-6.

13. Monteiro, H.P., *Free Radical Biol. Med.*, **2002**, *33*, 765-773.

14. Viera, L.; Radmilovich, M.; Vargas, M.R.; Dennys, C.N.; Wilson, L.; Barnes, S.; Franco, M.C.; Beckman, J.S.; Estévez, A., *Free. Radical Biol. Med.*, **2013**, *55*, 101-108.

15. Ischiropoulos, H.; *Arch. Biochem. Biophys.,* **1998**, *356*, 1-11.

16. Zhang, H.; Zielonka, J.; Sikora, A.; Joseph, J.; Xu, Y.; Kalyanaraman, B., *Arch. Biochem. Biophys*., **2009**, *484*, 134-145.

17. Quijano, C.; Romero, N.; Radi, R., *Free Radic. Biol. Med.,* **2005**, *39*, 728-741.

18. Uppu, R.M.; Squadrito, G.L.; Pryor, W.A., *Arch. Biochem. Biophys*., **1996**, *327*, 335-343.

19. Gow, A.; Duran, D.; Thom, S.R.; Ischiropoulos, H., *Arch. Biochem. Biophys*., **1996**, *333*, 42-48.

20. Nauser, T.; Koppenol, W.H.; Pelling, J.; Schöneich, C., *Chem. Res. Toxicol*., **2004**, *17*, 1227-1235.

21. Tsikas, D.; Duncan, M.W.; *Mass Spectrom. Rev.,* **2014**, *33*, 237-276.

22. Radi, R., *J. Biol. Chem.*, **2013**, *288*, 26464-26472.

23. Ferrer-Sueta, G.; Radi, R., *ACS Chem. Biol.*, **2009**, *4*, 161-177.

24. Trujillo, M.; Naviliat, M.; Alvarez, N. M.; Peluffo, G.; Radi, R., *Analusis.*, **2000**, *28*, 518-527.

25. Pfeiffer, S.; Mayer, B., *J. Biol. Chem.*, **1998**, *273,* 27280-2728.

26. Feelisch, M., *Naunyn-Schiedeberg's Arch. Pharmacol.*, **1998**, *358*, 113-122.

27. Carballal, K.; Bartesaghi, S.; Radi, R., *Biochim. Biophys. Acta,* **2013**. *1840*, 768-780.

28. Stamler, S. J.; Simon, I. D.; Osborn, J. A.; Mullins, M. E.; Jaraki, O.; Michel, T.; Singel, D. J.; Loscalzo, J., *Proc. Natl. Acad. Sci*., **1992**, *89*, 444-448.

29. Mayer, B.; Schrammel, A.; Klatt, P.; Koesling, D.; Schmidt, K., *J. Biol. Chem.*, **1995**, *270*, 17355-17360.

30. Zhang, H.; Zielonka, J.; Sikora, A.; Joseph, J.; Xu, Y.; Kalyanaraman B., *Arch. Biochem. Biophys.*, **2009**, *484*, 134-145.

31. Zhang, H.; Xu, Y.; Joseph, J.; Kalyanaraman, B., *J. Biol. Chem.*, **2005**, *280*, 40684-40698.

32. Petruk, A. A.; Bartesaghi, S.; Trujillo, M.; Estrin, A. D.; Murgida, D.; Kalyanaraman, B.; Marti, A. M.; Radi, R., *Arch. Biochem. Biophys.*, **2012***, 525*, 82-91.

33. Surdhar, S. P.; Armstrong, A. D., *J. Phys. Chem.*, **1987**, *91*, 6532-6537.

34. Gaston, B. *Biochim. Biophys. Acta*, **1999**, *1411*, 323-333.

35. Prutz, A. W.; Monig, H.; Butler, J.; and Land, J., *Arch. Biochem. Biophys.*, **1985**, *243*, 125-134.

36. Hodges, G. R.; Marwaha, J.; Paul, T.; Ingold, K. U., *Chem. Res. Toxicol*., **2000**, *13*, 1287-1293.

37. Zielonka, J., Sikora, A., Joseph, J., and Kalyanaraman, B. *J. Biol. Chem.*, **2010**, *285*, 14210-14216.

Chapter 4. Studies on Reactions Under Sustained Fluxes of Peroxynitrite in the Wells of the Platform

4.1 Background

The post-translational modification of tyrosine to 3-nitrotyrosine (3-NT) has long been accepted both as a hallmark indicator of inflammation and a footprint of the reactive nitrogen species peroxynitrite (PN).[1-3] Initial skepticism regarding the physiological relevance of this modification arose from low and contradictory yields of 3-NT defined by the mode of PN synthesis employed by various groups as discussed previously. However, the critical link between PN-mediated nitration of tyrosine and diseased states has now been demonstrated by the identification of this modification at critical tyrosine residues within proteins and enzymes collected from *in vitro* and *in vivo* sources.[4-6] Although identification of the post-translational modification in collected tissue samples and cellular assays has silenced skepticism regarding the physiological relevance of this PN-mediated process, biochemical and proteomic exploration of PN pathophysiology remains at its nascent stage due to technical difficulties encountered in sustained generation of PN in laboratory settings to provide significant levels of modified protein for further analytical investigations.[1] Given the results obtained in previous nitration studies where exposures of free tyrosine and model peptide **Y1** to PN within the wells of our second-generation PN platform (24-well plate) for 30 min yielded ~40 % nitration, we attempted to extend the time interval of PN exposure further to reach approach 100 % nitration of a desired tyrosine-containing peptide or protein.

Because it has been strongly correlated that nitration of a tyrosine residues of a protein or peptide can impose structural perturbations that ultimately alter the

function of the biostructure, we synthesized model β-hairpin peptide **YTV** in hopes of performing 2D-NMR experiments confirming such effects. However initial attempts to maximize the nitration of **YTV** yielded unexpected results, spurring the questions *what happens after nitration?* Exploration into this facet of chemistry requires conditions of sustained PN exposure mimetic of chronic inflammations.

4.1.1 Tyrosine Nitration: Physicochemical Changes

Tyrosine is an amphoteric amino acid that constitutes 3-4 mol % of proteins, capable of undergoing H-bonding and nonpolar interactions. While the vast majority of tyrosine residues are solvent exposed (~15% of tyrosine are 95% buried), nitration of tyrosine has been observed to be a highly selective process, suggesting that some tyrosine residues are more susceptible to nitration than others. In fact, it has been noted that (1) the presence of an acidic residue such as glutamic or aspartic acid, (2) small number of cysteine and methionine residues, and (3) the presence of a proline or glycine in the local vicinity of a tyrosine residue can direct nitration.

Physicochemical features of tyrosine include a pK_a of 10.07 (depending upon the solvent system) and a tyrosine/tyrosyl (Tyr/TyrO$^{\bullet}$) redox potential (E°′) of 0.94 V,[1] with the latter parameter playing a crucial role in electron transfer when the tyrosine is located at the active site of the enzymes. Although several amino acids have been implicated in high-potential redox catalysis, Warren *et. al.* have noted that tyrosine and tryptophan remain the main players in such process, and that the redox chemistry of tyrosine is *inherently proton-coupled* (Figure 4.1).[7] The proton (H^+)/electron (e^-) transfer are collectively called *proton-coupled electron transfer* (PCET). Further, it

has been stated that the pH dependent oxidation and reduction of tyrosine occurs with a loss and gain of H^+ and e^- in *all* but extreme cases. PCET of tyrosine and has been supported through the use of small molecule models, such as tyrosine-tethered Ru(II)-tris(diimine) photosensitizer. In many of these studies the electron transfer process requires, or is sharply accelerated with, the addition of a base (a requirement that may parallel the observed selectivity in the nitration of tyrosine residues in the vicinity of acidic amino acid residues).[7-9]

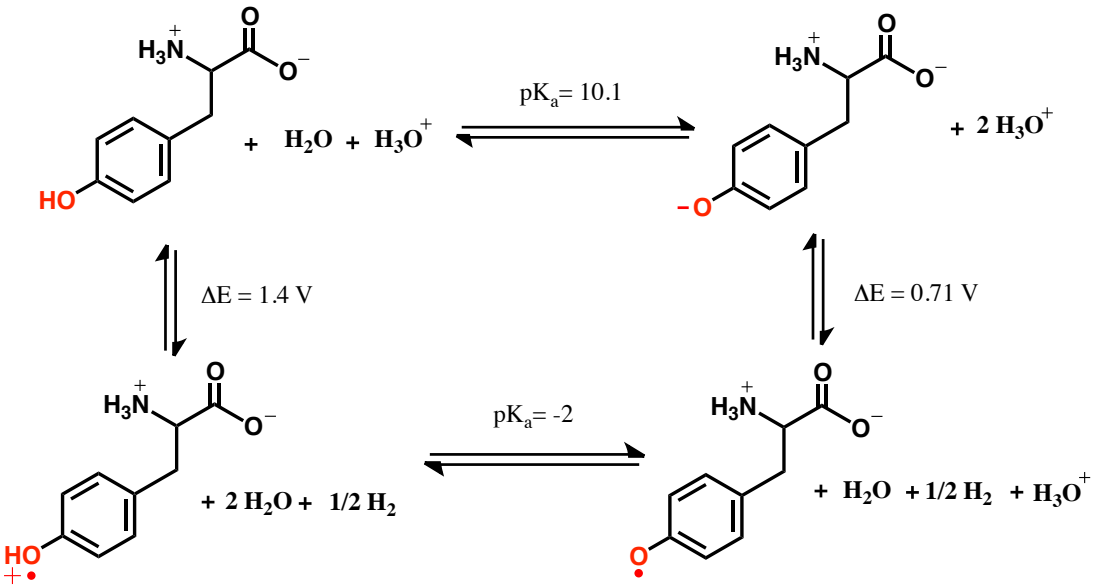

Figure 4.1. Thermodynamic cycle for tyrosine in aqueous media.[7]

Addition of a nitro group (–NO_2) to the phenolic ring significantly changes the physicochemical properties of the amino acid (pK_a = 7.2-7.4, 3-NT/3-NT$^\bullet$ $E°'$= 1.1-1.2 V).[1] Such changes are expected to lead to a diverse array of chemistry (distinct from that of tyrosine) that has hardly been explored in the realm of PN. While nitration of tyrosine represents a relatively unique modification among established

biological transformations, the chemistry of nitrated phenyl rings is rich and established. In general addition of NO_2 to a phenyl ring strongly activates the ring towards nuleophilic aromatic substitution (S_NAr).[10] In fact, the addition of NO_2 to phenyl moieties has been seen to strongly direct various chemical reactions such as Ullmann reactions (De-halogen-coupling) that can be utilized to form symmetric and asymmetric biaryls.[11,12] Interestingly, while the diverse chemistry of nitrophenyls and nitrophenols that have been meticulously studied over the course of the last century the chemistry of 3-NT remains unexplored.

4.1.2 Tyrosine Nitration: Aggregative Proteins

In the late 1960's a series of reports were published describing an aggregation phenomena of proteins following exposure to nitrating agent tetranitromethane (TNM).[13,14] Boesel and Carpenter performed a time-dependent study showing that aggregation likely proceeded through a dimerization event between tyrosine residues and performed equivalent experiments with glycine-L-tyrosine to corroborate this hypothesis. Under acidic conditions nitration of glycine-L-tyrosine upon exposure of TNM was observed as the predominant and primary product, while the same experimental parameters under alkaline conditions gave rise to a numerous unknown products. The authors proposed that cross-linkage between tyrosine residues because it was found that the number of unreacted tyrosine residues reached almost zero after 100 minutes of exposure to TNM, while the percentage of glycine-L-3-nitrotyrosine was only 24 %. So they posed the question *what happened to tyrosine*? Reference was made to work by Walter and coworkers that had reported the formation of

polymeric products and Pummerer's ketone after exposing *p*-cresol to TNM through a $^{\bullet}NO_2$ oxidation process to generate a phenoxy radical at the p-cresol O.[15] The generalized nitration mechanism of phenols by TNM is shown in Figure 4.2, where the proposed crosslinkage pathway is initiated by the formation of a phenoxyl radical ($Ph\text{-}O^{\bullet}$) and nitrite (NO_2^-) that first proceeds through a formed charge transfer

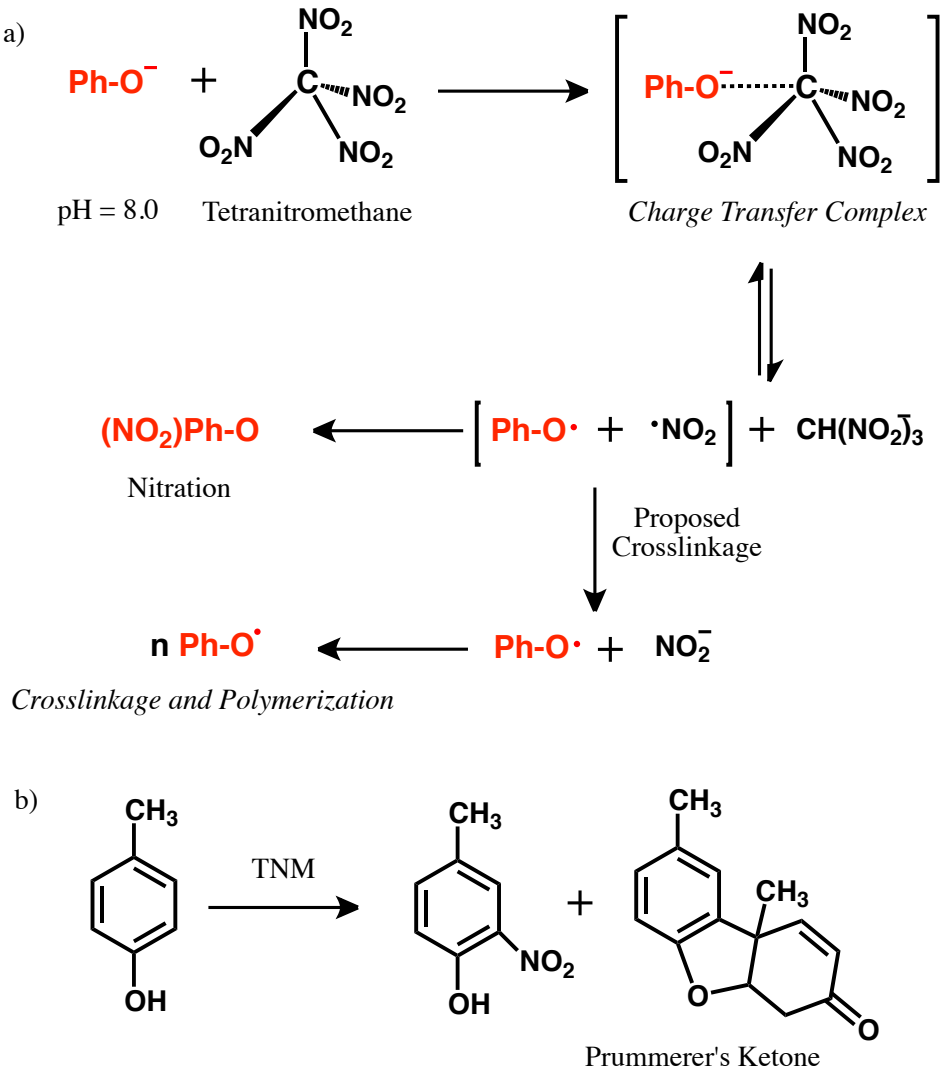

Figure 4.2. (a) Proposed TNM-mediated nitration mechanism and (b) products observed upon exposure of *p*-cresol to TNM.

complex between TNM and a phenolate molecule ($Ph\text{-}O^-$). Incubation of bovine insulin, collagen, and rabbit γ-globulin with TNM resulted in the formation of dimer, trimmers, and oligomers that showed significant stability against denaturation by heat or urea treatment.[13,14]

Review of the literature contributed to further perpetuated interest in exploring this post-nitration chemistry given the results reported by Lee and coworkers that showed the formation of an ultra-stable α-synuclein aggregate formed *only* upon exposure to PN.[17,18] Exposure of α-synuclein to alternative nitrating (known to proceed through electrophilic aromatic substitution, NO_2^+) and oxidizing sources resulted in the formation of significantly weaker aggregates, easily denatured with heat or urea treatment.[8] *Based on the series of work discussed we chose to explore the chemistry of 3-NT to probe the possibility that the dimerization events observed in the aggregative proteins highlighted above (insulin, collagen, and rabbit γ-globulin) could occur between nitrated tyrosine residues*.

4.2 Extended Exposure of a Model Peptide to PN

With initial intentions of maximizing product yields for potential proteomic investigations we treated model peptide KK**Y**TVSINGKKITVSI (YTV, 0.25 mM) with β-hairpin-like secondary structure (R-groups of the amino acid residues exposed outward)[18] to PN within the wells of the platform (24-well plate, pH 7.4 phosphate buffer, 25 mM $NaHCO_3$, affording ~4μM PN min^{-1})[19] for 20 min intervals. At the end of each interval we analyzed the well content by electronic absorption spectroscopy to

monitor the growth of the absorbance band with λ_{max} (maximum absorbance) at 370 nm indicative of tyrosine nitration.[20] Over the course of the first two time intervals (40 total min of PN exposure), the 370 nm absorption band increased as expected. However, at the end of the third interval of exposure (60 total min of PN exposure) dramatic spectral changes were observed with a sharp diminishment and slight blue shift in the λ_{max}, as highlighted in Figure 4.3. To explore the origin of these changes in the absorbance spectrum, the well content was processed by high-pressure liquid chromatography (HPLC). Following separation, the peaks were collected and further analyzed by MS. The analytical results indicated dimerization between two nitrated YTV units, as evidenced by the observed $[M+H]^+$ peak at *m/z* 3649 (Figure 4.3). Secondary analysis of this dimeric product by fluorescence spectroscopy revealed a *biphenyl-type* emission profile insinuating coupling between aromatic residues (Figure 4.3).[21] Given the primary sequence of the model peptide, the tyrosine residue stands out as the likely site of dimerization.

These findings indicate that the tyrosine residue within the YTV peptide is nitrated within the first 40 min of exposure to PN within the wells of the platform and the concentration of tyrosine-nitrated YTV (YTV-NO_2) builds in the system in the presence of the sustained PN flux. Further reaction of PN with YTV-NO_2 presumably promotes dimerization of 3-NT residues between YTV-NO_2 peptides. The HPLC chromatograph (not shown) observed of the crude well content showed a number of peaks directly following the parent YTV peak, similar to that observed in Bosele and Carpenters when glycine-L-tyrosine was exposed to TNM for 100 min, likely

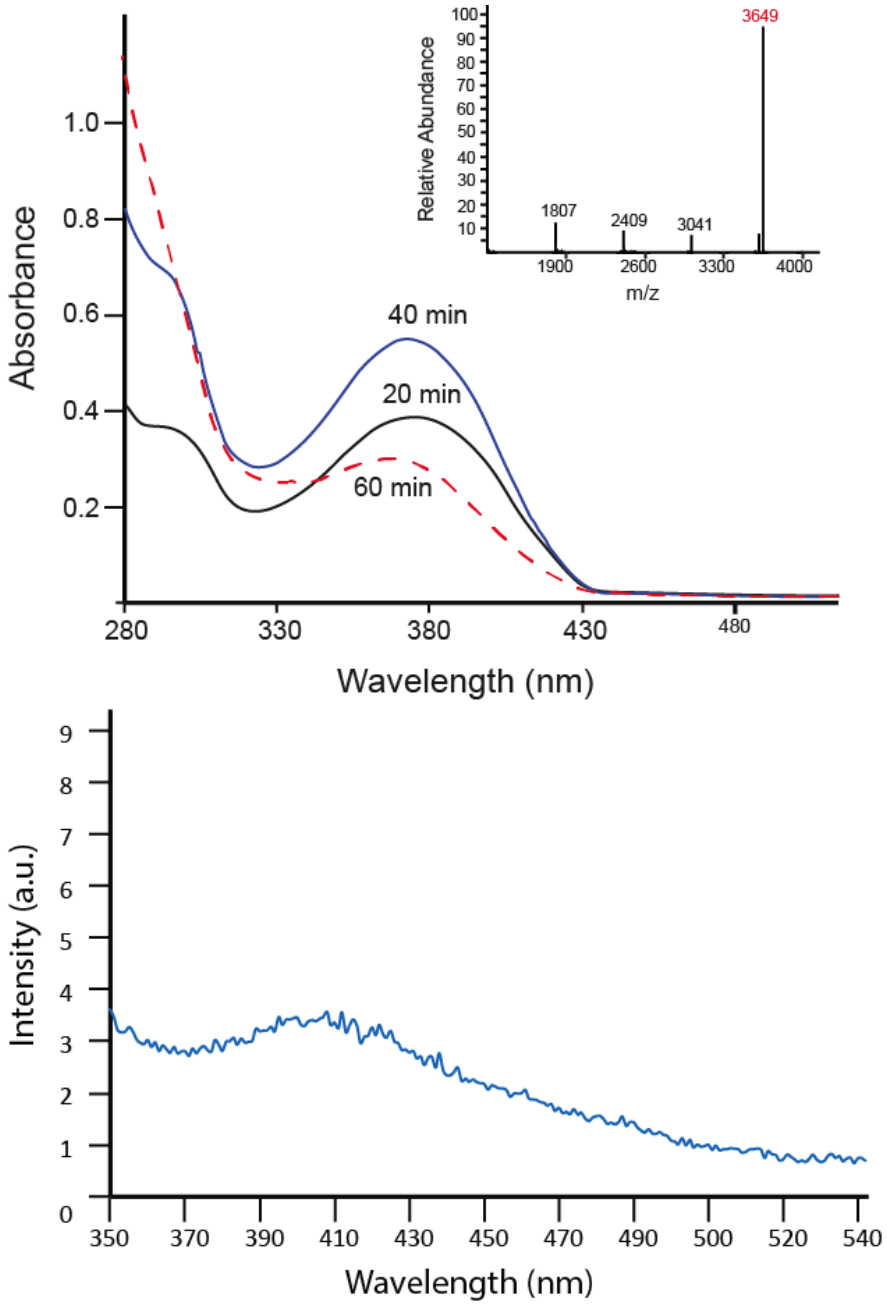

Figure 4.3. (**Top panel**) Electronic absorbance spectrum of the well content in which YTV peptide was exposed to PN for 20 min (solid black line), 40 min (solid blue line), and 60 min (dotted red line). Mass spectrum (Inset, deconvoluted) and fluorescence spectrum (bottom panel, excitation wavelength 270 nm) of the product peak collected from the HPLC separation.

indicative of alternative oxidation and degradation products. Mass spectral analyses were performed on all peaks, but only one of the peaks afforded the mass value representative of 3-nitrotyrosine linkage between two peptide monomers.

4.3 PN-Mediated Dimerization of 3-NT Monomers

In attempts to elucidate this potential linkage we proceeded to study the proposed active unit, 3-nitrotyrsoine (3-NT. The concentration of 3-NT was selected to match the maximum level of tyrosine nitration (~160μM) observed with the YTV peptide within the wells of the platform at the end of 40 min (as discussed above). The intent was to effectively emulate very similar well conditions to minimize secondary reactions. In all studies initial baseline spectra of standard 3-NT solutions were collected prior to PN exposure and compared to absorption spectra of the final well content to monitor spectral changes arising from PN reaction. When 3-NT was exposed to PN for 30 min under the same well conditions as in the previous YTV study, very similar absorptions profiles were observed with a blue shift of the λ_{max} from 370 to 350 nm, paired with a significant diminution in peak intensity. As the solution of 3-NT was exposed to PN in the wells of the platform, the initial vibrant yellow color gradually diminished to a pale yellow hue.

To separate the products formed in the wells of the platform we employed an HPLC equipped with a multi-channel diode array (DAD) detector. Analysis of the well content showed the formation of a single predominant species (Figure 4.4) that featured an absorbance profile distinct from 3-NT. This product peak with retention

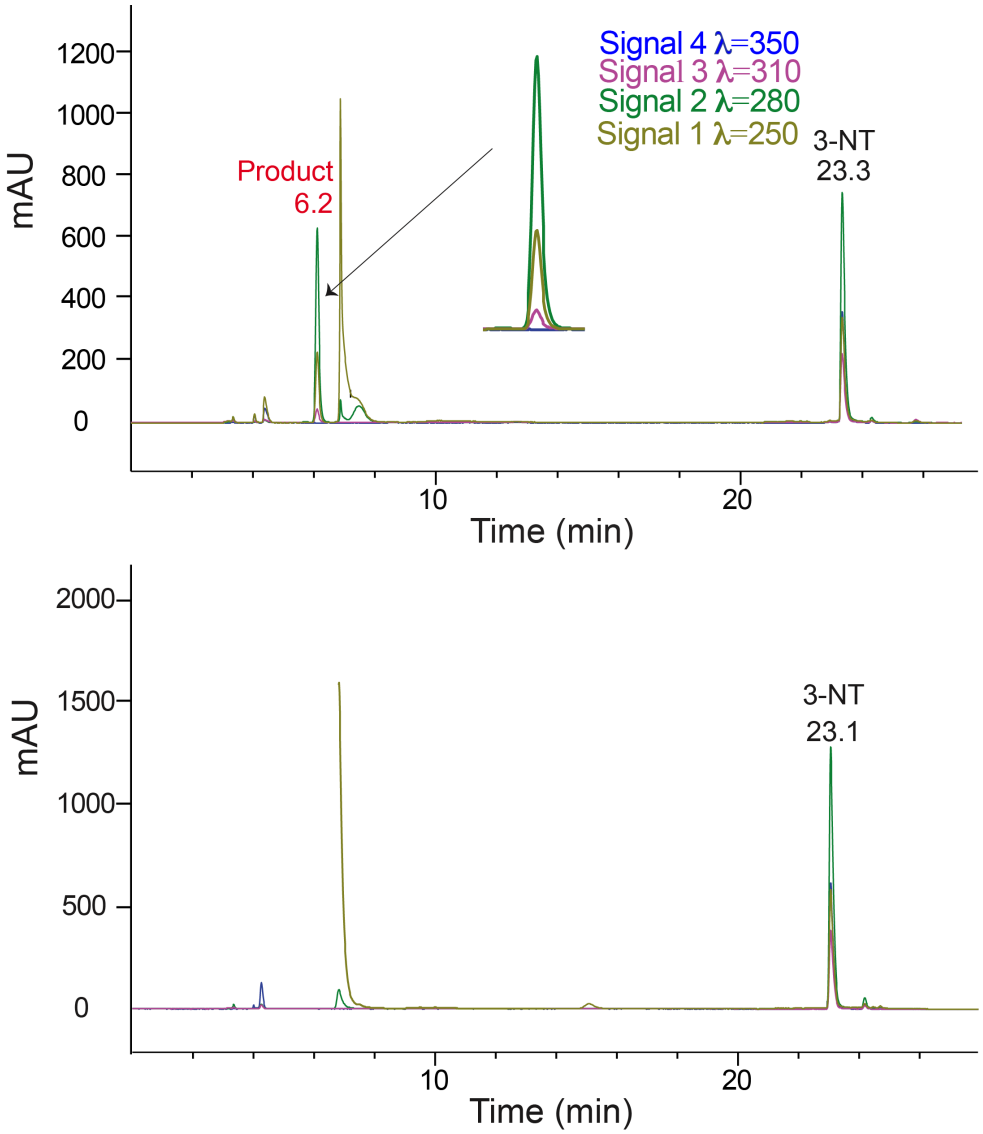

Figure 4.4. Chromatographic analysis of di-3-$NT_{C\text{-}O}$ formation. (Top) HPLC chromatogram of the analyte collected from a PN-generating well following exposure of 3-NT to PN for 30 min. The representative signals observed at 250, 280, 310, and 350 nm are shown highlighted in gold, green, purple, and blue, respectively, with the signal profile of the 3-NT dimer peak being highlighted in the inset. (Bottom) Corresponding HPLC chromatogram collected from control study where 3-NT was exposed to NO only for 30 min under the same conditions.

time of 6.12 min was detectable at 280, 250, and 310 nm but silent at 350 nm (Figure 4.4, inset), while 3-NT showed signals over all four wavelengths. Further, in control studies where 3-NT was exposed only to NO this product peak was absent.

Collection of the product peak allowed for further detailed mass spectral analysis. Tandem mass spectral analysis (MS/MS) of the sample on a LTQ mass spectrometer (electron spray ionization, positive ion mode, CID) uncovered a peak at *m/z* 451 indicative of a 3-NT dimer (di-3-NT). Fragmentation of this peak required three times standard collision energy (60 eV) to yield predominant fragmentation ions *m/z* 435, 390, 336, 226, and 210, with the later peaks corresponding to dissociation of the dimer to yield monomer 3-NT (*m/*z = 227, Figure 4.X). The characteristic mass spectral fingerprint of standard 3-NT features a mass transition of 227 → 181, with *m/z* 181 representing the most intense peak in the mass spectrum. Further, the relative intensity of the parent ion (*m/z* = 227) is typically weak because it rapidly looses a nitro group upon ionization to yield tyrosine and only sparingly decomposes to yield fragmentation product *m/*z 210 that corresponds to a loss of the phenolic hydroxide from the nitrated tyrosine amino acid.[24] However, the relative abundance intensity profile of the reaction product exhibited a predominant *m/*z 210 peak upon fragmentation of the *m/z* 451 peak (Figure 4.X). The remaining fragmentation peaks *m/z* 435, 417, 390, and 336 correspond to consecutive -H_2O and -HCO_2 losses from the parent dimer, and the rearrangement tropylium product (*m/z* = 336) observed previously in the mass spectra of compounds with 3,O′-dityrosine moiety.[22]

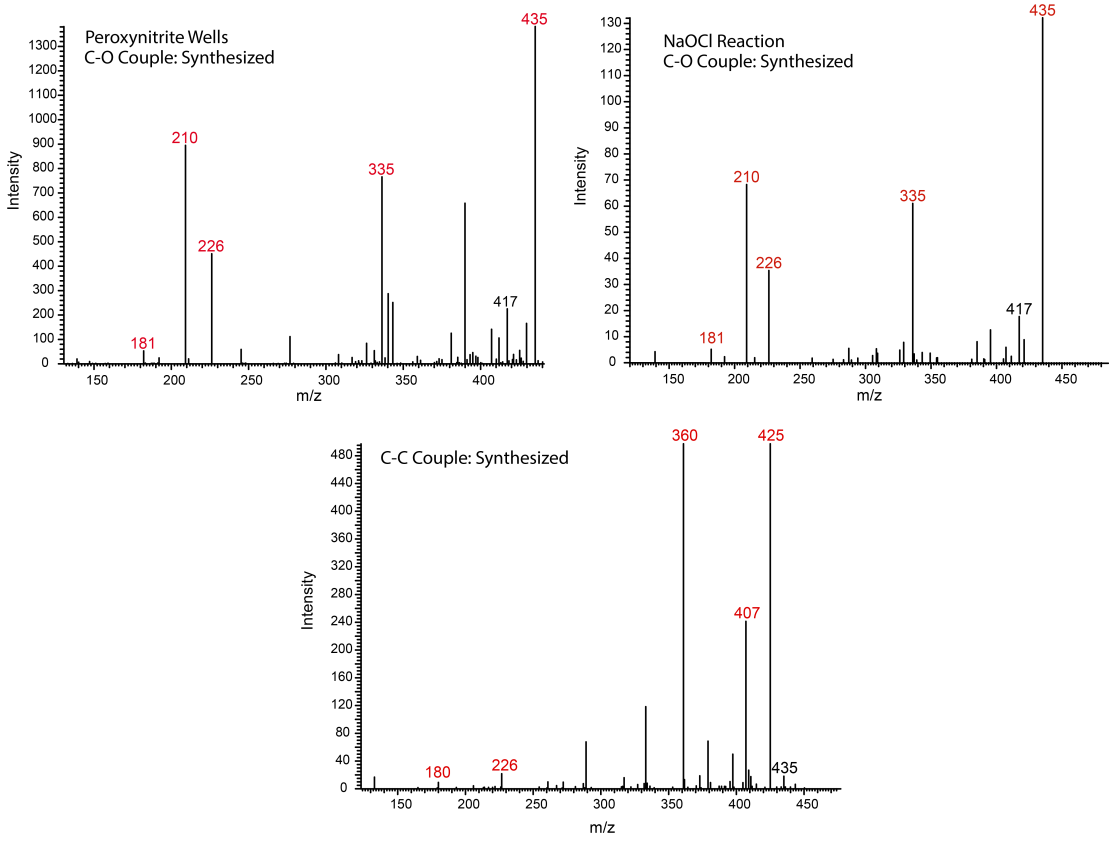

Figure 4.5 Comparative mass spectral analysis of di-3NT$_{C\text{-}O}$ and di-3NT$_{C\text{-}C}$. Mass spectra of (Top left) di-3NT$_{C\text{-}O}$ formed upon exposure of 3-NT to PN within the wells of the PN-generating platform, (Top right) di-3NT$_{C\text{-}O}$ formed upon exposure of 3-NT to NaOCl, and (Bottom center) synthesized di-3NT$_{C\text{-}C}$ with fragmentation ions *m/z* 425, 407, and 361 corresponding to loss of a carbon monoxide (-CO), nitro group (-NO_2), and sequential nitro group loss (2 (-NO_2)), respectively.
Peaks discussed in the text are highlighted in red.

Additionally, fluorescence analysis of the reaction product revealed an excitation band at 268 nm and a broad emission band at 420 nm with a shoulder at 456 nm (Figure 4.6). These features suggested dimerization connecting the phenyl moieties of the 3-NT units since standard 3-NT solutions lack fluorescence emission across all excitation wavelengths. The asymmetric profile of the emission band however differs noticeably from the peak profile of *o,o'*-dityrosine centered at 410 nm.[21] *Taken together, the spectroscopic results indicate dimerization of the 3-NT monomers through a C-O linker (di-3-NT$_{C-O}$) following exposure of 3-NT to PN in the wells of the platform.*

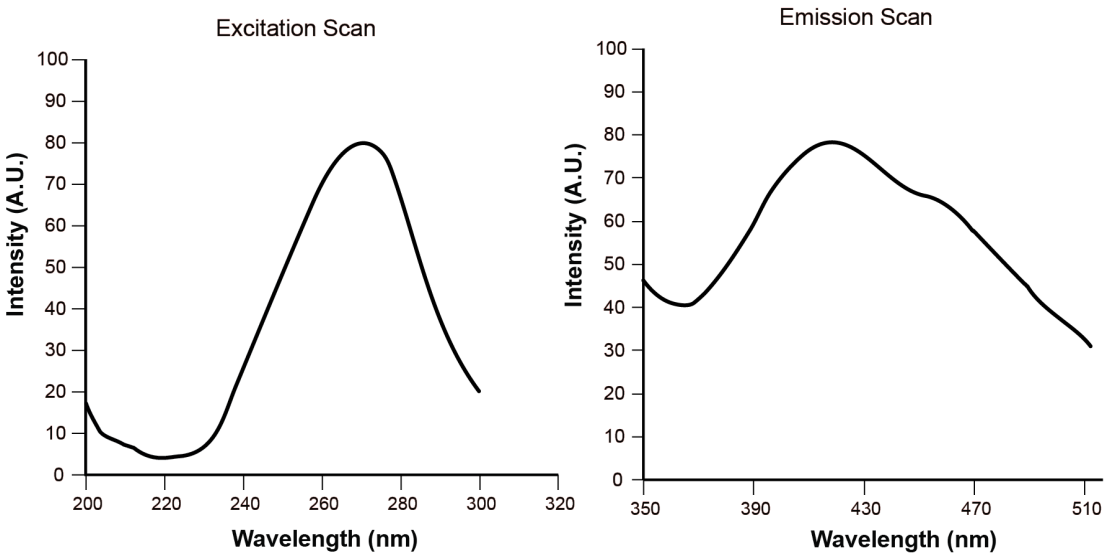

Figure 4.6. Fluorescence spectrum of di-3NT$_{C-O}$ (excitation wavelength 268 nm).

4.4 Uncovering the Coupling Modality of 3-NT Dimers by Mass Spectrometry

To distinguish the C-O coupling from C-C coupling on the basis of mass spectral fragmentation pattern and fluorescence emission profile, we synthesized the analogous C-C coupled isomer of di-3-NT (di-3-NT_{C-C}). Successful synthesis of di-3-NT_{c-c} was achieved in an *Ullman type* reaction which employs a cuprous catalyst and an inorganic base to couple an activated aryl halide with a nucleophile.[23,24] This nucleophilic aromatic substitution reaction afforded di-3-NT_{c-c} upon reaction of 3-NT (nucleophile) with 3-bromo-5-nitrotyrosine (the aryl halide) in the presence of a cuprous catalyst (Tetrakis(acetonitrile)copper(I) tetrafluoroborate, $[Cu(MeCN)_4]BF_4$) and Cs_2CO_3 in dimethyl formamide (DMF) under aerobic conditions. The resulting pale yellow powder was collected and analyzed by mass spectrometry, displaying a parent dimer peak at *m/z* 451 $(M+H)^+$.

Fragmentation of *m/z* 451 under equivalent collision conditions produced a fragmentation pattern distinct from that of di-3-NT_{C-O} (Figure 4.X), with predominant peaks at *m/z* 425, 407, and 360 that correspond to loss of a carbon monoxide (-CO), a nitro group ($-NO_2$), and sequential nitro group loss (2 ($-NO_2$)), respectively. Additional secondary *m/z* 226 and 181 peaks, corresponding to monomeric 3-NT, were also observed but in comparatively lower abundance. Further, the fluorescence profile of di-3-NT_{C-C} featured a symmetric emission band at 470 nm (Figure 4.7) compared to that of di-3-NT_{C-O}. Interestingly, basification of the solution results in a bathochromic shift in the emission band from 470 nm to 515 nm. Similar shifts have been reported for dimer molecule *o,o′*-dityrosine.

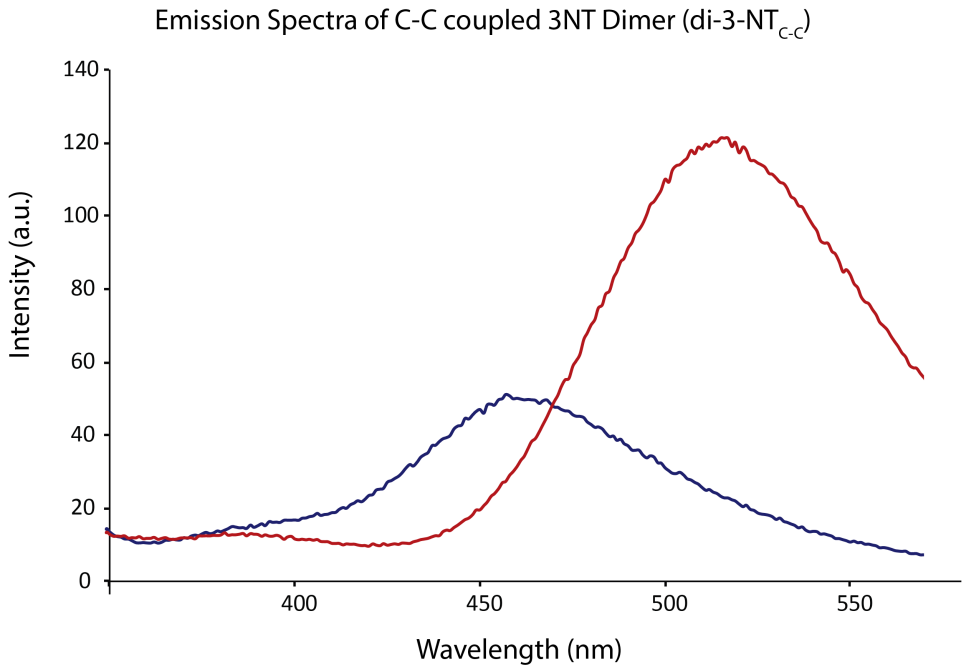

Figure 4.7. Fluorescence spectrum of di-3NT$_{C-C}$ (excitation wavelength 310 nm), at pH 7.4 (blue) and pH 10 (red).

Taken together, these data readily differentiate the products derived from 3-NT via C-C and C-O coupling (affording di-3-NT$_{C-C}$ and di-3-NT$_{C-O}$ respectively). In particular, the fragmentation pattern yielded following fragmentation of the parent dimer *m/z* 451 peaks of these isomers are dramatically different (Figure 4.5). The greatest difference is apparent in the range of *m/z* 150-250 where peaks corresponding to monomer 3-NT (*m/z* = 226) and its fragmentation ions are featured. Fragmentation of the parent peak of di-3-NT$_{C-O}$ (*m/z* = 451) produced a predominant peak at *m/z* 210 and secondary peaks at *m/z* 226 and 181, while the same parent peak of di-3-NT$_{C-C}$ afforded significantly less abundant decomposition products displaying weak peaks at *m/z* 226 and 180 (and no *m/z* 210 peak was observed). These decomposition profiles

corroborate the presumed C-O coupling of 3-NT upon exposure to PN (Figure 4.8). As expected, cleavage at the ether linkage of di-3-NT_{C-O} produced asymmetric products represented by predominant *m/z* 210 and 226 peaks; while cleavage along the symmetric C-C linkage of di-3-NT_{C-C} on the other hand resulted in *m/z* 226 and 180 peaks corresponding to decomposition of the dimer to monomeric 3-NT only.

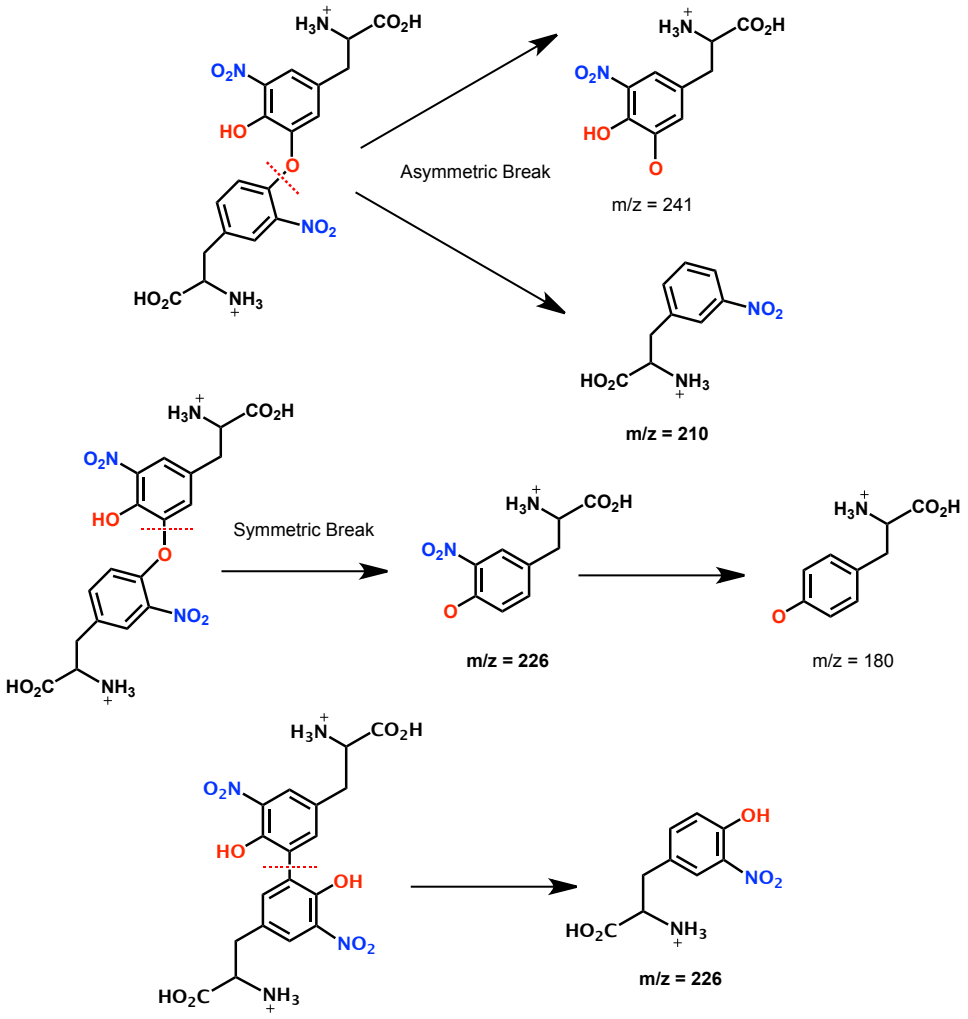

Figure 4.8. Proposed fragmentation profile of di-3-NT_{C-O}, highlighting the two possible modes of fragmentation along the C-O linkage (symmetric and asymmetric).

4.5 Probing the Mechanism of 3-NT Dimerization

Results of the comparative mass spectral studies of the di-3-NT_{C-O} and synthetic analogue di-3-NT_{C-C} confirmed C-O coupling between 3-NT monomers in the presence of PN. In attempts to unravel the possible mechanism of 3-NT dimerization mediated by PN we employed sodium hypochlorite (NaOCl, E° = 0.89 V)[23] as an alternative oxidant, produced by myeloperoxidase (MPO) during acute human inflammatory conditions.[23] In this experiment, 160 μM of 3-NT was exposed to 10 μL of NaOCl for 30 min and the reaction mixture was collected and processed by HPLC (Retention time = 17.277 minutes, Figure 4.9). The resulting chromatogram featured a peak with an absorption profile identical to that observed in the previous PN studies, with λ_{max} at 280, 250, and 310 nm.

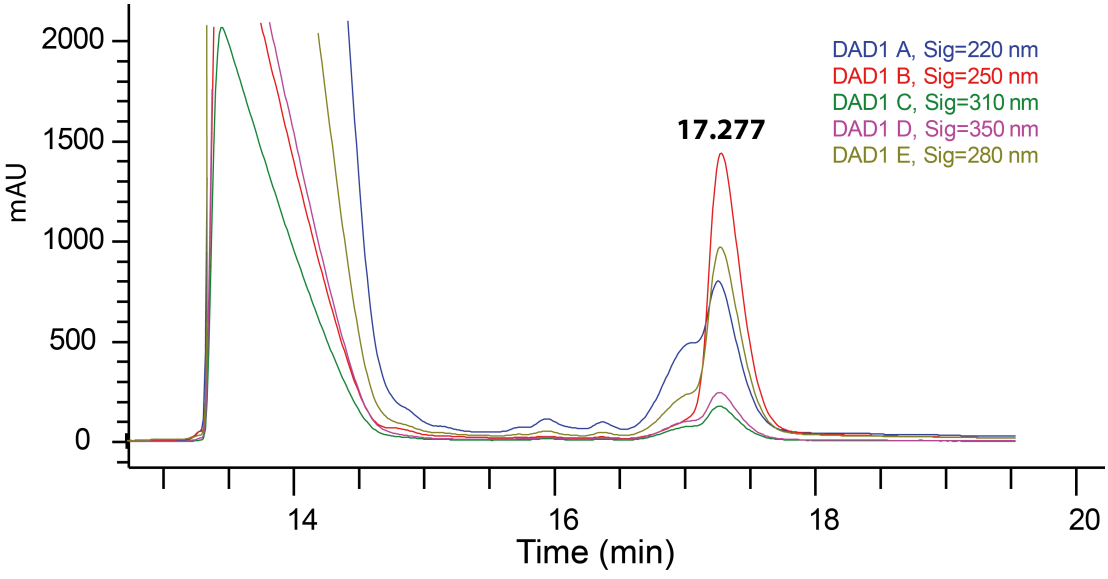

Figure 4.9. HPLC chromatogram collected following exposure of 3-NT to NaOCl for 30 min. The peak denoted at 17.277 min was collected and further analyzed my mass spectrometry. Absorbance wavelengths denoted by color.

Mass spectral analysis of this product also produced identical fragmentation pattern (Figure 4.5), where the parent dimer *m/z* 451 peak afforded *m/z* 226, 210, and 181 peaks (60 eV collision energy) indicating formation of di-3-$NT_{C\text{-}O}$. Additional studies were carried out as control experiments where L-tyrosine was exposed to NaOCl that yielded a product with mass observed at 363 m/z and fluorescence emission band at 310 nm upon excitation at 280 nm. These results suggest *o,o´*-dityrosine formation. The oxidation-mediated pathways of 3-NT dimerization became more apparent when doubling of the concentration of 3-NT in the oxidation reaction resulted in a significant decline in the formation of di-3-$NT_{C\text{-}O}$, as observed by a significant decrease in intensity of the corresponding HPLC peak. Equivalent experimental conditions in the PN-generating system resulted in very similar results, where the corresponding di-3-$NT_{C\text{-}O}$ HPLC peak was barely above the detection limit of the instrument. The sharp diminution of di-3-$NT_{C\text{-}O}$ formation with increased concentration of 3-NT clearly suggests that dimerization of the 3-NT monomer units is optimal under *excess oxidant conditions*.

Because carbon dioxide (CO_2, physiological concentration ≥ 1.3 mM) effectively sequesters PN to generate stronger oxidants namely, carbonate radical ($CO_3^{\bullet-}$, E° = 1.759V) and nitrogen dioxide ($^{\bullet}NO_2$, E° = 1.04 V),[24] we also probed the dependence of di-3-$NT_{C\text{-}O}$ formation on the concentration of PN as oxidant by decreasing the concentration of CO_2 by one-half (14 mM $NaHCO_3$) within the wells of the PN-generating platform. Once again, the intensity of the HPLC peak corresponding to di-3-$NT_{C\text{-}O}$ was significantly reduced.

Compilation of these findings supports PN-mediated oxidation of 3-NT monomers to yield di-3-$NT_{C\text{-}O}$. Coupling between the nitrated tyrosine units most likely proceeds through the oxidation of the phenol moiety by $^{\bullet}NO_2$ and $CO_3^{\bullet-}$ (both strong oxidants). Formation of the resulting phenoxy radical and radical dimerization events are both favored with highly substituted phenols, most commonly when a substituent is present *ortho* to the hydroxyl group.[25] Radical coupling reactions as shown in Figure 4.10 eventually lead to the formation of the C-O coupled product di-3-$NT_{C\text{-}O}$.

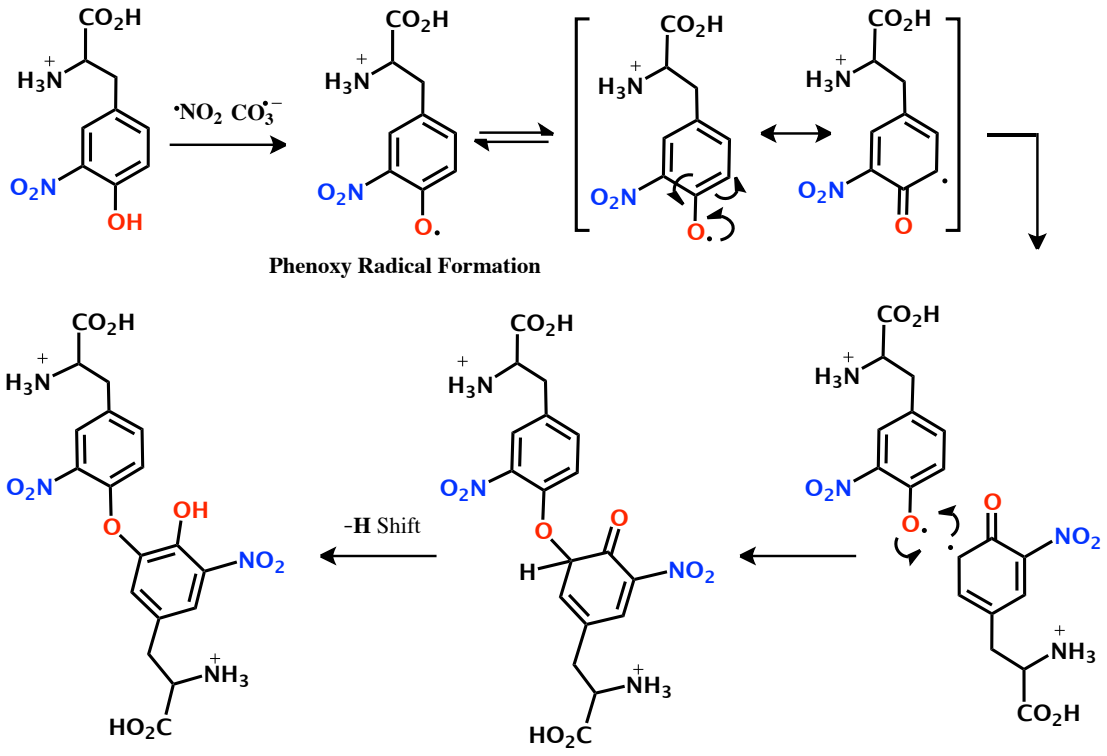

Figure 4.10. Proposed mechanism of C-O coupling between 3-NT residues

4.6 Establishing PN-mediated Dimerization in Model Tripeptide

To explore the possibility of PN-mediated dimerization of 3-NT units within biomolecules we synthesized a model tripeptide K(3-NT)V that contained a single 3-NT residue. This tripeptide was designed with the intention of creating a model peptide system that could be processed by tandem mass spectrometry to confirm the occurrence of the di-3-NT_{C-O} moiety within the resulting peptide dimer following exposure to PN. As described above, 160 μM of K(3-NT)V was exposed to PN within the wells of the PN-generating platform (pH 7.4, 25 mM $NaHCO_3$) for 30 min. The well content was then processed by HPLC and the product peaks were further analyzed by mass spectrometry to verify dimerization of the K(3-NT)V peptide.

The peak with retention time of 18.2 min exhibited a parent dimer $[M+2H]^+$ peak at *m/z* 906 confirming di-K(3-NT)V formation. Further fragmentation of this parent ion required 80 eV collision energy and afforded peaks *m/z* 452, 435 and 336. Because the molecular weights of K(3-NT)V monomer and di-3-NT_{C-O} unit are 453 Da and 452 Da, respectively, we first fragmented the parent *m/z* 451 peak to confirm that it originated from K(3-NT)V arising from dissociation of the dimer. On the other hand, fragmentation of the *m/z* 435 peak afforded a decomposition pattern (with predominant peaks observed at *m/z* 336, 210, and 226, Figure 4.11) identical to that obtained in case of di-3-NT_{C-O} (Figure 4.5). Collectively these results demonstrate that the PN-induced dimerization of the K(3-NT)V peptide does occur through C-O coupling analogous to that in the formation of di-3-NT_{C-O}.

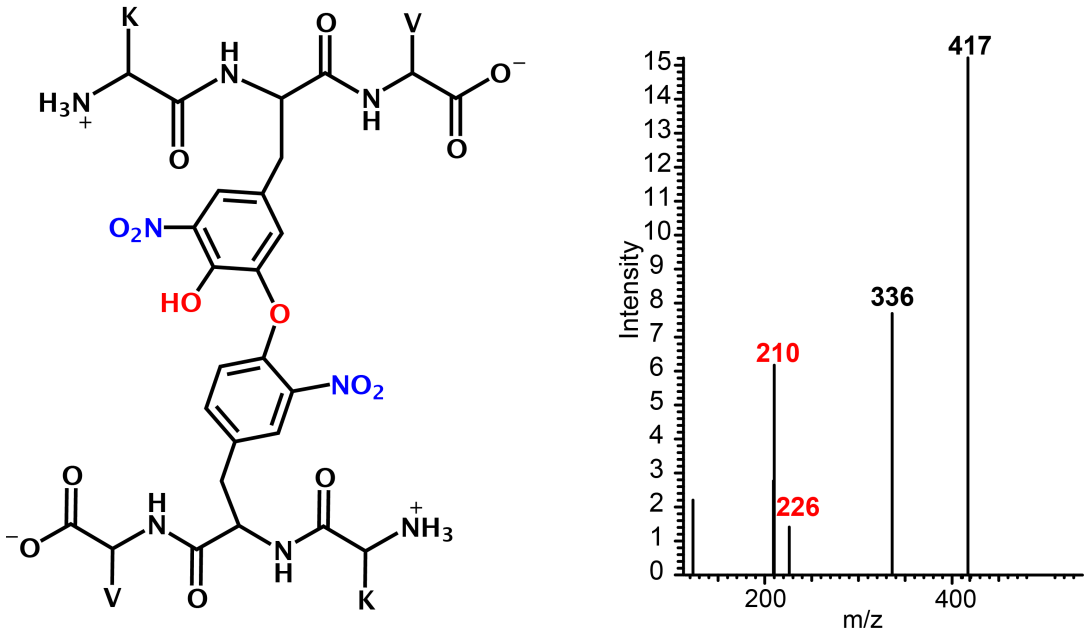

Figure 4.11. Mass spectral analysis of di-K(3-NT)V. (Left) Simplified representation of di-K(3-NT)V highlighting the ether linkage between K(3-NT)V monomer units. (Right) Mass spectrum obtained following consecutive MS/MS processing of parent dimer (906 m/z) fragmentation that yielded a mass spectral profile indicative of C-O coupling between the peptide monomers.

4.7 Conclusion

It is important to note that in case of the YTV peptide, the dimerization phenomena proceeds only after an optimal concentration of the nitrated YTV derivative is reached within the wells of the PN-generating platform. This observation clearly indicates that the PN-mediated C-O coupling between peptides with nitrated tyrosine residues *could only be observed under prolonged exposure of the reaction mixture to PN*, a requirement not easily attained with the use of conventional PN sources. PN chemistry within the wells progressed from predominantly nitrative to

oxidative as the concentration of nitrated YTV rapidly built in the well content (a schematic of which is shown in Figure 4.12). It is evident that nitration of tyrosine leads to significant alteration of its physicochemical parameters that in turn changes the reactivity of the phenyl ring toward oxidative PN chemistry.

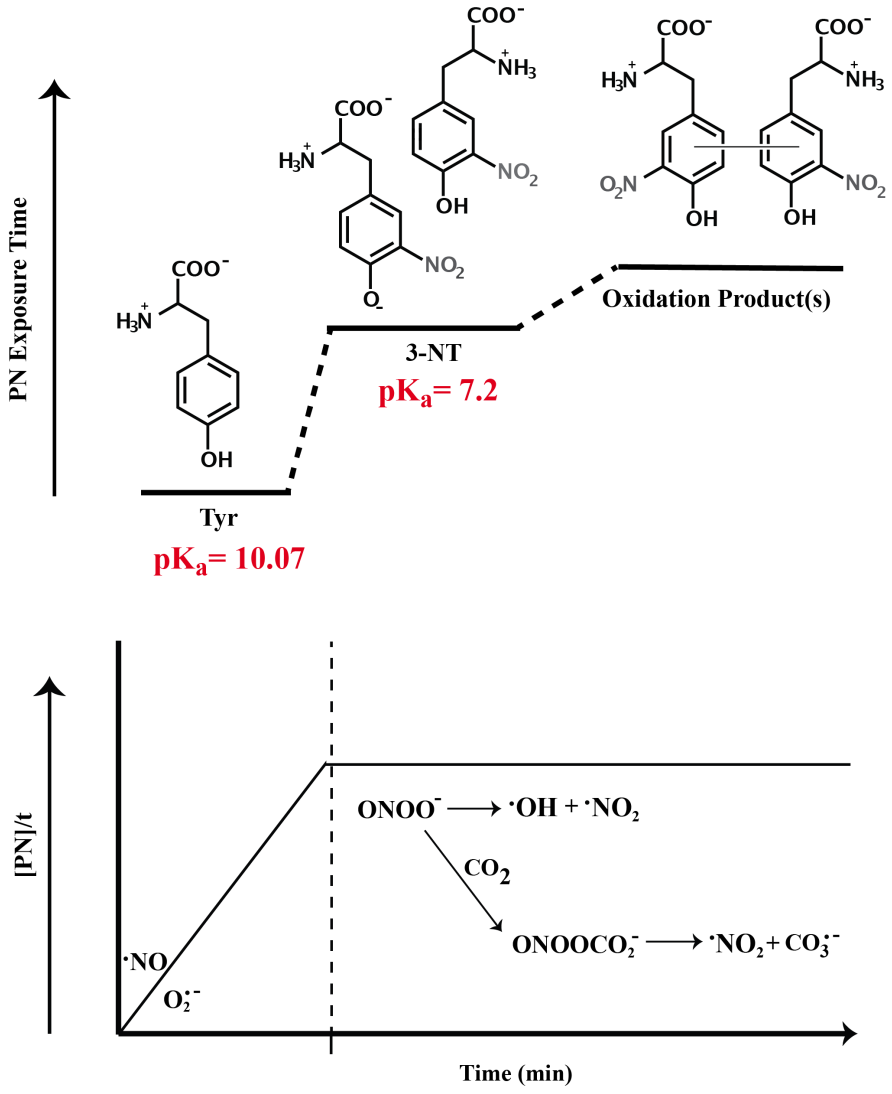

Figure 4.12. Schematic representation of the species within the PN-generating wells as a function of time.

The broader impact of this work can be translated back to the observed aggregation phenomena discussed previously, keeping in mind two critical features of proteins that may be susceptible to dimerization events between their nitrated derivatives. The first is realized after taking a closer look at the primary sequence of the proteins where ultra-stable aggregates formed upon exposure of PN. In all cases, there are distinct ratios of tyrosine to sulfur-containing amino acid residues. For example, work reported by Ischiropoulos and coworkers showed that α-synuclein formed stable aggregates that resisted thermal and chemical degradation after exposure to PN, while β-synuclein and RNAse did not. All three contain four tyrosine residues in the primary sequence, but display large variations in the ratios and relative spatial arrangement of tyrosine to methionine to cysteine residues. Additionally, α-synuclein contains the greatest number of acidic residues, a feature proposed to facilitate tyrosine nitration in proteins and peptides, with aspartic acid residues directly neighboring the three of the four tyrosine residues. Second, many of the proteins observed to aggregate are characteristically random coil with no long-term structure. This feature makes intermolecular tyrosine and 3-nitrotyrosine dimerization events increasingly probable compared to large structured enzyme and proteins where tyrosine residues can be buried in the structure of the biomolecule.

Interestingly to note is that many of the proteins discussed throughout are found in relatively high abundance at specific locations in the body. For example α-synuclein is typically concentrated at synaptic clefts and comprises 1% of all proteins found in the brain. Exposure of this protein to sustained and chronic levels of

inflammatory conditions presumably gives rise to pathological effects observed through the formation of aggregate Lewy bodies. Given this proteins susceptibility towards nitration and its perpetuated exposure to reactive oxygen and nitrogen species the dimerization events highlighted above could prove to be one of the dimerization variants that contribute to the formation of the ultra-stable aggregates frequently observed following its exposure to peroxynitrite.[16] *Taken together, the results and observations discussed emphasize the potential impact of the PN-generating platform that could afford, for the first time, a tool to study the chemistry of sustained and prolonged PN exposure.*

4.8 Methods

All chemicals used were analytical or ACS grade unless otherwise noted. Platform components xanthine oxidase, tetramethylorthosilicate, and hypoxanthine were purchased from Sigma-Aldrich. Catalase was procured from Spectrum Chemicals MFG Corp. HPLC grade solvents acetonitrile (ACN) and trifluoroacetic acid, and 3-nitrotyrosine (3-NT) were obtained from Sigma-Aldrich.

Synthesis of PN-Generating Platform. Peroxynitrite-generating platforms were constructed as described in our previous publication.[16,17] In short, individual $^{\bullet}$NO- and $O_2^{\bullet-}$-generating sol-gel pieces were synthesized through the encapsulation of $[Mn(PaPy_3)(NO)]ClO_4$ ($PaPy_3$= N,N′-bis(2-pyridylmethylamine)-N- ethyl-2-pyridine-2-carboxamide), xanthine oxidase (XO), and catalase (CAT) solutions into respective tetramethylorthosilicate matrices. Stock solutions of the corresponding reactive

species sol-gel mixtures were plated into individual 24-well plates and (600μL Mn(NO) and 800μL, XO/CAT sol-gel mixtures respectively) and allowed to solidify and dry in the dark for 1 week at 4°C. Activity of the final sol-gel pieces were analyzed at random prior to use with the aid of an NO electrode and electronic absorption spectroscopy, as described previously.[1,2] The individual sol-gel pieces were then combined in a single well of a 24 plate to afford the final peroxynitrite-generating system. Generation of $^{\bullet}NO$, $O_2^{\bullet-}$, and peroxynitrite was initiated with exposure of the plate to low power (10mW) broadband light and the addition of hypoxanthine (final concentration 250 μM unless otherwise noted).

Peptide Synthesis and Purification. The two peptides YTV and K(3-NT)V were synthesized using Fmoc synthesis on a Liberty 1 Peptide Synthesizer with Discover® microwave platform on a 0.1mmol scale, and monitored with PepDriver software. Peptides were assembled on a Rink-amide ChemMatrix® resin (Sigma-Aldrich). All amino acids were purchased through Aapptec. The deprotection of the Fmoc group was achieved using a 0.1M solution of hydroxybenzotriazole (HOBt) and 20% piperidine in dimetheyl formamide (DMF). 0.625M diisopropylcarbodiimide (DIC) and 1.25M HOBT in DMF were used in the coupling reactions, and all couplings were performed at 4 equivalents of Fmoc-amino acid. Each amino acid was double coupled.

A cleavage cocktail consisting of 10 mL of TFA, 0.5 mL each of 1,2-ethanedithiol (EDT) and liquefied phenol, and 1 mL of triisopropylsilane (TIPS), was added to

each vessel of dried resin and reacted for 2 h followed by filtration. The filtrate was added to 90 mL of cold, dry diethyl ether for precipitation. The precipitate was collected by centrifugation, and the ether was discarded. The pellet was dissolved in 20 mL of 1:1 H_2O/ACN (1% formic acid) and lyophilized. Peptides were purified by RP-HPLC on Vydac semi-preparative C18 columns. Fractions were collected and analyzed by ESI-MS on a Micromass ZMD mass spectrometer to confirm the correct molecular weight.

Exposure of YTV, 3-NT and K(3-NT)V to PN. In the wells of the platform, 250 μM YTV was exposed to peroxynitrite for 20 min time intervals (pH 7.4, 25 mM $NaHCO_3$) under continuous undulation. At each time point, the well content was removed and analyzed by electronic absorption spectroscopy. The analyte was then transferred back into the wells of the platform for further peroxynitrite exposure. In 3-NT and K(3-NT)V studies 160 μM of the respective substrates were exposed to peroxynitrite for 30 min within the wells of the platform, while all other conditions were maintained. At the end of all experiments the well contents were removed and processed by HPLC and mass spectrometry (Thermo Electrospray Ionization LTQ-Orbitrap Velos Pro, run in positive ion mode).

HPLC Analysis of YTV product, di-3NT, and di-K(3-NT)V. Analysis of well content was carried out using a Hewett Packard 1050 Series HPLC, equipped with a 4.6 mm x 250 mm C18 5U reverse-phase Econosphere Alltech column and diode array detector. Samples were manually injected into a Rheodyne 7225 injection loop

and eluted over 30 min with H_2O/ACN (both containing 0.1% Trifluoroacetic Acid) at a flow rate of 0.8 mL/min. The established solvent method developed as follows: 0-15 min isocratic 98:2, 15.01-20 gradient 70:30, 20.01-25 gradient 98:2, and 25.01-30 isocratic 98:2. Detection wavelengths included 220 nm, 280 nm, 310 nm and 350 nm with bandwidths of 4 nm. Chromatographic peaks were collected and lyophilized (VirTis bench top SLC lyophilizer) for fluorescence and mass spectral analysis.

Fluorescence Analysis. Lyophilized sample were dissolved in 2 mL of 50:50 H_2O:ACN (0.1% formic acid) solution and analyzed by fluorescence spectroscopy (Varian Cary Eclipse) with slit widths set to 10 nm. An initial excitation and emission scan was completed to define max emission and excitation bands.

Synthesis of 3-Bromo-5-Nitrotyrosine. A 50mL round bottom flask was charged with 100 mg of 3-bromotyrosine (385 mmol). To this solid, 2 mL of neat nitric acid was added dropwise. The white solid quickly dissolved in the rapidly stirred acid and yielded a deep orange-yellow solution. To this solution, 2 mL of diethyl ether was added when a fluffy pale yellow solid formed. The solid was collected and thoroughly washed with diethyl ether. The fluffy solid was then recrystallized from methanol yielding a yellow microcrystalline solid. Yield: 82 %. ^{1}H NMR (500 MHz, Varian Unity, collected in D_2O): 8.07 (s), 7.91 (s), 4.32 (t), 3.18 (m). IR: 3146.55 cm^{-1} (w), 1735.57 (s), 1544 cm^{-1} (s). ESI-MS: 307 m/z and 306 $(M+H)^+$.

Synthesis of 3-NT_{C-C} (2,2'-(6,6'-dihydroxy-5,5'-dinitro-[1,1'-biphenyl]-3,3'-diyl)-bis-(1-carboxy-ethanaminium). Synthesis of the C-C coupled 3-NT dimer was

achieved in reaction of the 5-bromo-3-nitrotyrosine (50 mg, 163 mmol) and 3-nitrotyrosine (55 mg, 243 mmol) in the presence of $[Cu(MeCN)_4]BF_4$ (75 mg, 238 mmol) and Cs_2CO_3 (165 mg, 506 mmol) under anaerobic conditions in 20 mL of dry DMF. The reaction mixture was allowed stir for 1 h at which time the solvent was evaporated of to one-third the original volume. Upon addition of 6-8 of mL 50:50 methanol/ethyl acetate solution a fine powdery solid formed. The solid was filtered off and the filtrate was collected. Addition of dry diethyl ether afforded a pale yellow product. Yield: 12%. ^{1}H NMR (500 MHz, Varian Unity, collected in D_2O): 8.05 (s), 8.02 (s), 7.90 (s) 7.54 (d) 7.17 (d) 4.12 (t), 3.19 (m). ESI-MS (m/z) = 451 $[M+H]^+$.

4.8.1 Experimental Data

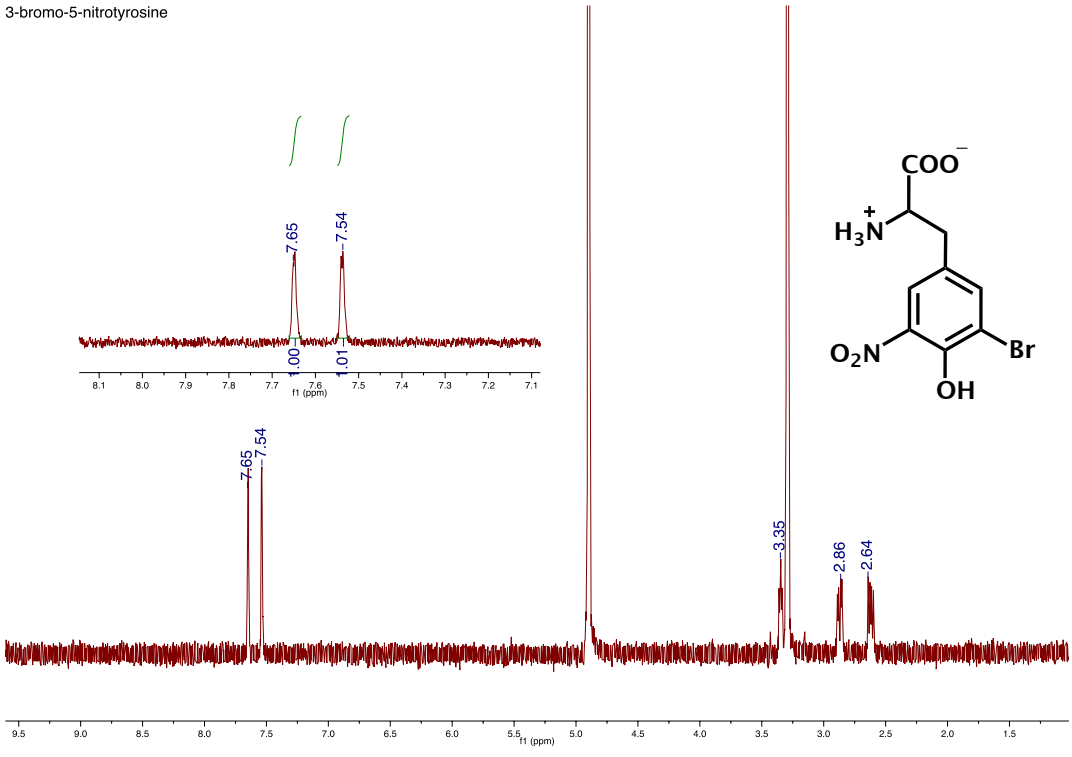

Figure 4.13. ^{1}H-NMR of synthesized 3-bromo-5-nitrotyrosine collected in D_2O.

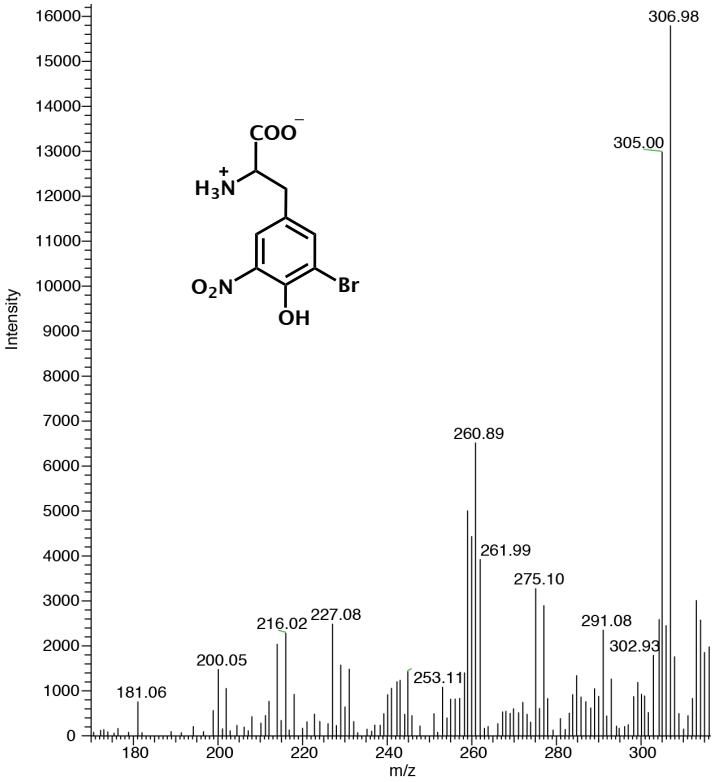

Figure 4.14. Mass spectrum of 3-bromo-5-nitrotyrosine.

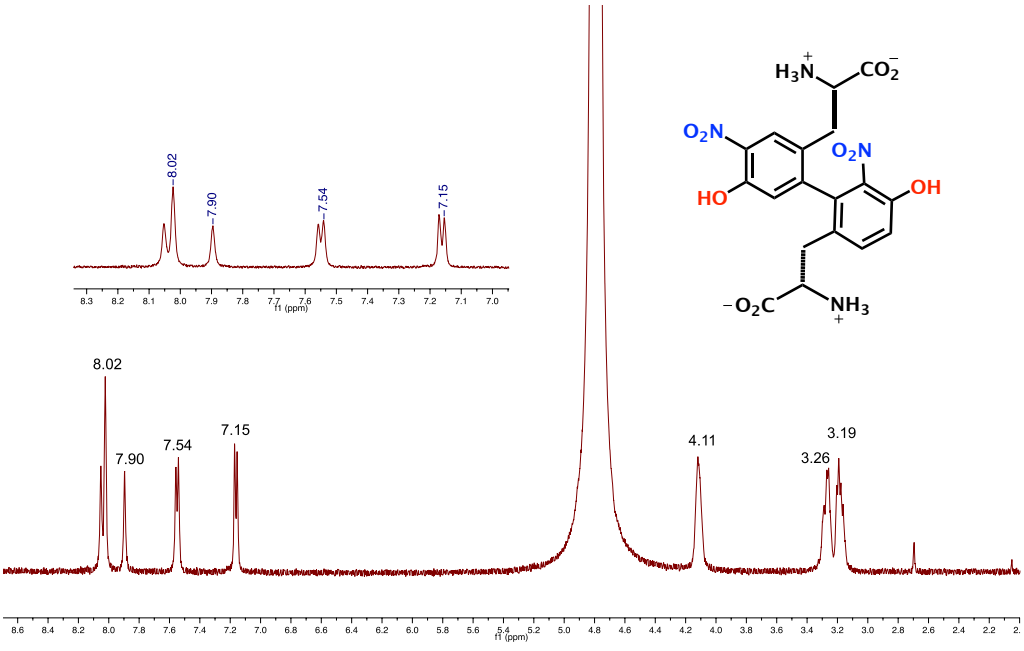

Figure 4.15. ^{1}H-NMR of 3-NT dimer (**3-NT$_{C\text{-}C}$**) collected in D_2O.

4.9 References

1. Radi, R., *Acc. Chem. Res.*, **2013**, *46*, 550-559.
2. Radi R., *Proc. Nat. Acad. Sci.*, **2004**, *101*, 4003-4008.
3. Szabó, C., Ischiropoulos, H., and Radi, R., *Nat. Rev. Drug. Discov.*, **2007**, *6*, 662-680.
4. Pacher, P., Beckman, J.S., and Liaudet, L., *Physiol. Rev.*, **2007**, *87*, 315-424.
5. Greenacre, S.A.B. and Ischiropoulos, H., *Free. Rad. Res.*, 2001, *34*, 541-581.
6. Abello, N., Kerstjens, A.M., Postma, D.S., and Bischoff, R., *J. Proteom. Res.*, **2009**, *8*, 3222-3238.
7. Warren, J.J.; Winkler, J.R.; Gray, H.B., *FEBS Lett.*, **2012**, *586*, 596-602.
8. Sjödin, M.; Styrine, S.; Kermark, B.; Sun, L.; Hamsmarström, L.; *J. Am. Chem. Soc.*, **2000**, *122*, 3932-3936.
9. Sjödin, M.; Styrine, S.; Wolpher, H.; Xu, Y.; Sun, L.; Hamsmarström, L.; *J. Am. Chem. Soc.*, **2005**, *127*, 3855-3863.
10. Beletaskaya, I.O.; Cheprakov, A.V., *Coord. Chem. Rev.*, **2004**, *248*, 2337-2367.
11. March J., *Advances in Organic Chemistry: Reactions, Mechanisms and Structures* Ch. 10, pp 460-465, **1992**, Wiley Interscience, New York.
12. Bunnett, J. F. and Zahler, R. E., *Chem. Rev*. **1951**, *49*, 273-412.
13. Carraway, K.L.; Koshland, D.E., *Biochim. Biophys. Acta.*, **1968**, *165*, 274-276.
14. Boesel, R.W.; Carpenter, F.H., *Biochem. Bioph. Res. Co.*, **1970**, *38*, 678-682.
15. Bruice, T.C.; George, M.J.; S.L. Walters, *J. Am. Chem. Soc.*, **1968**, *90*, 1612-1619.

16. Giasson, B.I., Duda, J.E., Murray, I.V.J., Chen, Q., Souza, J.M., Hutig, H.I., Ischiropoulos, H;, Trojanowski, J.Q.; Lee, V. M.-Y., *Science*, **2000**, *290*, 985-989.

17. Souza, J.M.; Giasson, B.I.; Chen, Q.; Lee, M.-Y.; Ischiropoulos, H., *J. Biol. Chem.*, **2000**, *275*, 18344-18349.

18. Griffiths-Jones, S.R.; Maynard, A.J.; Searle, M.S., *J. Mol. Biol*., **1999**, *292*, 1051-1069.

19. (a) deBoer, T.R.; Resendez, A.; Mascharak, P.K., *ChemBioChem*, **2013**, *14*, 2106-2109. (b) deBoer, T.R., Palomino, R.I., Idiga, S.O., Millhauser, G.L., and Mascharak, P.K., *J. Inorg. Biochem.*, **2013**, *138*, 24-30 (2013).

20. Tsikas, D. and Duncan, M.W., *Mass Spectrom. Rev.*, **2014**, *33*, 237-276.

21. Harms. G.S., Pauls, S.W., Hedstron, J.F., and Johnson, C.K., *J. Fluoresc*., **1994**, *7*, 283- 292.

22. DiMarco, T. and Giulivi, T., *Mass Spectrom. Rev.*, **2007**, *26*, 108-120.

23. Katrantzis, M., Baker, M. S., Handley, C. J., and Lowther, D. A., *Free Rad. Biol. Med.*, **1991,** *10*, 101-109.

24. Molina, C., Kissner, R. and Koppenol, W.H., *Dalton Trans.*, **2013**, *24*, 9898-9905.

25. E.R. Altwicker., *Chem. Rev.*, **1967**, *67*, 475-531.

26. Goers, J.; Bog-Manning, A.B.; McCormack, A.L.; Millett, I.S.; Doniach, S.; Di Monte, D.; Uversky, V.; Fink, A.L., *Biochem*., **2003**, *42*, 8465-8471.

Chapter 5. Exploring the Metabolites of Anti-Inflammatory Pharmaceuticals under Sustained Exposure to Peroxynitrite and its Precursors

5.1 Background

In chapters 3 and 4, the PN-mediated pathways were studied to establish the utility of the two-component PN-generating platform as a bioanalytical tool and to explore the dynamic chemistry of PN. While control studies were commonly performed in which the flux ratios of nitric oxide (NO) to superoxide ($O_2^{\bullet-}$) were modulated, work dedicated to emphasizing the *two-component* feature of the platform had not been thoroughly established. With this goal in mind and with intentions of developing a project that could be explored by future researchers in the Mascharak group, we chose to study the metabolites of a set of pharmaceuticals exposed to NO, $O_2^{\bullet-}$, and PN. Impetus for this work spurs from a significant body of work discussed throughout the preceding chapters that have firmly linked PN to many inflammation-mediated diseases. Because hepatotoxicity remains a predominant adverse effect of many anti-inflammatory drugs, investigation into the metabolites formed in the presence of PN and its precursors could reveal potential species that could show enhanced toxicological effects in the liver.

5.1.1 Inflammation and Liver Toxicity

The liver represents an *in vivo* locale susceptible to inflammatory responses as it functions to metabolize pharmaceuticals and detoxify unwanted metabolites. Drugs such as acetaminophen (APAP) have been shown to evoke hepatoxocity after biotransformation by cytochrome P450 to form reactive metabolites such as N-acetyl-*p*-benzoquinone imine (NAPQI).[1] NAPQI, a cytotoxic molecule, is capable of covalently coordinating to thiols groups of glutathione and protein cysteine residues,

thus depleting the effective antioxidant capacity of the liver tissue and potentially introducing further hepatotoxic effects.[2] Further, localization of 3-nitrotyrosine and NAPQI-cysteine adducts in hepatic centrilobular cells following administration of toxic doses of APAP to mice, suggests a possible implications of PN in the toxic events associated with APAP-induced hepatocyte damage.[3]

Many of the drugs currently on the market contain phenyl moieties within their scaffolds. While phenyl rings decorated with hydroxide substituents show enhanced susceptibility towards PN-mediated modifications, phenyl-containing amino acid phenylalanine has also been observed to undergo chemical modifications upon exposure to PN.[4] In addition to hydroxylation, phenylalanine has been reported to form 3-nitrotyrosine and dinitro- and dinitro-hydroxy adducts. Dinitrophenols exhibit severe toxicity arising from uncoupling of mitochondiral oxidative phosphorylation, and nitronaphthalenes are pulmonary toxicants.[5] Further, nitrated phenolic derivatives such as *p*(*p*-nitrophenoxy) phenol represent a class of compounds known to be metabolized by cytochrome P450 to yield reactive benzoquinone species.[6] In addition to nitrophenols, catechol molecules are also able to generate similar reactive semiquinone species (Figure 5.1). However unlike the nitrophenols that most commonly require metabolism by P450 to yield reactive metabolites, catechols require only simple oxidants and or heavy metals such as iron or copper.[7]

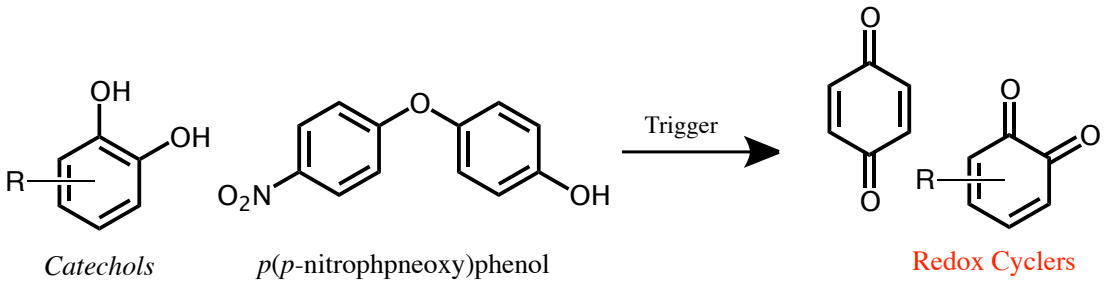

Figure 5.1. Chemical scheme representing the transformation of nitrophenols and catechols to their reactive quinone counterparts that give rise to semiquinone species.

Toxicity of quinone metabolites arises from their ability to initiate redox cycling (generating $O_2^{\bullet -}$) that can covalently bond to DNA, RNA, and other cellular macromolecules.[2] Such findings provide the impetus for chemical exploration of the metabolites generated when these medications are exposed to PN. While various cytotoxicity and epidemiology studies have established the relationship between reactive oxygen and nitrogen species (ROS and RNS, respectively) and drug-induced hepatotoxicity,[8,9] bioanalytical investigations of the prospective secondary metabolites of pharmaceuticals upon exposure to RNS and ROS's have not been completed as thoroughly.

5.1.2 Design of the Experimental System

Based on our work completed previously (discussed in chapter 3) where ~40% nitration of tyrosine was achieved within the wells of a second-generation PN-generating platform after only 30 minutes, it was inferred that drugs containing a phenol moiety would be considerably susceptible to PN-mediated modification.[10] For

this reason we focused our attention towards drug molecules that contain a phenol group within their chemical frame. A set of therapeutics was chosen to systematically evaluate the contribution of functional groups on the reactivity of the drug towards PN, NO, and $O_2^{\bullet-}$. The compendium of drug molecules includes APAP, 5-aminosalicylic acid (5-ASA) and phenylbutazone (bute), shown in Figure 5.2. Additionally, to provide the most fundamental point of reference, we also investigated the reactivity of phenylalanine towards PN, NO and $O_2^{\bullet-}$ in the wells of our platform.

Comparison of the structures in Figure 5.2 highlights the modulatory transformation of the fundament phenyl ring of phenylalanine (far left), first with the addition of a hydroxyl group in tyrosine, followed by the replacement of the methylene group of tyrosine with a carboxamide group in APAP, and finally with the replacement of the carboxamide group of APAP with an amine and the addition of carboxylic acid *ortho* to the hydroxide group in 5-ASA. Lastly, bute was included in this list. Although this molecule lacks a phenol moiety it has been observed to be highly reactive towards PN. The enhanced activity may be attributed to the pyrazolidinedione addition in comparison to the methylene group of phenylalanine.

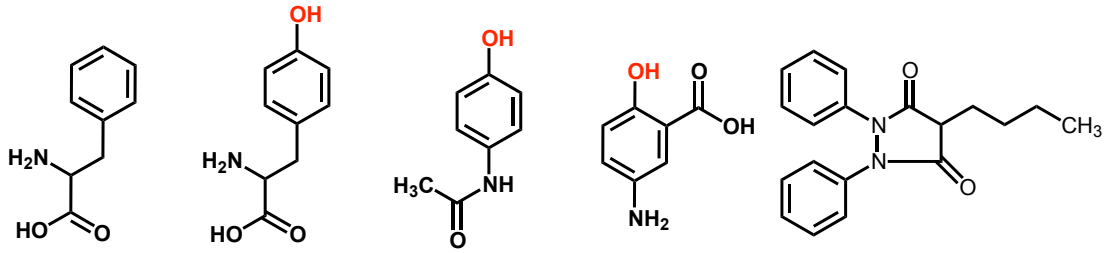

Figure 5.2. Chemical structures of the selected pharmaceuticals.

5.1.3 Acetaminophen (APAP)

Acetaminophen is one of the most commonly administered analgesic and antipyretic used to treat pain and fever.[8,9] Interestingly, in 2009 the FDA noted that acetaminophen toxicity was a leading cause of acute liver failure.[8] Similarly, non-steroidal anti-inflammatory drugs (NSAIDs) have also been strongly associated with hepatotoxicity. Numerous studies substantiating a link between APAP and ROS/RNS's have been reported. In fact, it has been well established that APAP overdose can result in increased production of NO and $O_2^{\bullet-}$.[11] However, exploration into the potential metabolites of APAP formed in the presence of PN, NO or $O_2^{\bullet-}$ remains absent in the literature.

5.1.4 5-Aminosalicylic Acid (5-ASA)

Compared to APAP, 5-ASA has been shown to elicit much more mild toxicological effects. 5-ASA (also referred to as Mesalamine) has been used to treat inflammatory bowl ailments such as ulcerative colitis and Crohn's disease and acts as a rapid antioxidant.[12,13] It has been widely accepted that increased fluxes of NO and PN are released at local sites of gut inflammation, and chronic and sustained release of these and other reactive species is attributed to the progression of inflammatory bowel states and the onset of colon cancer.[14,15]

Work completed by Halliwell and coworkers comparing the antioxidant capacity of APAP and 5-ASA showed comparative action.[16] Pertinent results of this study are shown in Figure 5.3. In this work PN was employed as the oxidant species, and the anitoxidative capacity of APAP and 5-ASA were measured as a function of PN-

mediated nitration to tyrosine to 3-nitrotyrosine (3-NT). The plot in Figure 5.3 shows the extent of 3-NT inhibition. While both APAP and 5-ASA have the capacity to act as strong antioxidants, their significant toxicity lies in the difference in metabolism. 5-ASA, more effectively reaches its target at the intestines compared to APAP that accumulates in higher concentrations in the liver.[3]

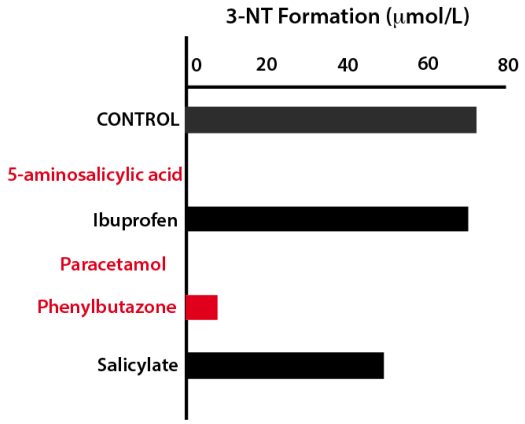

Figure 5.3. Plot representing the relative inhibition of selected pharmaceutical against PN-mediated nitration of tyrosine. Structures of ibuprofen and salicylic acid are shown on the right for reference in the text.

5.1.5 Phenylbutazone (bute)

Phenylbutazone, more commonly known as bute, is a NSAID that was introduced in the 1948 by Wilhemi *et. al*. for the treatment of rheumatoid arthritis (RA).[17] However, its use was quickly restricted once it was found that severe and irreversible liver damage developed when bute was combined with APAP and many other common analgesics.[18] While bute was observed to be a potent anti-inflammatory agent for the treatment of RA at joints, the unintended toxicity of the therapeutic at the liver ultimately lead to its cessation as a therapeutic in humans.

The antioxidant capacity of bute was also studied by Halliwell *et. al* who demonstrated significant inhibition of nitration of tyrosine by PN. Structural comparison of the therapeutics listed in Figure 5.2 initially predicts bute to be significantly less reactive towards oxidant PN than those containing phenolic moieties. In general, phenol moieties are more reactive towards oxidation than a phenyl ring, and hence tyrosine is more commonly utilized in biology as a redox center than phenylalanine.[19] However the lack of substituents could in fact make the phenyl rings of bute susceptible to a wide variety of modification and potential hydroxylation of one of the rings by PN could result in the formation of a significant more reactive metabolite.

Because therapeutics account for one-third to one-half of acute liver failure, design and construction of new and alternative analytical tools to study the metabolomics of drugs have emerged.[20] Moreover, reactive oxygen and nitrogen species have been established to be tightly connected to inflammation and the drugs employed to attenuate inflammation.[15,20] We therefore chose to explore the metabolites of phenyl-containing drugs acetaminophen, 5-aminosalicylic acid, and phenylbutazone generated in the presence of reactive oxygen and nitrogen species NO, $O_2^{\bullet -}$, and PN. These reactions were performed in our previously designed two-component PN-generating platform that allows one to study the chemistry of all three species in a single multi-well plate. Given the established hepatotoxicity of catechol and nitrophenol molecules, formation of similar derivatives upon reaction of the

selected drugs by the reactive species (NO, $O_2^{\bullet-}$, and PN) could indicate a pathway of therapeutic toxicity of the pharmaceuticals in the body.

5.2 Peroxynitrite-Generating Platform Construction

To explore the metabolites of the selected drug molecules upon exposure to PN, NO, and $O_2^{\bullet-}$, an alternative second-generation PN-generating platform (24-well plate)[10] was designed, where lanes were prepared that released only NO and $O_2^{\bullet-}$ in addition to PN (as shown in Figure 5.4). These wells were constructed by incorporating a single prefabricated Mn(NO)•SG piece, a single prefabricated XO-CAT•SG piece to generate $O_2^{\bullet-}$, or by combing two sol-gel pieces together to evolve NO, $O_2^{\bullet-}$, or PN respectively (where, Mn(NO)•SG = metal nitrosyl encapsulated sol-gel piece, XO-CAT•SG = xanthine oxidase and catalase encapsulated sol-gel piece). Release of NO was initiated by exposing the plate to light, while $O_2^{\bullet-}$ was evolved by adding the xanthine oxidase substrate hypoxanthine (as described in Chapter 2). To assure homogeneity of the well content, the platform was undulated on a plate rocker throughout the time of exposure to the respective reactive species.

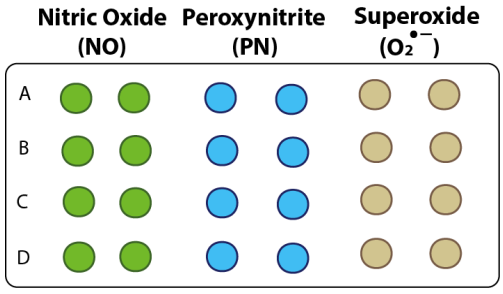

Figure 5.4. Schematic of the designed second-generation PN-generating platform that also contains lanes of a 24-well plate dedicated to exploring the chemistry of NO and $O_2^{\bullet-}$ with selected pharmaceuticals.

5.3 Characterization of the Metabolites of Acetaminophen

In the wells of the designed platform APAP was exposed to NO, $O_2^{\bullet-}$, or PN for 30 minutes. The wells were prepared to final concentrations of 0.160 mM of APAP, 0.250 mM of hypoxanthine (HX), and 4 mM of $NaHCO_3$ (CO_2 source) in a final volume of 0.700 mL (pH 7.4, 0.01 mM phosphate buffer). At the end of 30 minutes the well content was collected, centrifuged, filtered, and characterized by HPLC and mass spectrometry. The HPLC chromatograph of the well content collected from the PN-generating wells are shown in Figure 5.5 where two predominant products are observed at times 4.859 and 18.256 min. The HP 1100 series HPLC is equipped with a multichannel diode array detector that allows for the detection of samples over five selected wavelengths, chosen as 220, 280, 310 and 360 nm. Additional peaks with retention times 9.754, 5.856, and 3.944/4.197 min (Figure 5.5) correspond to unreacted APAP, HX, byproducts of the $O_2^{\bullet-}$-generating system, respectively.

Analysis of the peak at 4.859 min shows an absorbance profile where the 280 nm signal is more pronounced than the 220 nm signal in contrast to many of the other peak in the chromatograph. Collection and mass spectral analysis of this peak showed a dimer $[M+H]^+$ peak at 303 m/z, and a $[M+Na]^+$ peak at 325. Further mass spectral m/z values are shown in Table 5.1. APAP is a neutral molecule with a molecular weight of 151.2 Da but is observed at $[M+H]^+$ by mass spectroscopy at 152 m/z on the *Micromass* ESI-MS (run in positive ion mode).

Analysis of the second predominant peak at a retention time of 18.256 min in the HPLC chromatograph identifies absorbance profile as the characteristic of a nitrated

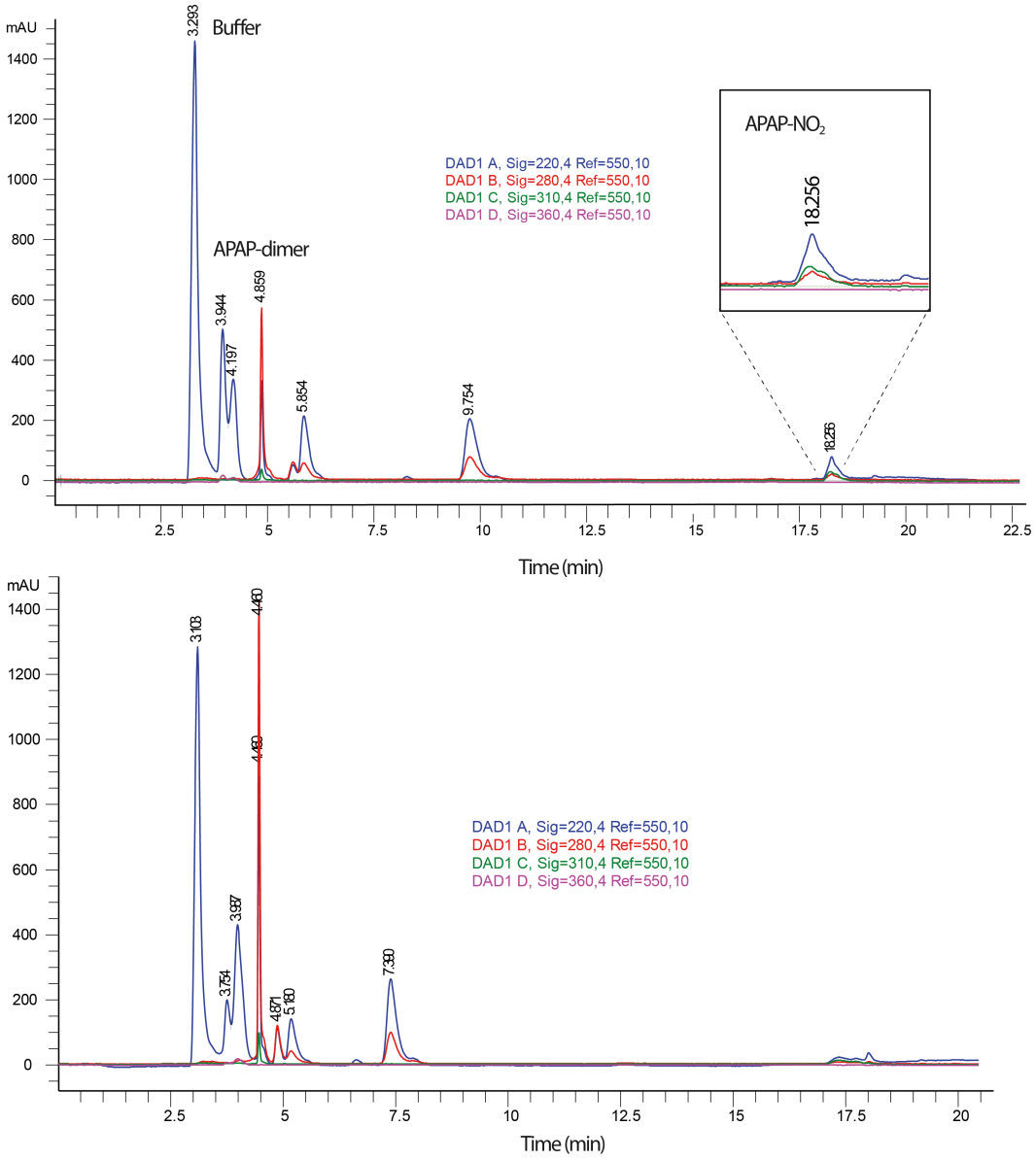

Figure 5.5. HPLC chromatograph observed in the analysis of sample collected following exposure of APAP to PN in the presence (top) and absence (bottom) of CO_2. In the top chromatograph the inset magnifies the peak at retention time 18.256 min that corresponds to the proposed nitration product of APAP.

Table 5.1. Mass spectral peaks observed in the data collection of studies where APAP was exposed to PN. In the top three rows the mass spectral peaks are shown that correspond to the product collected at time 4.859 min following separation by HPLC, and in the bottom two rows are the mass spectral peaks that correspond to the product collected at 18.256 min.

Parent Species	Mass Addition	*m/z*
Retention Time = 4.859 min		
APAP	-	152 ($[M+H]^+$)
APAP (151.1Da)	APAP (151.1 Da)	303($[M+H]^+$)
APAP Dimer (302 Da)	Na (22.9 Da))	325 ($[M+Na]^+$)
Retention Time = 18.256 min		
APAP	NO_2 (46 Da)	197 ([M+H])
APAP-NO_2	Na (22.9)	219 ($[M+Na]^+$)

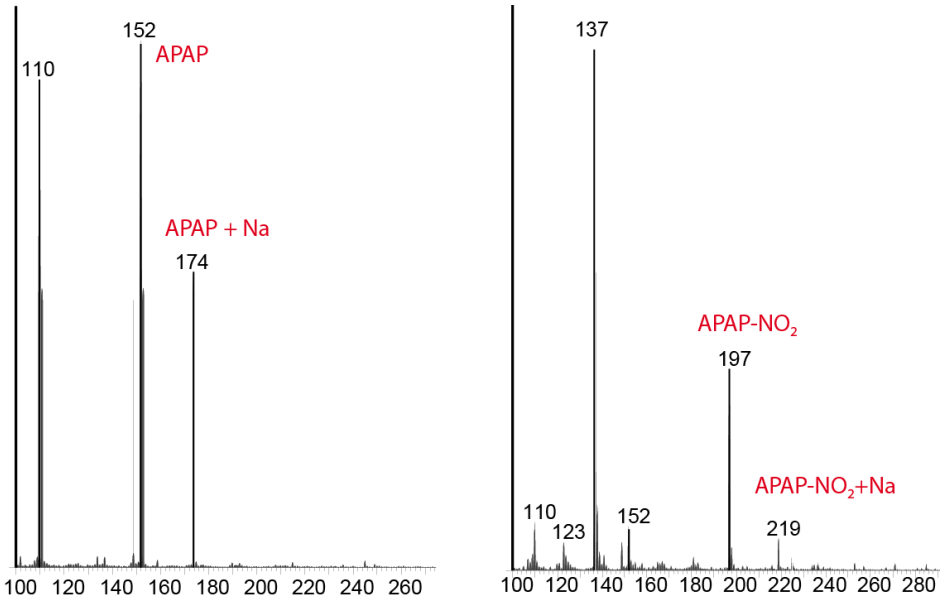

Figure 5.6. Mass spectrum of standard APAP (*left*) and APAP-NO_2 (*right*) solutions, both prepared in buffer (pH 7.4, 0.01 M phosphate buffer) and later treated with mass spec buffer to acidify the solution.

product with observable signals of 220, 280 and 310 nm. Spiking of this peak at 18.256 min with a standard solution of 5-nitroacetaminophen resulted in an increase in the intensity of this peak. Mass spectral analysis of the peak showed a $[M+H]^+$ value at 197 m/z and a $[M+Na]^+$ at 219 m/z, before spiking. To further corroborate PN-mediated nitration of APAP in the PN-generating well, a second set of experiments were conducted in the absence of $NaHCO_3$. After 30 minutes of exposure the well content was processed as discussed above. The HPLC trace of the sample is shown in Figure 5.5. As expected, the intensity of the peak observed at 18.26 min that corresponds to nitrated APAP (APAP-NO_2) was strongly diminished. In contrast the peak corresponding to APAP dimerization increased. Because our focus remained on identifying nitrated and hydroxylated metabolites we did not further study this PN-mediated coupling event.

In adjacent wells where APAP was exposed to NO and $O_2^{\bullet-}$ under identical conditions to those described in the PN studies above, no predominant products were observed in the HPLC chromatographs. In both, small peaks were observed in the ~17-20 min range and yields of all products were below the mass spectral detection limit.

5.4 Characterization of the Metabolites of 5-Aminosalicylic Acid

As described above, 5-ASA was exposed to NO, $O_2^{\bullet-}$, or PN in the wells of the platform. Wells were prepared to final concentrations of 0.160 mM of 5-ASA, 0.250 of mM HX, and 4 mM of $NaHCO_3$ (CO_2 source) in a final volume of 0.700 mL (pH 7.4, 0.01 mM phosphate buffer). At the end of 30 min the well contents were

collected, centrifuged, filtered, and characterized by HPLC and mass spectrometry. The HPLC chromatograph of the well content collected from a PN-generating well is shown in Figure 5.7. Two predominant peaks at 25.527 and 26.496 min were observed. The first peak displayed an absorption profile indicative of a nitrated product. The peak 26.496 min showed a unique profile where the 210 nm signal was strong, but lower energy signals at 310 and 350 nm were also present. Mass spectral analysis of the two separated peaks were completed. The spectrum of the product collected at 25.527 min by HPLC is shown in the bottom panel of Figure 5.7. This spectrum contains a [M+H]+ peak at 199 m/z that corresponds to an addition of 46 Da, indicating a nitrated 5-ASA product.

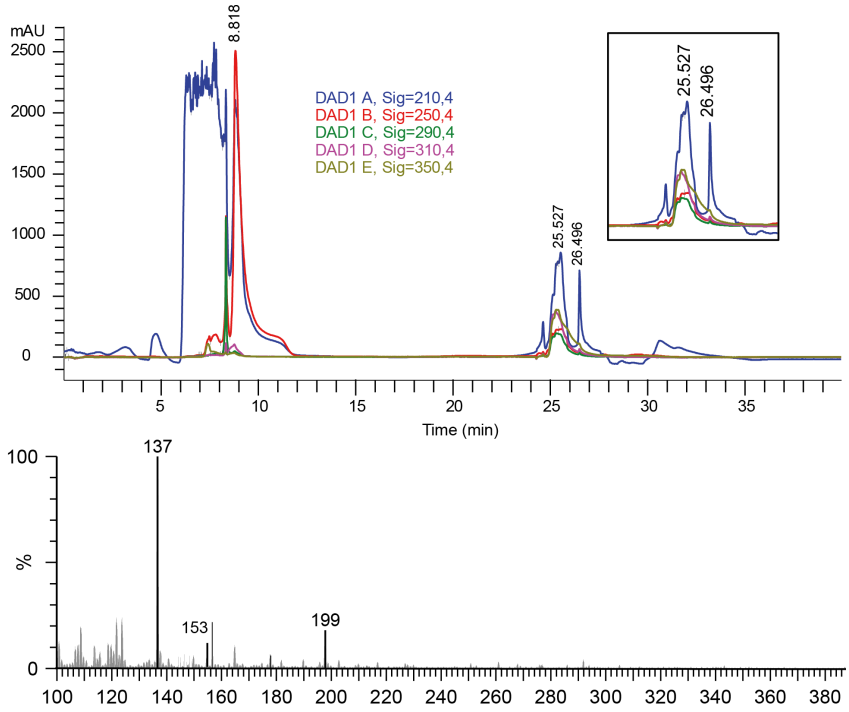

Figure 5.7. HLPC chromatograph of well content, where 5-ASA was exposed to PN for 30 minutes is shown in the top panel. Corresponding mass spectrum of the peak collected at the retention time 25.527 min is shown in the bottom panel.

Mass spectral analysis of the peak collected at time 26.496 minutes was much more complex. The mass spectrum showed a higher weight product with an m/z value of 352. The fragmentation of this peak was much more complex and 5-ASA is known to undergo oxidation-induced polymerization to higher weight oxidative products.[21,22] It is highly plausible that PN initiates dimerization or polymerization of the drug molecules. An example of one such oxidative product is shown in Figure 5.8.

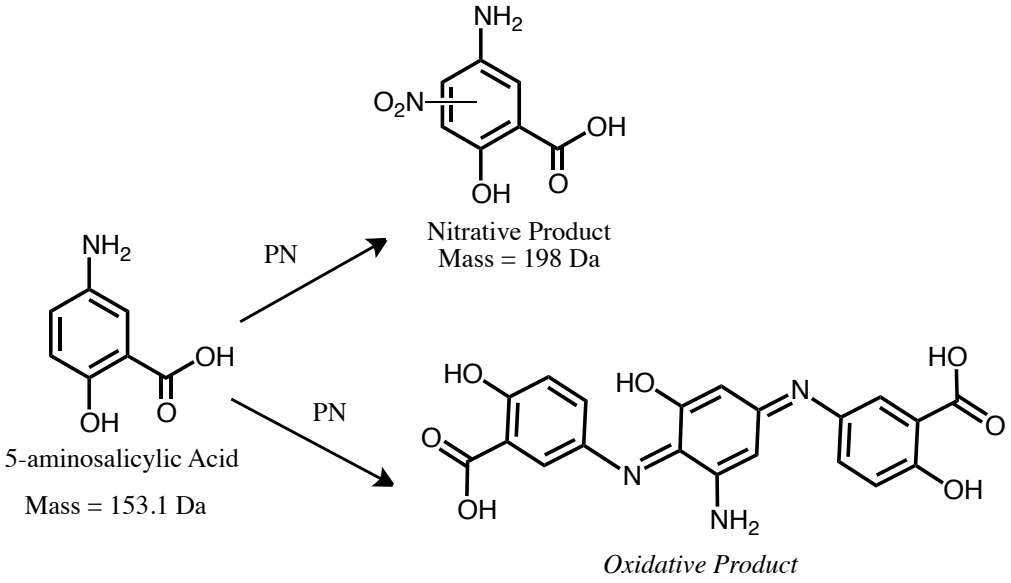

Figure 5.8. Chemical structures of the possible products of generated upon exposure of 5-ASA to PN within the wells of the platform.

In comparative studies, carried out in the wells of the platform where 5-ASA was exposed to NO, minimal change in the HPLC trace of the sample collected from the NO-evolving wells was noted. However, when 5-ASA was exposed to $O_2^{\bullet -}$, two predominant peaks were observed at retention times of 18.094 and 19.752 min (Figure 5.9). Similar to the proposed oxidative product observed in the PN-generating

wells, both peaks displayed unique absorbance profiles with strong 210 nm maximum. Peaks from 4 min to 6.5 min correspond to unreacted 5-ASA and HX, and the byproducts of the $O_2^{\bullet-}$-generating system. A closer look at the peak at 18.094 min showed similar extents of absorbance at 250, 290 and 310 nm, while the peak at 19.752 min shows a more intense absorbance at 250 nm verses 290 nm, and an absence of the 310 nm signal. Mass spectral analysis is currently underway to identify the products.

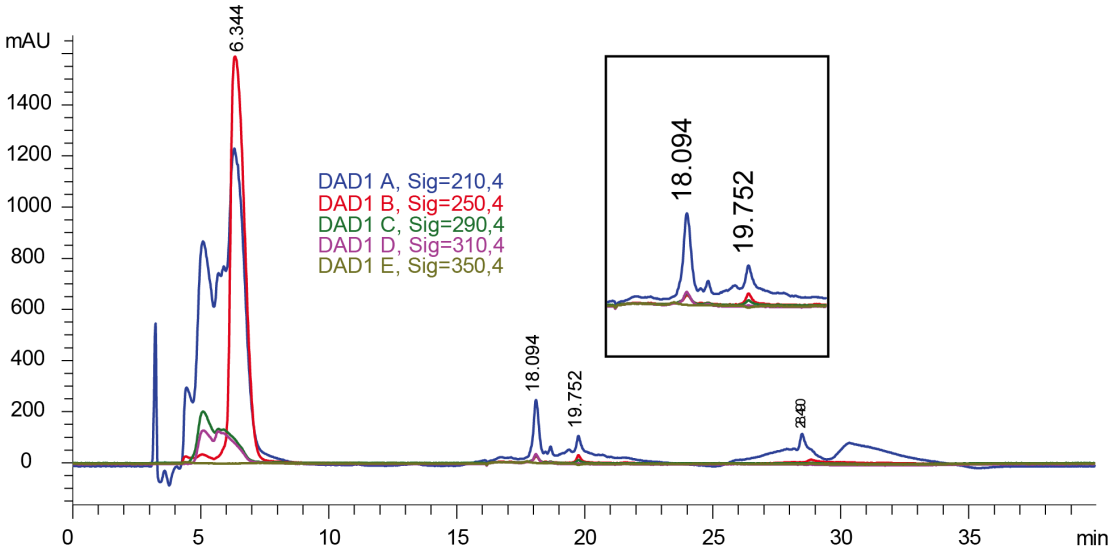

Figure. 5.9. HPLC chromatograph of the well content, where 5-ASA was exposed to $O_2^{\bullet-}$ for 30 minutes.

5.5 Characterization of the Metabolites of Phenylbutazone

Preliminary studies have been conducted to characterize the products of phenylbutazone (bute) in reaction with PN. Similar to previously described procedures, wells were prepared to final concentrations of 0.160 mM of bute, 0.250

mM of HX, and 4 mM of $NaHCO_3$ (CO_2 source) in a final volume of 0.700 mL (pH 7.4, 0.01 mM phosphate buffer). At the end of 30 min, the well content was collected, centrifuged, filtered, and characterized by HPLC. The HPLC analysis of the well content is shown in Figure 5.10, where peaks at times 8.276 and 27.262 min represent HX and bute respectively. Additionally, peaks in the range of 3 min to 5 min have been confirmed to be associated with molecules corresponding to the byproducts of the $O_2^{\bullet-}$-generating system.

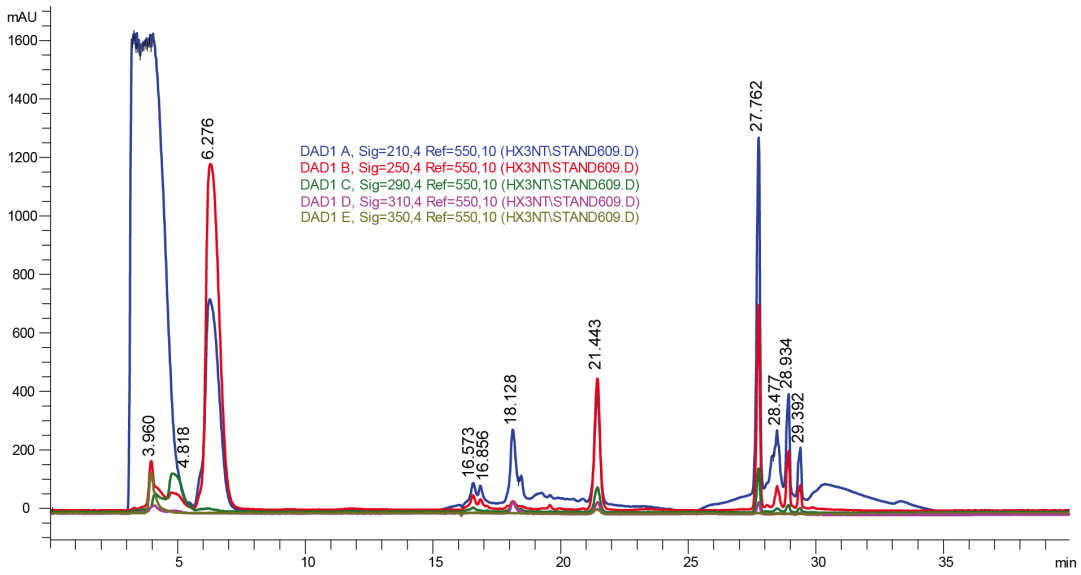

Figure 5.10. HPLC chromatograph of the well content where bute was exposed to PN for 30 minutes.

5.6 Discussion and Future Direction

A general and qualitative evaluation of the preliminary results discussed above highlights one critical point that remains the crux of PN chemistry that can be best phrased as a question, *are there chemical features that make a molecule more*

reactive towards peroxynitrite? Although not all of the metabolites of APAP, 5-ASA, and bute have been identified, it is very evident based on the HPLC chromatograms in Figures 5.5, 5.7, and 5.9 that the chemistry between the phenyl-containing drug is phenylbutazone and PN could be quite complex. In contrast, reactions between PN and APAP and 5-ASA are more selective. Based on the established selectivity of PN towards L-tyrosine and superficial examination of the three structures it could be suggested that APAP would show the most reactivity towards PN (in a very selective fashion). And in fact this observation holds true. The HPLC trace corresponding to the reaction of APAP with PN shows only two predominant products (APAP dimer and APAP-NO_2). The substitution of the methylene carbon of tyrosine for the carboximide –NH group *trans* to the hydroxide group in APAP deactivates the ring towards PN-mediated nitration such that the predominant metabolite of APAP is its dimer, in contrast to tyrosine chemistry where nitration is strongly preferred over dimerization under conditions of high PN flux.

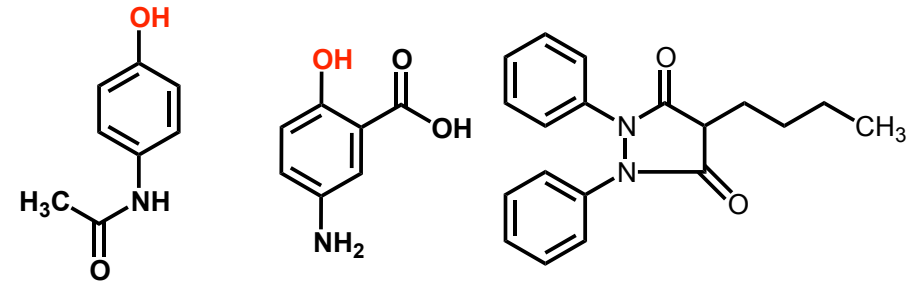

Acetaminophen 5-aminosalicylic Acid Phenylbutazone

Figure 5.11. Chemical structures of the pharmaceuticals studied in the wells of the PN-generating platform.

5-ASA represents a transition from the standard amino acid frames studied previously in the PN-generating platform. This molecule features a phenol ring with an amine substituent at the *para* position and a carboxylic group at the *ortho* position relative to the hydroxide. Decoration of the phenyl ring with an assortment of electron withdrawing and electron donating groups significantly alters the chemistry of the phenol ring, making it incomparable to tyrosine. One significant indicator of chemical divergence of 5-ASA from tyrosine is the pK_a of the hydroxide groups, reported to be 6.0 and 10.07 respectively.[23] Although a nitrated 5-ASA product was identified in the peak observed at 25.527 min, the HPLC trace shows that there are more unidentified products within this broad chromatographic peak. However, it should be noted that an alternative separation method should be developed to (1) sufficiently separate unidentified products under the broad 25.527 peak and (2) improve separation of 5-ASA and HX that are currently indistinguishable under the defined separation method (Experimental Section). Attempts were made to improve separation of 5-ASA and HX using a water and acetonitrile (0.01%TFA) solvent system. However no significant separation was achieved, suggesting that alternative solvent systems should be explored.

An additional observation not be overlooked is the reactivity of 5-ASA towards $O_2^{\bullet -}$. It is this general reactivity towards oxidants and/or radical species that contributes to the significant antioxidant capacity of 5-ASA, a feature that likely contributes to its potential as a therapeutic option to treat chronic inflammatory bowel conditions. Although further work remains to establish the metabolites of APAP, 5-

ASA, and bute, based on the results described above it is evident that the PN-generating platform affords a convenient tool to explore the chemistry of PN and various chemotherapeutics.

A second phase of this work that has yet to be established is the process of screening the identified drug metabolites as potential carcinogenic and/or hepatotoxic agents. Following detailed characterization of the metabolites, the molecules can be synthesized independently or purified from the well experiments and tested in Ames studies and/or hepatitis model.[20,24] Results of these bioanalytical and pharmacological studies can be compiled to create a library of pharmaceuticals with the potential of generating toxic metabolites under exposure of chronic inflammation. Although current pharmacological testing focuses on the toxicity of the metabolic products generated through enzymatic processing (CytP450) in the liver, continued evidence connecting chronic inflammation, peroxynitrite, and disease suggests the need for new and alternative approaches in the design and toxicological characterization of anti-inflammatory drugs.

5.7 Experimental and Methods

Acetaminophen, 5-aminosalicylic acid, and phenylbutazone were purchased from Sigma-Aldrich. All solvent used for high performance chromatography were HPLC grade, including trifluoroacetic acid. For the synthesis of APAP-NO_2 guanadinium nitrate and ACS grade sulfuric acid were also purchased from Sigma-Aldrich.

Synthesis of Peroxynitrite-Generating Platform. Second-generation PN-generating platforms were constructed as described in chapter 2.[10] Individual •NO- and $O_2^{\bullet-}$-generating sol-gel pieces were synthesized through the encapsulation of $[Mn(PaPy_3)(NO)]ClO_4$ ($PaPy_3$= N,N′-bis(2-pyridylmethylamine)-N-ethyl-2-pyridine-2-carboxamide) , xanthine oxidase (XO), and catalase (CAT) solutions into respective tetramethylorthosilicate matrices. Stock solutions of the corresponding reactive species sol-gel mixtures were plated into individual 24-well plates (600μL Mn(NO) sol-gel solution and 800μL, XO-CAT sol-gel solution) and allowed to solidify and dry in the dark for 1 week at 4°C. Activity of the final sol-gel pieces were analyzed at random prior to use with the aid of an NO electrode and electronic absorption spectroscopy. Final plates where constructed by incorporating the respective sol-gel pieces into the wells of a 24-well plate. The final system was designed such that lanes of plate were chosen to release NO, $O_2^{\bullet-}$or PN by incorporating either a single Mn(NO)•SG disc, a single XO-CAT•SG disc, or both discs, respectively. Generation of •NO, $O_2^{\bullet-}$, and PN was initiated with exposure of the plate to low power (10mW) broadband light and the addition of hypoxanthine.

Exposure of pharmaceticals to peroxynitrite. In the wells of the designed platform APAP, 5-ASA and bute were exposed to NO, $O_2^{\bullet-}$, or PN for 30 minutes intervals. The wells were prepared to final concentrations of 0.160 mM of the desired pharmaceutical, 0.250 mM of hypoxanthine, and 4 mM of $NaHCO_3$ (CO_2 source) in a final volume of 0.700 mL (pH 7.4, 0.01 mM phosphate buffer). At the end of 30 minutes the well content was collected, centrifuged, filtered, and characterized by

HPLC and mass spectrometry. In APAP studies an additional experiment was performed in the absence of $NaHCO_3$, where all other conditions were maintained.

Characterization of well content by HPLC. Analysis of well content was carried out using a Hewett Packard 1050 Series HPLC, equipped with a 4.6 mm x 250 mm C18 5U reverse-phase Econosphere Alltech column and diode array detector. Samples were manually injected into a Rheodyne 7225 injection loop and eluted over 30 min with H_2O/ACN (both containing 0.1% trifluoroacetic acid) at a flow rate of 0.8 mL/min. The established solvent method developed as follows.

APAP: 0-15 min isocratic 98:2 (water:acetonitrile, both solvents containing 0.1% trifluoroacetic acid by volume), 15.01-20 gradient 70:30, 20.01-25 gradient 98:2, and 25.01-30 isocratic 98:2. Detection wavelengths included 220 nm, 280 nm, 310 nm and 350 nm with bandwidths of 4 nm. To confirm the formation of nitrated APAP experimental samples were spiked with a stock solution of synthesized APAP-NO_2. Chromatographic peaks were collected and lyophilized (VirTis bench top SLC lyophilizer) for fluorescence and mass spectral analysis and in all subsequent separation methods.

5-ASA: 0-10 min isocratic 100:0 (water:acetonitrile, both solvents containing 0.1% trifluoroacetic acid by volume), 15.01-20 gradient 70:30, 20.01-25 gradient 100:0, and 25.01-30 isocratic 100:0. Detection wavelengths included 220 nm, 280 nm, 310 nm and 350 nm with bandwidths of 4 nm.

Bute: 0-10 min isocratic 100:0 (water: acetonitrile, both solvents containing 0.1% trifluoroacetic acid by volume), 15.01-20 gradient 70:30, 20.01-25 gradient 100:0, and 25.01-30 isocratic 100:0. Detection wavelengths included 220 nm, 280 nm, 310 nm and 350 nm with bandwidths of 4 nm.

Synthesis of nitrated acetaminophen (APAP-NO_2) for spiking. APAP (0.500g, 3.0 mmol) was slowly added to sulfuric acid (5mL, 85% v/v) at 0°C and stirred until the solid was completely dissolved. Guanidinium nitrate (.379g, 3.0 mmol) was added to the reaction mixture over a period of 30 minutes.[25] After stirring for three hours at 0°C, the solution was treated with ice DI water (20mL) and a yellow precipitate formed. The precipitate was dissolved in EtOAc and the aqueous layer was extracted three times with EtOAc (10mL each). The combined organic layers were dried with $MgSO_4$, and the solvent was evaporated in vacuum. The crude residue was purified by column chromatography (3:1, EtOAC:Tol) to give 4-methoxy-3-nitroacetanilide as a yellow solid in 90% yield (0.536g) ^{1}H NMR (500 MHz, CD_3OD) δ 8.42 (d, J=5, 1H), 7.67 (dd, J=5, 10, 1H) 7.09 (d, J=10, 1H), 2.11 (s, 1H).

5.8 References

1. Laine, J.E.; Auriola, S.; Juvonen, R.O., *Xenobiotica*, **2009**, *39*, 11-21.

2. Albano, E.; Rundgren, M.; Harvison, P.J.; Nelson, S.D.; Moldeus, P.; *Molecular Pharmacology*, **1985**, *28*, 306-311.

3. (a) Hinson, J.A.; Roberts, D.W.; James, L.P., *Handb Exp Pharmacol.*, **2010**, *196*, 369-405. (b) Michael, S.L.; Mayeux, P.R.; Bucci, T.J.; Warbritton, A.R.; Irwin, L.K.; Pumford, N. R.; Hinson, J.A., *Nitric Oxide: Biology and Chemistry*, **2001**, *5*, 432-441.

4. Kaur, H.; Halliwell, B., *Anal. Biochem.,* **1994**, *220*, 11-15.

5. Koizumi, M.; Yamamoto, Y.; Ilto, Y.; Takano, M.; Enami, T.; Kamata, E.; Hasegawa, R., *J. Toxicol.Sci.,* **2001**, *26*, 299-311.

6. Plasterer, M.R.; Bradshaw, W.S.; Booth, G.M.; Carter, M.W.; Schuler, R.L.; Hardin, B.D., *J. Toxicol. Env. Health*, **1985**, *15*, 25-38.

7. Schweigert, N.; Zehnder, A.J.; Eggen, R.I.; *Environ. Microbiol.*, **2001**, *3*, 81-91.

8. Blough, E.R.; Wu, M., *Frontiers Pharmacol.*, **2011**, *2*, 1-6.

9. Knight, T.R.; Ho, Y-S.; Farhood, A.; Jaeschke, H.; *J. Pharmacol. Exp. Ther.*, **2002**, *303*, 486-475.

10. deBoer, T.R., Palomino, R.I., Idiga, S.O., Millhauser, G.L., and Mascharak, P.K., *J. Inorg. Biochem.*, **2013**, *138*, 24-30 (2013).

11. Jaeschke, H.; Knight, T.R.; Bajt, M.L., *Toxicol. Lett.,* **2003**, *144*, 279-288.

12. Rembacken, B.J.; Snelling, A.M.; Hawey, Pm.M.; Chalmers, D.C.; Axon, A.T.R., *Lancet*, **1999**, *354*, 635-639.

13. Grisham, M.B., *Lancet*, **1994**, *344*, 859-861.

14. Pavlick, K.P.; Laroux, F.S.; Wolf, R.E.; Gray, L.; Hoffman, J.; Grisham, M.B., *Free Radic. Biol. Med.*, **2002**, *33*, 311-322.

15. van der Vilet, A.; Bast, A., *Free Radic. Biol. Med.*, **1992**, *12*, 499-513.

16. Whiteman, M.; Kaur, H.; Halliwell, B., *Ann. Rheum Dis*., **1996**, *55*, 383-387.

17. Domenjoz, R., *Ann. N.Y. Acad. Sci.,* **1960**, *86*, 263-291.

18. Weiner, M.; Chenkin, T.; Burn, J.J., *Am. J. Med. Sci.*, **1954**, *228*, 36-39.

19. Warren, J.J.; Winkler, J.R.; Gray, H.B., *FEBS Lett.*, **2012**, *586*, 596-602.

20. Tafazoli, S.; Sephar, D.D.; O'Brien, P.J., *Drug Metabol. Revs.*, **2005**, *37*, 311-325.

21. Jensen, J.; Cornett, C., Olsen, C.E.; Bondesen, S.; Christensen, J.; Christensen, L.A.; Tjørnelund, J.; Hansen, S.H., *Biochem. Pharmacol.*, **1993**, *45*, 1201-1209.

22. Jensen, J.; Cornett, C., Olsen, C.E.; Tjørnelund, J.; Hansen, S.H., *Int. J. Pharma.*, **1993**, *45*, 1201-1209.

23. Allgayer, H.; Sonnenbichler, J.; Kruis, W.; Paumgartner, G., *Arzneimittelforschung*, **1985**, *35*, 1457-1459.

24. Maron, D.M.; Ames, B., *Mutation Research*, **1983**, *113*, 173-215.

25. Schmidt, B.; Berger, R.; Hoelter, F., *Organic Biomol. Chem.,* **2010,** *8*, 1406-1414.

APPENDIX

Prelude

Over the last decade our group has maintained a theme of utilizing photoactive metal nitrosyls as effective antimicrobials therapeutics to eradicate a wide spectrum of established pathogens.[1-5] In all accounts a selected metal nitrosyl was incorporated into material frames that acted as inert drug carriers and delivered only therapeutic levels of nitric oxide (NO) to a local site upon illumination, while maintaining the resultant photoproduct within material network. Most recently, the manganese nitrosyl $[Mn(NO)(PaPy_3)]ClO_4$ was loaded into a mesoporous aluminosilicate host and shown to effectively eradicate *Acinetobacter baumannii*.[5] The significance of this work is evident given the multidrug resistance of *A. baumannii* and its emergence as a nosocomial pathogen in military hospitals in Iraq and Afghanistan.

In general, the emergence of antibiotic-resistance has become a serious epidemic that has lead to the transformation of many bacterial strains into "super bugs."[6,7] With continued focus on developing unique therapeutic systems we turned our attention from NO-delivery material systems to silver (I)-based options. Interest in silver as a therapeutic agent stems from its long history as a broad-spectrum antiseptic that has largely avoided resistance acquisition by its pathogen targets. Most commonly, silver has been used in the treatment and maintenance of wounds and burns. Review of the current literature in this area shows a vast and evolving field that has afforded numerous silver-loaded wound dressings. Interestingly, many of the reported dressings continue to employ $AgNO_3$, silver sulfadiazine, and silver nanoparticles as

the predominant sources of bioactive silver (I) ion (Ag^+) that is ultimately responsible for bacterial eradication.

Our entry to this area began with the design a silver (I) complex with fluorescent features that could be incorporated into a material frame to ultimately afford a "trackable" silver-loaded occlusive wound dressing. The unique trackable feature could be utilized as both as an indicator of therapeutic delivery to a wound or burn site and as a fluorometric probe to provide a quantitative profile of silver release from the designed wound dressing. The significance of the later application could prove advantageous in the optimization of drug release from silver-loaded wound dressings. The ability to tune the leaching profile of a material not only assures adequate loading of silver to a target site but also can be exploited to establish the minimum silver loading required to induce therapeutic action. Both effects are equally significant because it has been observed that inadequate delivery of silver at a wound site (i.e. a dosage bellow the established minimal inhibitor concentration, MIC) can result in the development of multidrug resistant bacteria,[8,9]

In the proceeding two appendices, work completed in efforts to establish the groundwork for future research projects in the area of silver-based wound dressing development will be presented. Appendix A highlights synthetic techniques and protocols of silver (I) complexes and Appendix B focuses on the design and construction of a first-generation carboxymethyl cellulose-based wound dressing loaded with the trackable silver (I) complexes $[Ag(ImD)_2]ClO_4$.

Appendix A. Synthesis of $[Ag(PyOH)_2]X$ Complexes: Diverse Topologies Directed by Anion Interactions

A.1.1 Background

Because it has been established that heterocyclic-based silver (I) complexes exhibit antibacterial potential we first sought to establish and standardize synthetic protocols of such complexes.[10,11] We first synthesized coordination complexes of the type $[Ag(PyOH)_2]X$, where PyOH is pyridine derivative 4-pyridylcarbinol and X is anionic couterion NO_3^- (nitrate), BF_4^- (tetrafluoroborate), ClO_4^- (perchlorate), and $CF_3SO_3^-$ (OTf^-, trifilate). Synthesis of the [Ag]X complexes afforded insight into synthetic and crystallization techniques and considerations. Interestingly collected crystallographic data identified unique supramolecular scaffolds in the solid-state structures of these silver complexes as a function of the chosen counter anion.

A.1.2 Synthesis and Characterization of $[Ag(PyOH)_2]NO_3$ (1)

Syntheses of $[Ag(PyOH)_2]NO_3$ (**1**) was achieved by adding of concentrated ethanolic solution of dry PyOH to a rapidly stirred ethanolic solution of the $AgNO_3$. After one hour of stirring the solution was concentrated and cooled to 4° C. After only 5 min a fluffy white microcrystalline solid formed. Clear colorless diffraction quality blocks were obtained by vapor diffusion of diethyl ether into a methanolic solution of the silver complex at 4 °C.

In the solid state structure **1**, the Ag(I) atoms are paired in discrete dimer units along the *c*-axis (deviating 8.83° from the vertical axis) with a Ag−Ag distance of 3.2141(2) Å (Fig. 1). The pyridyl nitrogen of the PyOH ligands linearly coordinates the Ag(I) center, and the aromatic moieties are near planar but display asymmetric interannular torsional angles in the plane orthogonal to the Ag(I) dimer (0.5° and 6.8°). The Ag(I) dimers stack in a staggered fashion impeding long-range p-stacking of the aromatic ring systems. The terminal oxygen atoms of the PyOH ligands weakly interact with adjacent Ag(I) centers of the dimer, namely Ag1···O_{Ligand} 2.794(5) Å and Ag2···O_{Ligand} 3.540(4) Å. The Ag···O interactions may contribute to the observed spatial orientation of the terminal alcohol groups (torsional angles 5.5° and 158°) that

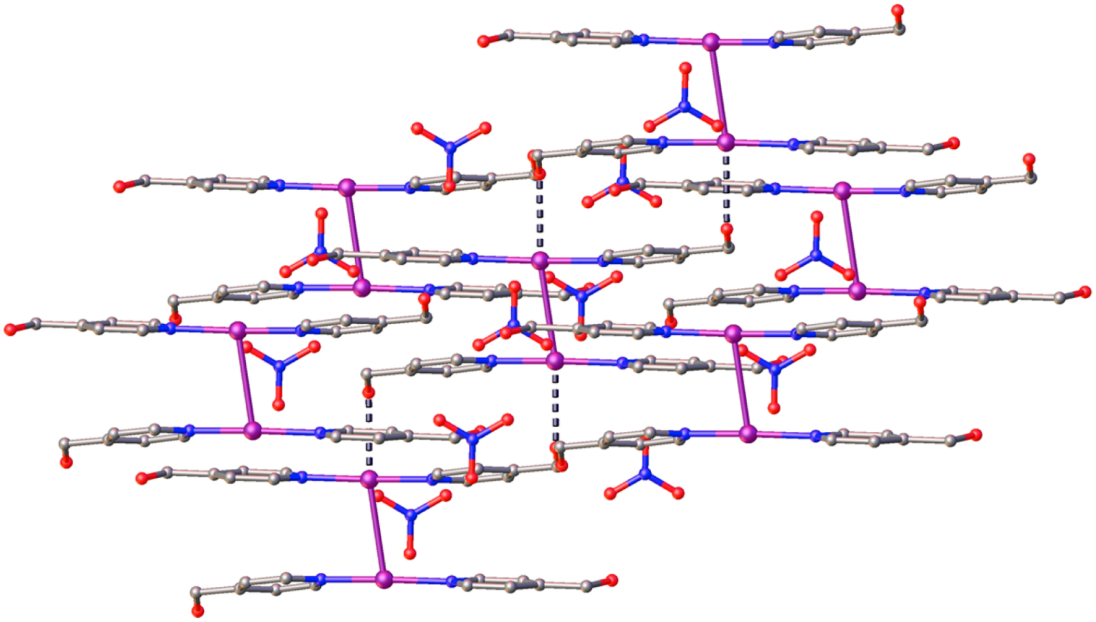

Figure A.1. Crystal structure of complex **1** along the c-axis.

outcompete intermolecular H-bonding. The NO_3^- ions of **1** function to balance the charge of the complex and are embedded within the void spaces in between the dimer units. The NO_3^- counter ion does not appreciably interact with the ligand units of the structure, but instead weakly coordinate to the Ag(I) centers through an oxygen (2.862(5) Å). Overall, the absence of strong intermolecular interactions between the ligand π-system or the terminal OH groups suggest that the structural topology observed in the extended structure of **1** is not guided by the PyOH ligand but by the NO_3^- counter ion.

A.1.3 Synthesis and Characterization of $[Ag(PyOH)_2]BF_4$ (2)

Similar to complex **1**, $[Ag(PyOH)_2]BF_4$ (**2**) was synthesized by adding an ethanolic solution of PyOH to a rapidly stirring $AgBF_4$ solution. Exchange of the trigonal planar NO_3^- counter ion with tetrahedral BF_4^- in **2** resulted in significant structural changes in addition to slightly longer Ag−Ag bond (3.3171 (1) Å). While planar NO_3^- traverses parallel to the Ag−Ag bonds of **1** with the N atom residing near the center of this bond (Ag−N 3.577(4) Å and Ag−N 3.468(4) Å, Fig. 1), BF_4^- ions interact with only one of the Ag centers of the dimeric units in **2** (Ag−F 3.398(4) Å, Fig. 2) Further, significant H-bonding between the F atoms of BF_4^- and the alcohol group of PyOH ligands (2.851(2) Å and 2.808(4) Å) in succession with $Ag\cdots O_{PyOH}$ interactions (3.615(3) Å) induces torsion of the pyridyl rings along the *a-c* plane that results in the near edge-on-edge orientation of the pyridyl rings of the dimer unit (Fig. 2). The orientation of the PyOH ligands along the N−Ag−N axis does not appear to

contribute significant destabilization or stabilization of the dimer units of structures **1** or **2**. In the NO_3^- analogue the methanol groups of the PyOH ligand are oriented in an *anti*-fashion, while in structure **2**, they exist in a *syn*-fashion. It may be expected that spatial arrangement of the OH groups of neighboring PyOH ligands in the dimeric units of **2** would promote H-bonding interactions that would enhance the argentophilicity of the Ag(I) centers. However this was not observed presumably due to tilt of the pyridyl moieties.

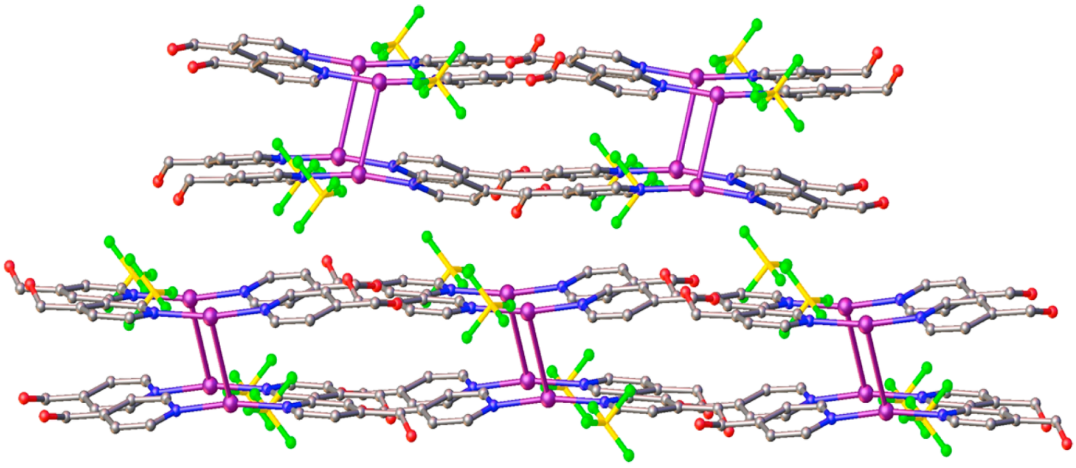

Figure A.2. Crystal structure of complex **2** down the *c* axis.

A.1.4 Synthesis and Characterization of $[Ag(PyOH)_2]OTf$ (3)

Following the synthesis and crystallization procedures described above, clear single-crystal quality plates of $[Ag(PyOH)_2]OTf$ (**3**) were isolated. The crystallographic structure of the triflate-containing complex **3** displays a zig-zag orientation of Ag(I) atoms along the *c* axis, in a Ag1−Ag2−Ag1'−Ag2' fashion, with Ag1−Ag2 and Ag2−Ag1' distances of 3.546(4) and 3.885(4) Å, respectively (Fig. 3, top). The PyOH ligands are linearly coordinated to the Ag(I) centers and are approximately planar. Examination of the structure along the *c* axis highlights the alternating units of $[Ag(PyOH)_2]^+$ eclipsing each other (Fig. 3, bottom).

It has been established that anion-bridging interactions can play a significant role in long-range structural order and the anions of **3** highlights this feature. The $CF_3SO_3^-$ ions link neighboring zig-zag units through H-bonding interactions of the anion with the PyOH groups of one chain (2.575(5) Å) and alternating Ag···O($CF_3SO_3^-$) interactions of another (Fig. 3, top). The spatial orientation of $CF_3SO_3^-$ along the zig-zag chain of Ag(I) centers mirrors that of NO_3 in structure **1**. Alternating Ag···$S_{Triflate}$ interactions (3.887(5) Å and 4.009(5) Å, respectively) are significantly weaker than the non-covalent Ag···N(NO_3) interaction observed in **1** possibly attributed to variability in close packing as a function of the significant size disparity between the molecular volumes of the $CF_3SO_3^-$ and NO_3^- ions (86.9 $Å^3$ and 34 $Å^3$, respectively).

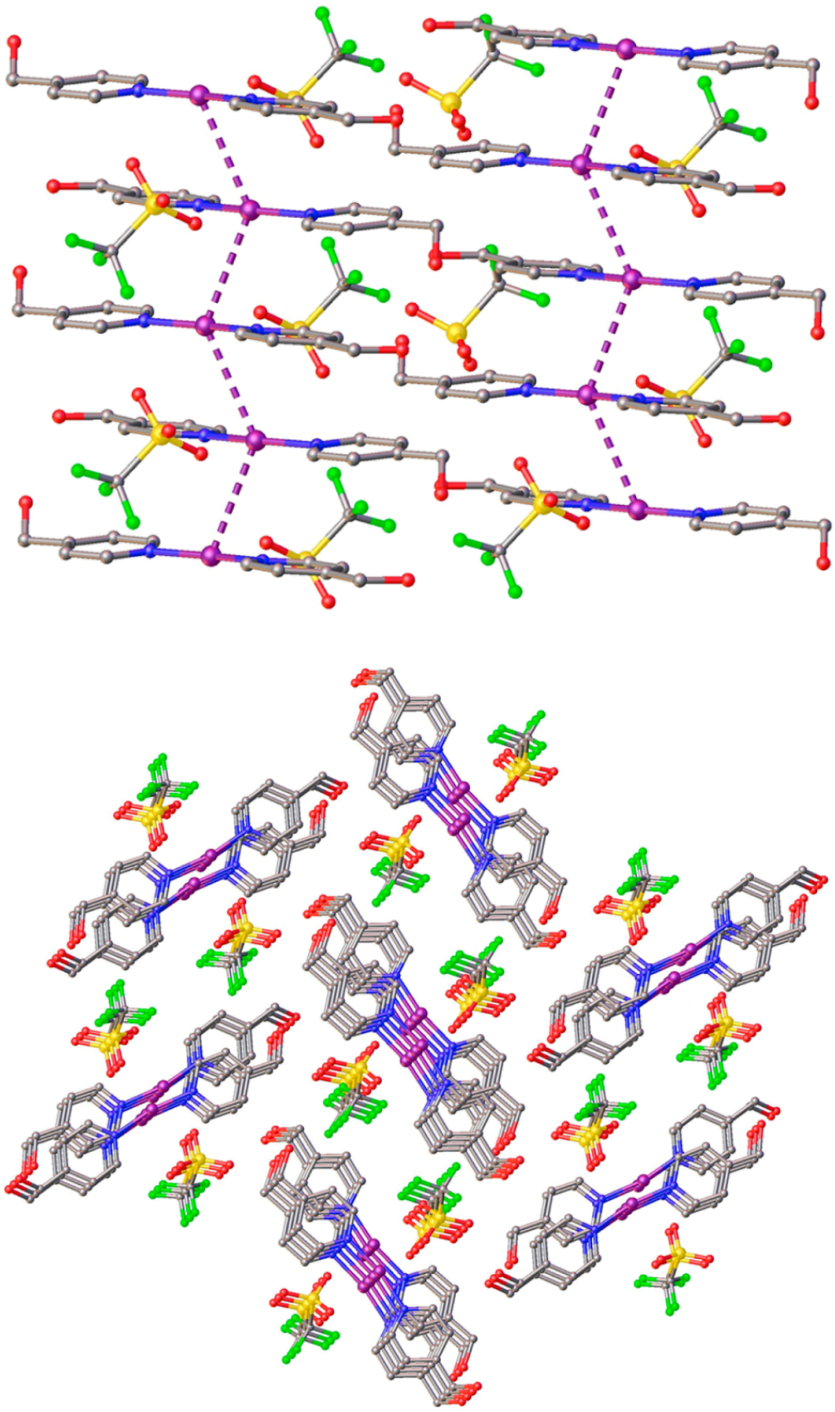

Figure A.3. Crystal structure of complex **3** oriented along **(Top)** and down (**Bottom**) the *c* axis.

A.1.5 Synthesis and Characterization of $[Ag(PyOH)_2]ClO_4$ (4)

Given the poor solubility of $AgClO_4$ in ethanol, $[Ag(PyOH)_2]ClO_4$ (**4**) was synthesized in a mixed solvent system (ethanol-acetonitrile). Similar to the synthetic procedures discussed above, a concentrated enthanolic solution of PyOH was added, this time, to a rapidly stirring solution of $AgClO_4$ in acetonitrile. Clear single-crystal quality needles of **4** were obtained from the reaction solution at 4° C after the solvent was concentrated down to one-half the original volume. The **4** needles were extremely fragile and required immediate crystallographic analysis once removed from the mother liquor. Product left in solution for longer than 24 h quickly began to decompose and visible dark purple deposits were observed on the surface of residual needles. The stability of the **4** needles were significantly less than all others synthesized previously.

In contrast to structures **1, 2** and **3**, the structure of **4** exhibits linear chains of Ag(I) centers stacked along the *c* axis, with alternating covalently linked Ag−Ag dimers (3.241(5) Å) and non-covalent Ag•••Ag (3.462(5) Å) units (Fig. 4, top) in a Ag3-Ag1-Ag2-Ag3'-Ag1'-Ag2' fashion. The pyridyl rings of the Ag3-Ag1-Ag2-A3' chains are staggered and exhibit distinct torsional angles, imposing non-planar stacking of aromatic moieties in the *a* plane (centroid-centroid distances = 3.685 Å, 3.667 Å, and 3.743 Å, respectively). Examination of this catenated building block down the *c* axis highlights the asymmetry of the ligand appendages (Fig. 4, bottom). Cross section of this unit orthogonal to the aromatic

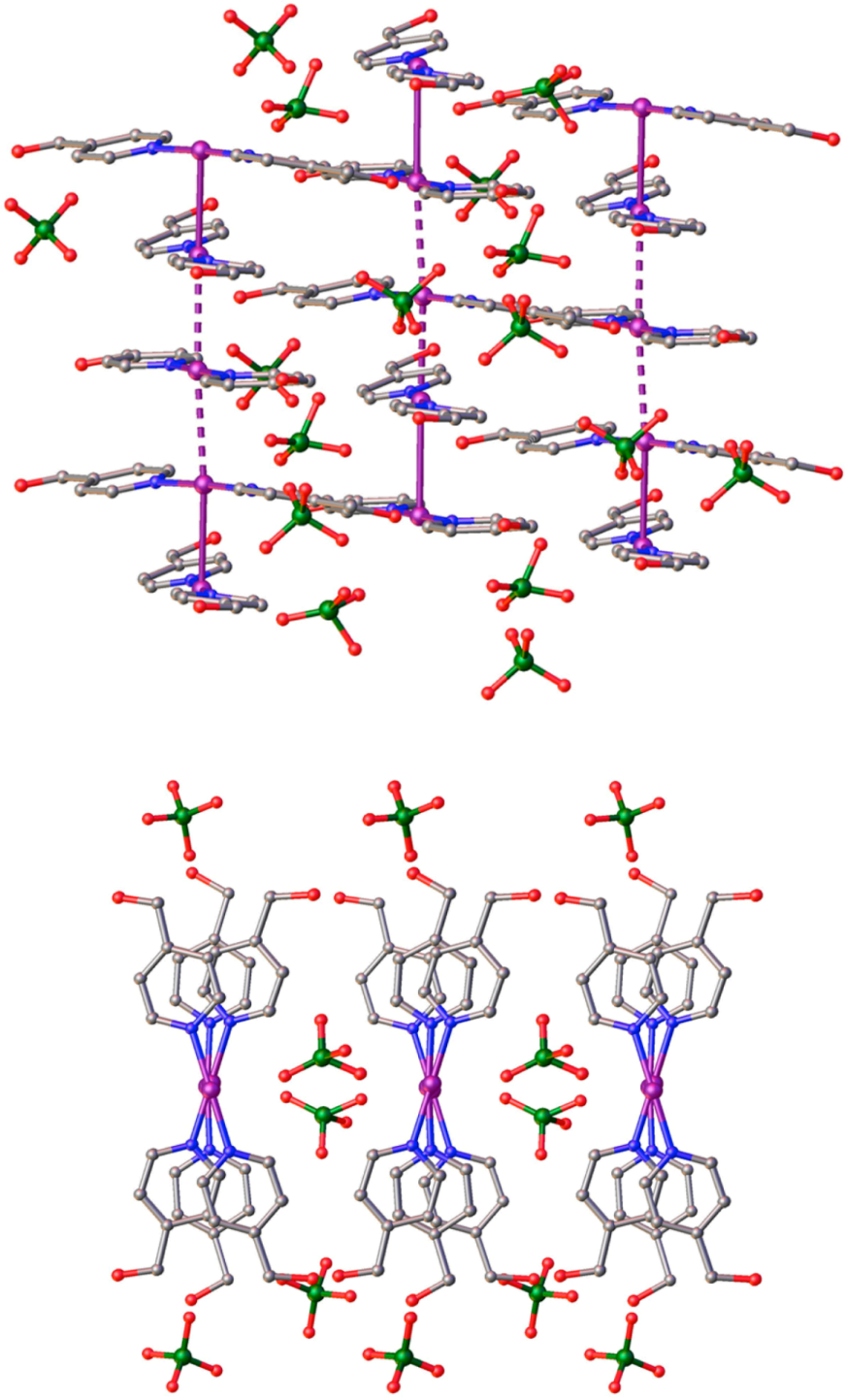

Figure A.4. Crystal structure of complex **4** oriented along **(top)** and down (**bottom**) the *c* axis.

rings through the Ag(I) chain accentuates this feature, and illuminates a weak H-bond network established through the OH groups between adjacent units along the *a*-*b* plan. In contrast, eclipsing ClO_4^- anions down the *c* axis between the stacked silver chains and the terminal alcohol groups of the contiguous Ag1-Ag2-Ag3 units exhibit an extensive bridging network that appears to drive the architecture of the extended structure. Unlike the weak Ag···O(NO_3^-) interactions observed in the structure of **1**, there are eleven distinct Ag···O(ClO_4^-) interactions with distances ranging from 2.706(4) to 3.553(5) Å.

A.1.6 Conclusion

Results of the current work demonstrate that the change in the counter anion from NO_3^- to BF_4^- to $CF_3SO_3^-$ and finally to ClO_4^- give rise to distinct structural topologies capable of imposing argentophilic interactions at Ag(I) centers of simple coordination complex $[Ag(PyOH)_2]^+$. In complex **1**, discrete Ag−Ag dimers along the *c* axis are observed and minimal intermolecular interactions between the ligand appendages of the $[Ag(PyOH)_2]^+$ units are present. Evolution of these discrete units towards an intermediate structure where silver atoms weakly interact in an extended semi-linear fashion was achieved by employing $CF_3SO_3^-$ to give the solid state structure of complex **3**. Complete transformation of the Ag(I) centers towards a stronger linear chain that features argentophilic interactions was finally achieved in structure complex **4**, where the ClO_4^- was selected as the counter anion. The counter ions in these complexes dictate both the architecture of the polymeric structures and the Ag−Ag interactions.

Although the results appear to be related only to the solid phase properties of heterocyclic silver complexes, these findings provide significant insight into synthetic processes that can be manipulated to yield desired heterocyclic silver (I) complexes. In particular, this work stressed the significance of selecting the appropriate starting silver salt. Choice of $AgNO_3$ in the synthesis of complex **1** afforded a robust solid that could be stored in a vacuum desiccator from months, while substitution of this salt for $AgClO_4$ yielded a fragile product that decomposed within hours, even when kept under air free conditions.

A.1.7. Methods

Materials. All chemicals and solvents used were ACS grade. $AgClO_4$ and 4-pyridylcarbinol were purchased from Sigma-Aldrich (St. Louis, MO). All solvents and reagents where dried according to standard procedures. *Because $AgClO_4$ is known to be explosive with excessive mechanical friction care was taken when working with this silver salt.*

Synthesis of $[Ag(PyOH)_2]$ NO_3 (1). A concentrated solution of 4-pyridylcarbinol (270 mg, 0.25 mmol) in dry ethanol was added dropwise to a rapidly stirring solution of $AgNO_3$ (200 mg, 0.12mmol) in 5 mL ethanol for 30 min. The reaction mixture was then heated to ~50° C for 20 min when a white fluffy precipitate began to form. As the solutions was cooled the product continued to form and precipitate out. The solid was collected by vacuum filtration and washed with cold ether. The solid was dried under vacuum for 24 h and then recrystallized by vapor diffusion, performed by

dissolving the solid into dry acetonitrile in scintillation vials (11.8 mg/1 mL acetonitrile) and slowly diffusing diethyl ether into the solutions. After 72 h clear single crystal quality blocks formed. ^{1}H-NMR (500 MHz, dMeCN, ppm): 4.66 (s), 7.41 (s) and 8.49 (s). IR (KBr pellet, cm^{-1}): 619 (s), 656 (s), 770 (s), 1109 (s), 1236 (s), 1385, 1619 (s), 1763 (s), 2392, and 3116.37 (s).

Synthesis of [Ag(PyOH)$_2$]BF$_4$ (2). A concentrated solution of 4-pyridylcarbinol (100 mg, 0.514 mmol) in dry ethanol was added dropwise to a rapidly stirring solution of $AgBF_4$ (115 mg, 1.05 mmol) in 4 mL acetonitrile for 30 min at 40° C. Allowed solution to cool over 30 min and solution remained clear. Solvent was decreased to one-third the original volume under vaco and solution became increasingly viscous until small microscrystals began forming along the walls of the flask. Solution was stored at 4° C overnight and clear single crystal quality cubes formed at the bottom of the flask. ^{1}H-NMR (500 MHz, dMeCN, ppm): 4.66 (s), 7.41 (s) and 8.49 (s). IR (KBr pellet, cm^{-1}): 602 (s), 798 (s), 1058, 1419 (s), and 1608 (s).

Synthesis of [Ag(PyOH)$_2$]OTf (3). A concentrated solution of 4-pyridylcarbinol (85 mg, 0.77 mmol) in dry ethanol was added dropwise to a rapidly stirring solution of AgOTf (100 mg, 0.390 mmol) in 5 mL dichlormethane for 30 min. The solution was then concentrated to one-third the original volume and stored at 4 C overnight, yielding a white solid. The product was collected and washed with cold diethyl ether and then ethanol. Dissolving the solid into dry acetonitrile in a scintillation vial and slowly diffusing diethyl ether afforded single crystal quality clear plates. After 72 h

clear single crystal quality blocks formed. ^{1}H-NMR (500 MHz, dMeCN, ppm): 4.66 (s), 7.41 (s) and 8.49 (s). IR (KBr pellet, cm^{-1}): 519 (s), 649 (s), 1034 (s), 1227, 1420 (s), and 1609 (s).

Synthesis of $[Ag(PyOH)_2]ClO_4$ (4). To a rapidly stirring solution of $AgClO_4$ in acetonitrile (200 mg, 0.888 mmol) a concentrated solution of PyOH (200 mg,1.8 mmol) in ethanol was added dropwise. Clear single-crystal quality needles of $[Ag(PyOH)_2]ClO_4$ were obtained from the reaction solution at 4° C after the solvent was concentrated down to one-half the original volume. ^{1}H-NMR (500 MHz, dMeCN, ppm): 4.66 (s), 7.41 (s) and 8.49 (s). IR (KBr pellet, cm^{-1}): 626 (s), 799 (s), 1005 (s), 1094, 1418 (s), and 1612 (s).

A.1.7.1 Experimental Data: IR and ^{1}H-NMR Spectra

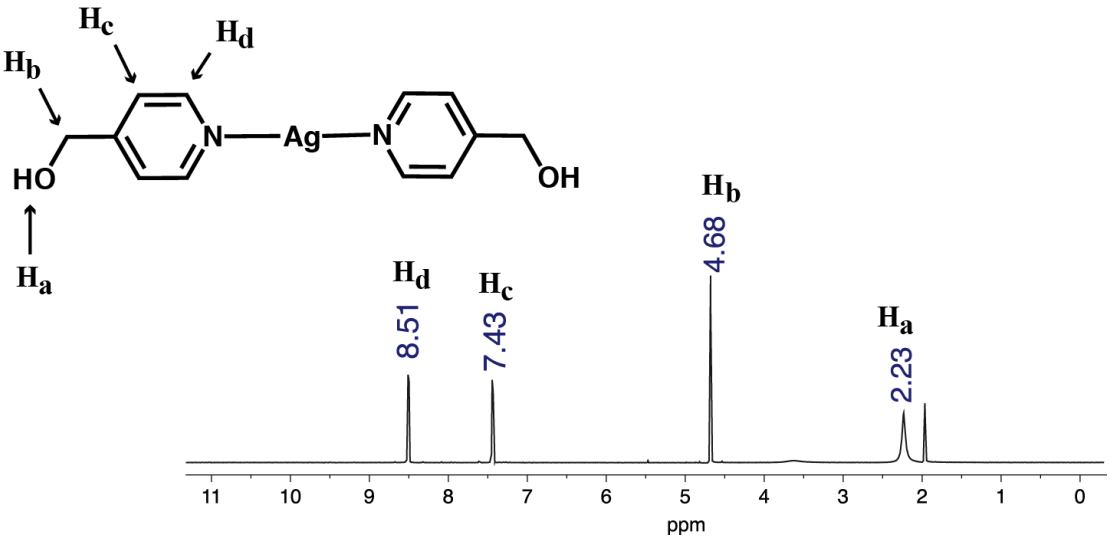

Figure A.5. ^{1}H-NMR (500 MHz) spectrum of $[Ag(PyOH)_2]X$ in CD_3CN.

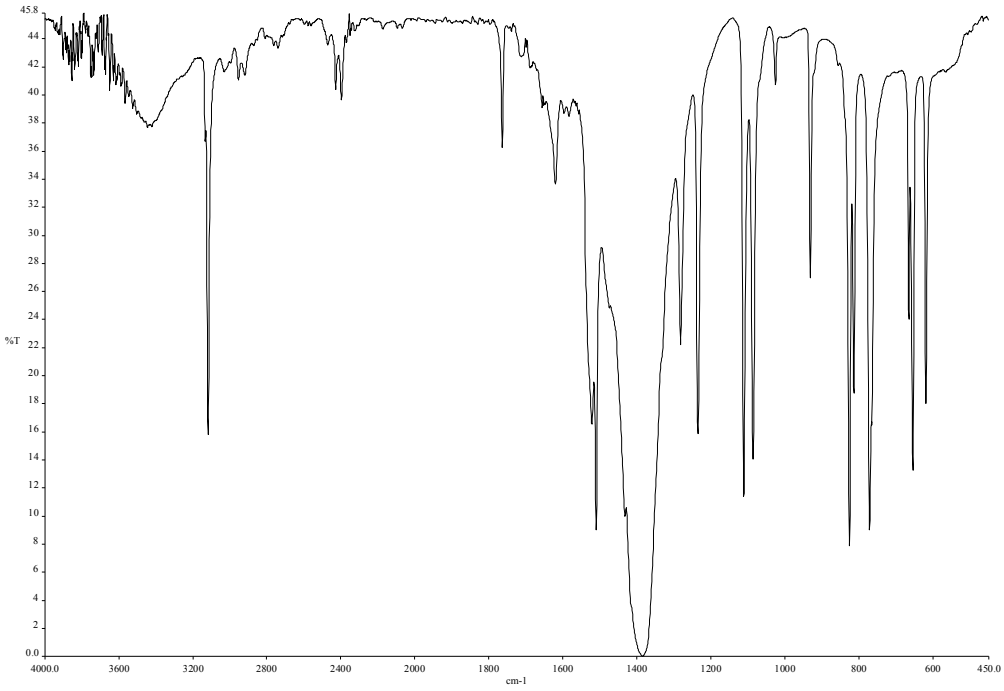

Figure A.6. IR spectrum of $[Ag(PyOH)_2]NO_3$ in KBR matrix.

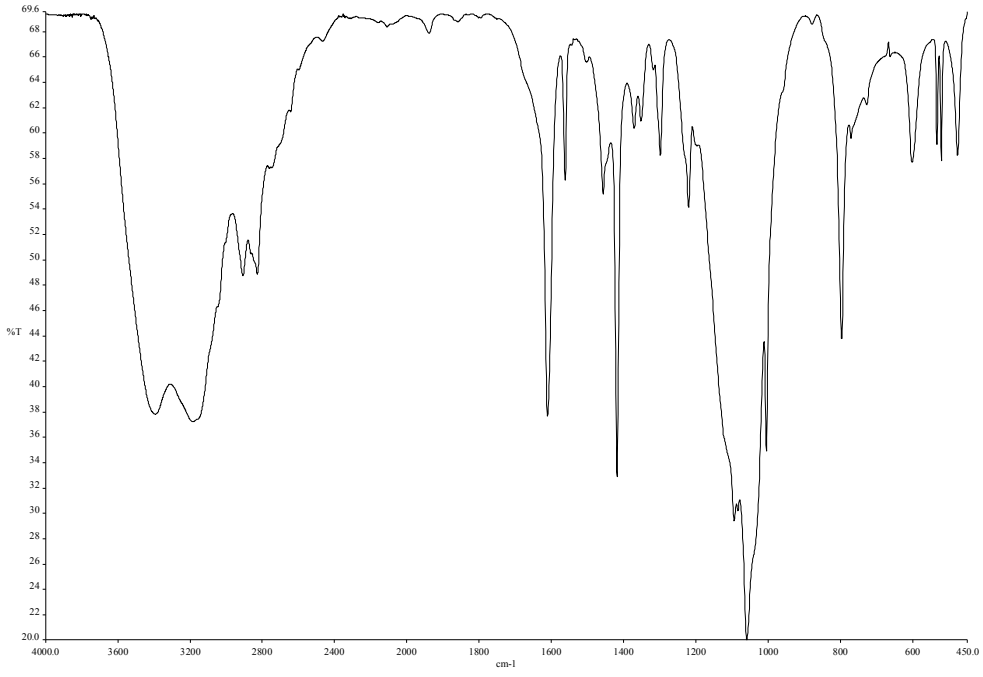

Figure A.7. IR spectrum of $[Ag(PyOH)_2]BF_4$ in KBR matrix

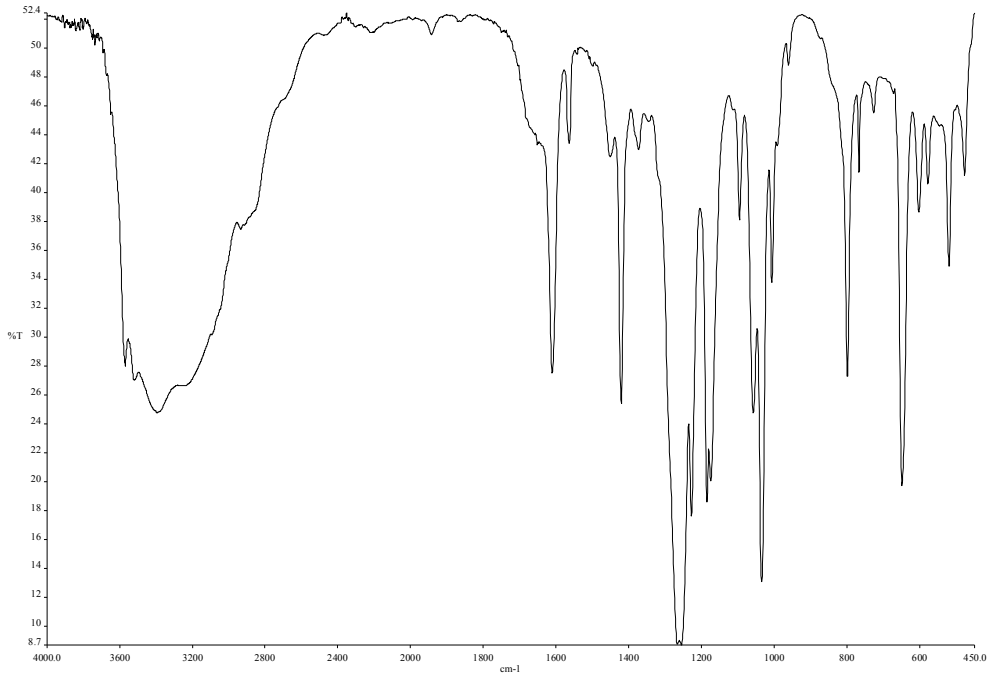

Figure A.8. IR spectrum of $[Ag(PyOH)_2]OTf$ in KBR matrix.

A.1.8 References

1. Halpenny, G.M.; Steinheardt, R.C.; Okialda, K.A.; Mascharak, P.K., *J. Mater. Sci.: Mater. Med.*, **2009**, *20*, 2353-2360.
2. Halpenny, G.M.; Gandhi, K.R; Mascharak, P.K., *ACS Med. Chem. Lett.*, **2010**, *1*, 180-183.
3. Heilman, B.J.; Halpenny, G.M.; Mascharak, P.K., *J. Biomed. Mater. Res. B.* **2011**, *99B*, 328-337.
4. Heilman, B.J.; St. John, J.; Oliver, S.R.J.; Mascharak, P.K., *J. Am. Chem. Soc.*, **2012**, *134*, 11573-11582.
5. Heilman, B.J.; Tadle, A.C.; Pimentel, L.R.; Mascharak, P.K., *Inorg. Biochem.*, **2013**, 123, 18-22.
6. Levy, S.B. and Marshall, B., *Nature Med*., **2004**, *10*, S122-S192.
7. Arias, C.A. and Murray B.E., *N. Engl. J. Med*., **2009**, *360*, 439-443.
8. Chopra, I., *J. Antimicrob. Chemoth.,* **2007**, *59*, 587-590.
9. Marambio-Jones, C. and Hoek, E.M.V., *J. Nanopart. Res.*, **2010**, 12, 1531-1551.
10. Rowan, R.; Tallon, R.; Sheahan, A.M.; Curran, R.; McCann, M.; Kavangh, K.; Devereux, M.; McKee, V., *Polyhedron*, **2006**, *25*, 1771-1778.
11. Abu-Youssef, M.A.M.; Dey, R.; Gohar, Y.; Massoud, A.A.; Öhrström, M.A.; Lander V., *Inorg Chem*., **2007**, *46*, 5893-903.

Appendix B. Synthesis and Construction of Silver(I)-Carboxymethyl Cellulose Dressings Designed for Trackable Therapeutic Release

B.1.1 Background

Silver is a biocide that has been utilized throughout civilization as a broad-spectrum therapeutic and antiseptic option.[1-3] Interestingly, interest in this noble metal plateaued in the late 1930's with the advent of modern-day antibiotics. However, the unfortunate onset of bacterial acquired antibiotic resistance has resulted in the resurgence of silver in therapeutics and in antimicrobial applications.[4,5]

Unlike traditional antibiotics that target selective cellular features or processes,[6] silver imparts cytotoxic effects on bacteria, fungi, and yeast by targeting not one but many pathways critical to cellular survival. The bioactive species is ionized silver (Ag^+) that has been hypothesized to react with reactive thiol groups of critical enzymes and transport proteins, disrupts proton motive forces essential for energy maintenance of a cell, induce reactive oxygen species (ROS) formation, and impede DNA replication.[7] The multipronged action of Ag^+ has allowed for its continued utility in the control and maintenance of bioburden at wound and burn sites. Silver nitrate ($AgNO_3$) has been used for decades as a topical therapy in burn wound care, but unfortunately requires irrigation of wound sites with a 1% $AgNO_3$ solution 12 times daily, a procedure undesirable for patients and health care professionals alike.[3]

To address these shortcomings, silver-impregnated wound dressings have become an attractive option because they offer extended residual therapeutic activity, decreased wound site exposure, and require significantly less frequent manipulation of the wound site.[8] Taken together, these features contribute to the possibility of increasing patient compliance and minimizing wound site exposure to ultimately

shorten the wound healing process. There are numerous silver *carrier* dressings currently on the market, constructed from dense polymeric frames that are designed to maintain optimal wound moisture levels in addition to releasing therapeutic levels of silver.[9] Silver-based therapeutics commonly loaded into carrier wound dressings range from silver nanoparticles (Ag-NP) to free Ag^+. Although incorporation of ionic silver into a carrier material has the potential of affording the highest level of therapeutic capacity, complications arising from its reactivity towards non-specific proteins and electrolytes can result in its rapid consumption and diminished therapeutic efficacy. Nevertheless, the choice and design of the delivery frame of a silver-based wound dressing can be modulated to further optimize the rate of Ag^+ release to the wound sites, a level of control unattainable with silver salt solutions or silver-based creams.

In addition to impeding the bacterial load at open wounds sites, dressings can contribute to the global wound healing process. This dynamic process requires optimal moisture balance for proper re-epithelialization and tissue remodeling (two of the four wound healing stages).[9-11] Low moisture environments commonly give rise to scab formation that inhibits both stages by creating a mechanical barrier that blocks translation of epidermal cells towards the surface and forces them down into deeper layers of the tissue, extending healing times and giving rise to abnormal tissue architecture and scarring.[12] Hydrocolloid materials are one such example of occlusive dressings that are capable of absorbing wound exudate and maintaining wound moisture. Cellulose-based polymers represent a large class of hydrocolloid dressings

that display effective swelling properties easily modulated with chemical derivatization. For example, incorporation of an anionic group into the cellulose frame significantly increases the hydration capacity of the polymer and introduces anionic sites available for electrostatic interactions with cationic therapeutics. Although it was initially believed that occlusive dressings could inhibit oxygenation and facilitate bacterial growth at wound sites contradictory results were shown by Winter in the 1960's when he showed decreased healing times with application of occlusive dressings to non-ischemic wounds.[13] Application of hydrocolloid-based dressings not only provides optimal level of wound moisture, but also contributes to improved patient comfort because as moisture penetrates the dressing, the surface becomes gelatinous and minimizes resistance during cleaning and replacement of expended dressings.

The potential of occlusive silver-loaded wound dressings in the management of wound healing and infection is evident given the exponential growth in the number of publications highlighting the design of silver-based therapeutics and wound dressings over the last decade. Still, the vast majority of silver-loaded wound dressings available on the market incorporate traditional silver sources $AgNO_3$ and Ag-SD or Ag-NP's.[14] Based on our expertise in the design of trackable therapeutics and drug-carrier materials we synthesized a silver complex-loaded wound dressing that displays a unique *trackable* drug delivery modality by incorporating a blue-green fluorescent silver (I) complex $[Ag(ImD)_2]ClO_4$ (Ag(ImD), λ_{em} = 600 nm) into a carboxymethyl cellulose (CMC) frame. The luminescent properties of the silver

complex also allowed for quantitative determination of Ag(ImD) release rates from the hydrocolloid pad by both fluorescence and electronic absorptions spectroscopy. Further, the effective delivery of Ag(ImD) from the occlusive dressing to a wound site was qualitatively established in solid-phase leaching studies, where movement of Ag(ImD) out the CMC frame onto an agar surface was visually tracked using a hand-held ultraviolet (UV) wand. The findings discussed bellow demonstrate the potential of silver (I) complexes as tunable components of silver-loaded wound dressings that can be tailored to impart trackable release of silver therapeutics to wound sites.

B.1.2 Synthesis and Characterization of Silver (I) Complex $[Ag(ImD)_2]ClO_4$

In attempts to design a trackable silver (I) complex fluorescent highly fluorescent dansyl chloride-dye derivative imidazole dansyl (Im-Dansyl) was employed. The ligand structure was carefully selected and can be divided into to critical units. The first is the *silver-coordinating imidazole group* that was selected based extensive literature support establishing silver (I) imidazole complexes as effective antibacterial therapeutics. The complex effectively increase the bioavailability of Ag^+ leading to enhanced bactericidal action.[15,16] The second, the fluorescent dansyl group is commonly used as a protein tag and reacts with a wide variety of functional groups, including the imidazole group of histidine residues.[17] This fluorophore lacks antibacterial features and acts solely as a visible maker of Ag^+ movement.

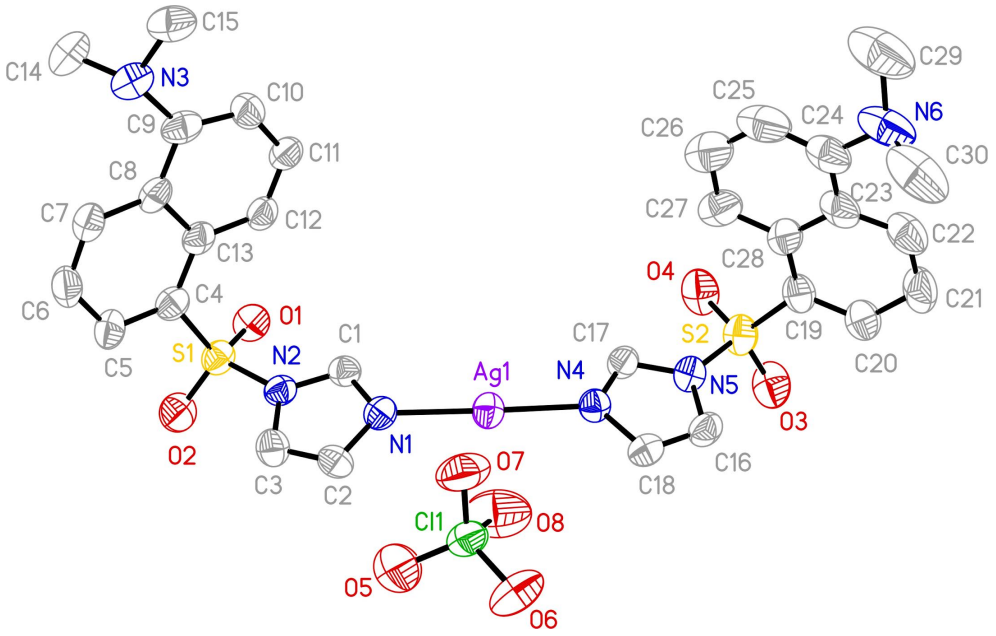

Figure B.1. ORTEP of $[Ag(ImD)_2]ClO_4$

Addition of 2 equivalents of argentophilic ligand Im-Dansyl to a rapidly stiring solution of $AgClO_4$ afforded a classic cationic silver (I) complex $[Ag(ImD)_2]ClO_4$ (Ag(ImD)) which is significantly more water soluble than free Im-Dansyl or $AgClO_4$ (Figure A2.1). Single crystal X-ray diffraction analysis revealed a classic linear silver structure (N-Ag-N, 172.3°) with the silver center caged between two ligand appendages through the imidazole moiety of Im-Dansyl (Figure A2.1). The complex is relatively symmetric (Ag-N1 and Ag-N4 bond lengths of 2.120 and 2.109 Å, respectively) with the imidazole rings of the coordinating ligands lying within a single plane.

The stacked ^{1}H-NMR in Figure A2.2 highlights noteworthy peak additions and shifts utilized throughout the synthetic process to ultimately corroborate the

crystallographic data and confirm Ag(ImD) synthesis. In the top panel of the figure a standard ^{1}H-NMR of dansyl chloride is shown. Derivatization of the Dansyl chloride with an imidazole group at the sulfonyl chloride end was confirmed in the ^{1}H-NMR spectra shown in the middle panel, with the addition of three new singlet peaks at 8.11, 7.31, and 7.03 ppm corresponding to the three protons of the imidazole ring and a global upfield shift of the all peaks corresponding to the aromatic protons of the naphthalene moiety of Dansyl chloride. Finally, the bottom panel highlights ligation of Im-Dansyl to the silver center to form Ag(ImD) with the significant shifts in peaks 8.11, 7.31, and 7.03 ppm (Imidazole H's) to 8.41, 7.18, and 7.00 ppm, respectively.

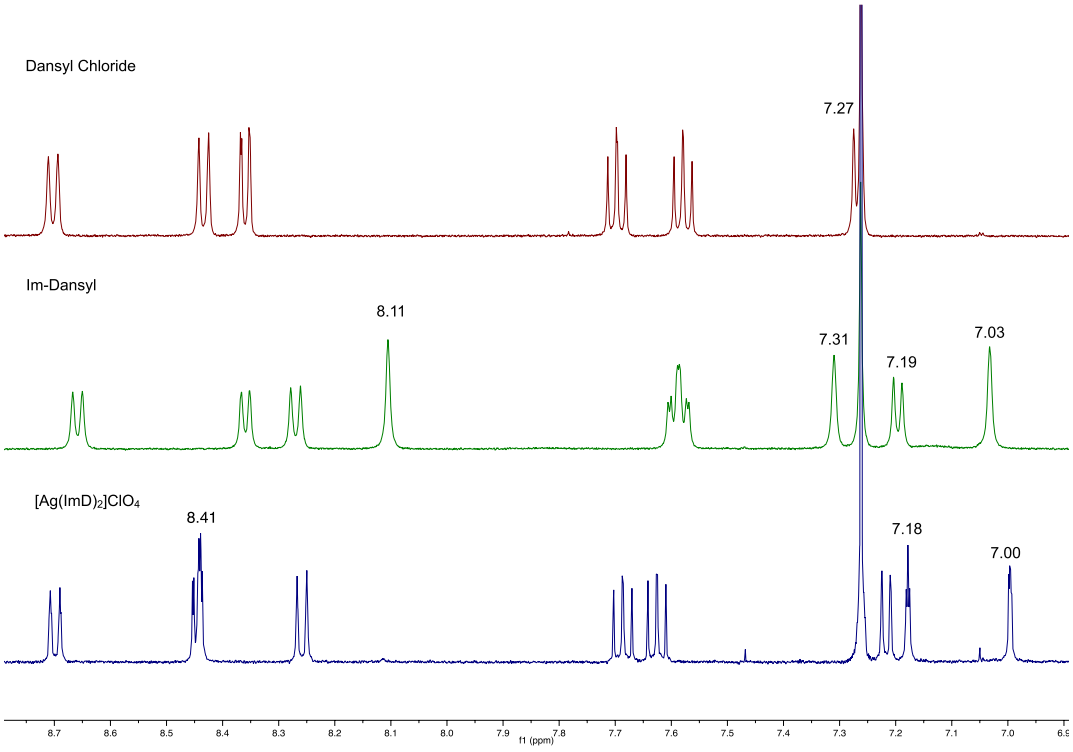

Figure B.2. Stacked ^{1}H-NMR ($CDCl_3$) spectra of Dansyl chloride (top panel), Im-Dansyl (middle panel), and $[Ag(ImD)_2]ClO_4$ (bottom panel).

Interestingly, electronic absorption spectroscopy measurement of Ag(ImD) showed no significant change in the absorption profile compared to the absorption spectrum of free ligand Im-Dansyl, with the λ_{max} (maximum absorption band) at 360 nm (Figure A.2.3). However the extinction coefficient value at this wavelength increased from 2020 $M^{-1}cm^{-1}$ to 7735 $M^{-1}cm^{-1}$ upon ligation. Because each Ag(ImD) molecules is decorated with two dye molecules around the silver center one may predict an approximate doubling in the molar absorptivity, however an ~4-fold increase was instead observed suggesting electronic interactions between the filled d-orbitals of the silver center and perhaps the π-orbitals of the ligand appendage. Minimal changes in the fluorescence excitation and emission profiles were also observed between the metal complex and its free ligand, displaying only a small bathochromic shift in the emission band upon excitation at 360 nm from 480 to 500 nm (Figure B.3).

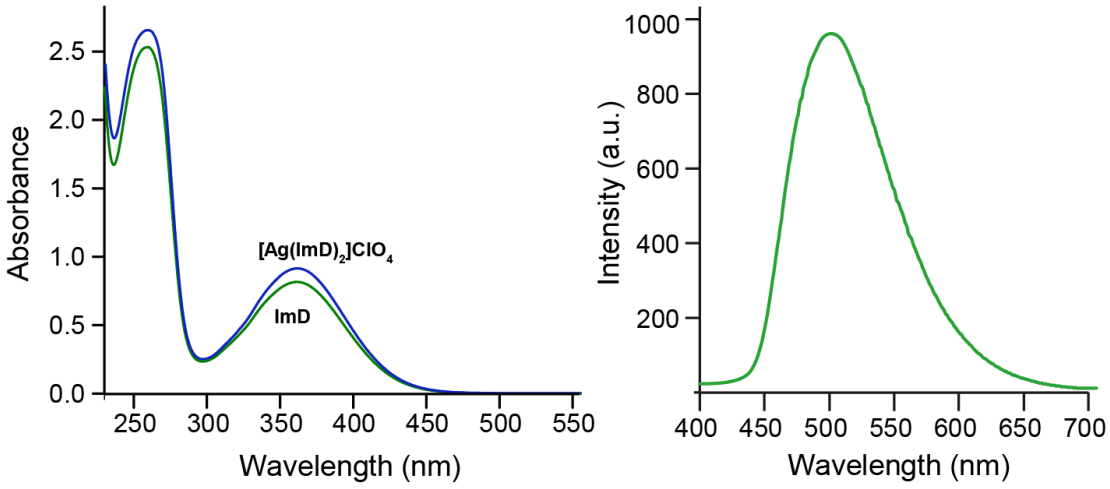

Figure B.3. Electronic absorption spectrum of free Im-Dansyl and Ag(ImD) (left) and emission spectra of Ag(ImD).

Photostability experiments completed using ^{1}H NMR showed no apparent decomposition of Ag(ImD) upon continuous exposure to ambient light for 24 h. In comparison, a purple-brown solid began forming in the standard $AgNO_3$ sample after only 1 h of equivalent light exposure. Further, the additional stability experiment performed in minimal recovery diluent (MRD) confirmed the stability of Ag(ImD) in biological media because no evident change in the profile of the 500 nm excitation band (indicative of deligation) was observed over 24 h. Interestingly, thermal stability experiments performed by ^{1}H-NMR, where a sample of $[Ag(ImD)_2]ClO_4$ in deuterated acetonitrile (CD_3CN) was incubated at 37° C for 24 h, showed a resultant spectrum indicative of complete deligation of ImD (Figure A2.4).

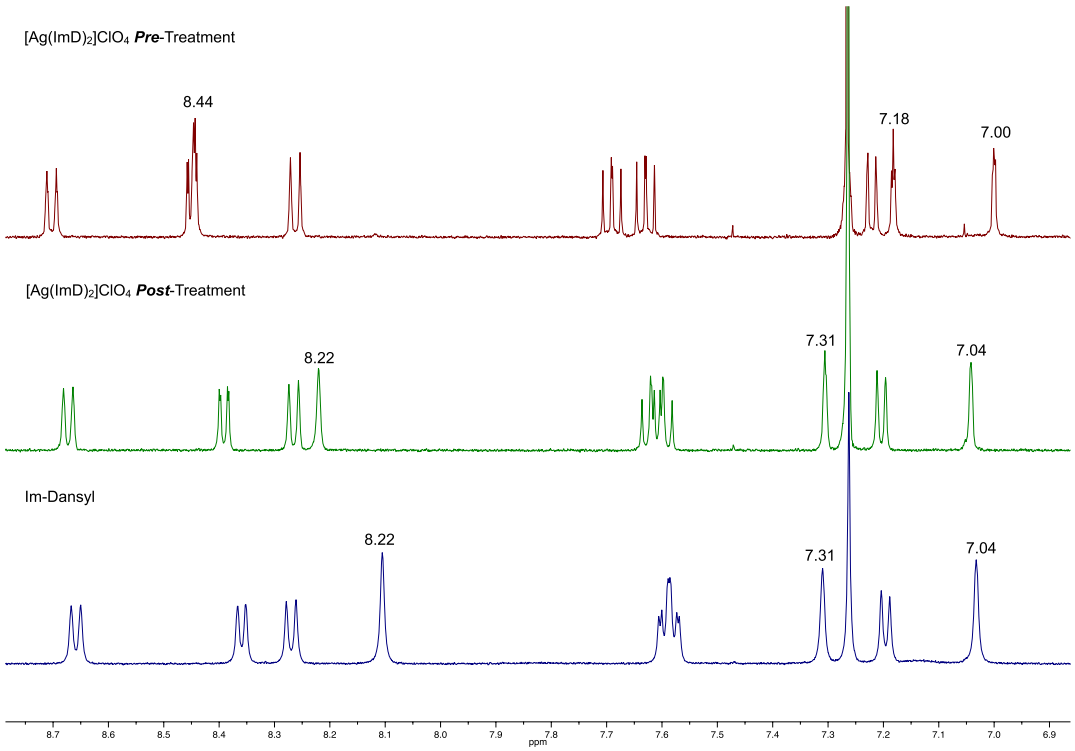

Figure B.4. ^{1}H-NMR spectrum of $[Ag(ImD)_2]ClO_4$ after 24 h incubation in CD_3CN at 37° C.

B.1.3 Synthesis and Characterization of Silver (I) Complex $[Ag(ImD)_2]NO_3$

Given our established knowledge regarding the role that counter ions in the synthesis of hetercyclic silver (I) complexes the nitrate analogue of $[Ag(ImD)_2(ClO_4)]$ was also synthesized. Substitution of the starting silver perchlorate salt for silver nitrate afforded neutral silver complex $[Ag(ImD)_2(NO_3)]$, where the nitrated anion was observed to coordinate to the silver center by crystallographic analysis (Ag-$O_{Nitrate}$ 2.553(3) Å). The tri-cooridnate complex fashions a *quasi*-trigonal planar geometry, but is slightly puckered with N(4)−Ag−N(1), N(4)−Ag−O(7), and N(1)−Ag−O(7) angles of 155.14(9)°, 119.78(10) °, and 85.07(10)° respectively (Figure A2.5). While this Ag-ImD analogue was not suitable for further studies given the choice of a anionic sodium carboxymethy cellulose carrier frame, this complex could be utilized in future studies.

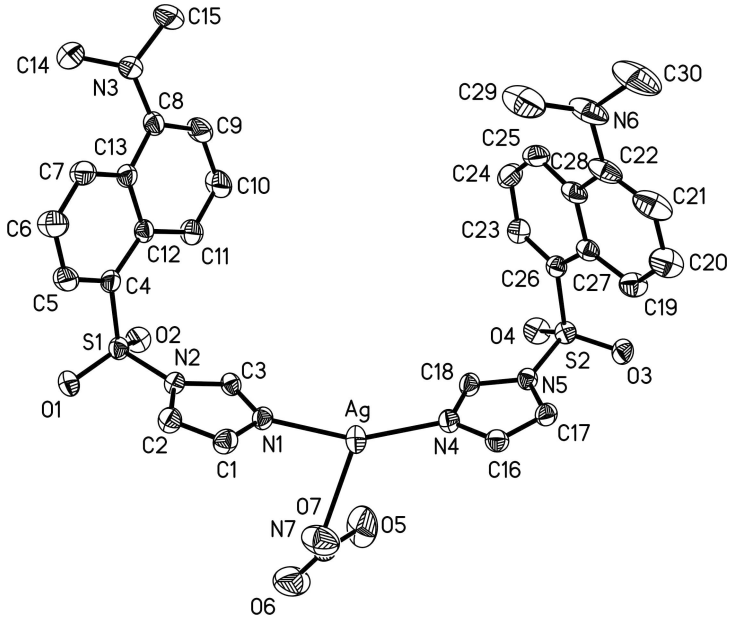

Figure B.5. ORTEP of $[Ag(ImD)_2(NO_3)]$

B.1.4 Preparation and Characterization of $Ag(ImD)_{CMC}$ Wound Dressing

Ag(ImD)-loaded carboxymethyl cellulose pads were synthesized by a *one-pot* synthesis, where a homogenous gel of NaCMC, PEG, Ag(ImD) and water is poured into a sterile culturing dish and dried to a desired consistency. The final $Ag(ImD)_{CMC}$ pad exhibits a rubber-like texture that is rigid enough to be easily cut into any desired shape but slowly gels with the addition of water, a feature characteristic of hydrocolloid polymers. The carboxymethyl cellulose frame was selected because it is a common wound dressing component that facilitates desloughing process at the wound bed (desloughing agent), assist in maintaining optimal wound moisture, and contains available anionic sites for electrostatic loading of the Ag(ImD) cationic complex.[12,18,19] It should be noted that PEG was incorporated into the dressing to help

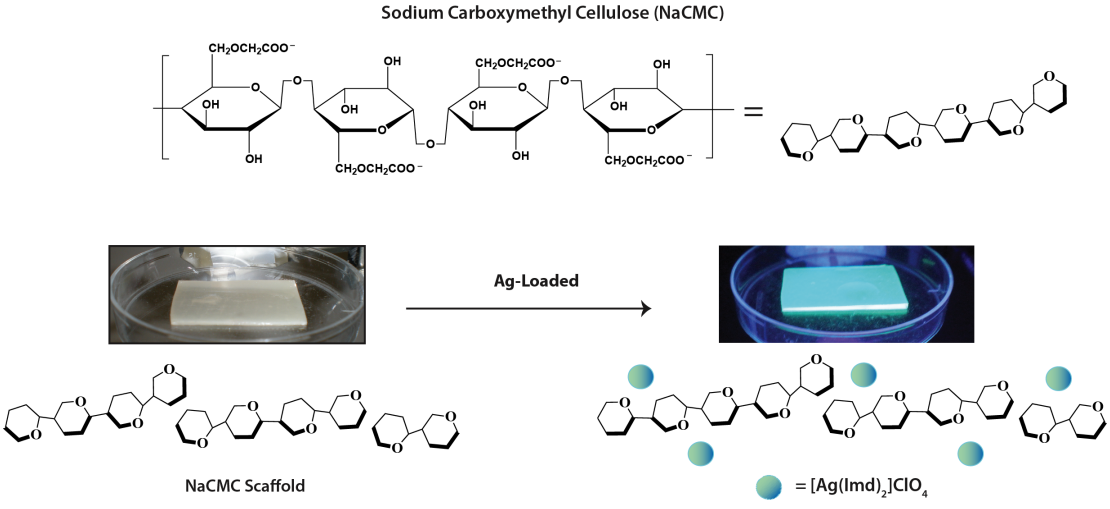

Figure B.6. Schematic representation of loaded and unloaded carboxymethyl-cellulose (CMC) pads. The left image represents an unloaded non-fluorescent CMC pad and the right a loaded $Ag(ImD)_{CMC}$ pad.

solubilize NaCMC into the water media. PEG is bioinert and poses no apparent bactericidal action and for this reason can be considered an auxiliary component within the $Ag(ImD)_{CMC}$ pad.[20]

Release of Ag(ImD) from pre-fabricated pre-weighed hydrocolloid gel disc pads into MRD solutions was monitored by fluorescence and absorption spectroscopy. Analysis of the release profile collected over 24 h highlights an initial lag period in the first 8 h where the rate of release is relatively slow. However, after 8 h a linear release of Ag(ImD) begins with a slope equating to leaching rate of 0.0027 ± 0.00045 μg/min. The average Ag(ImD)CMC pad of 1 cm diameter is 75.6 mg, which equates to 64 μg Ag(ImD). Based on this rate of release it can be calculated that under the defined experimental conditions 5.2 μg of Ag(ImD) are released over 24 h of incubation. Interestingly, decrease in the loading of Ag(ImD) from 1 % to 0.5 % results in a decrease in the lag interval of Ag(ImD) release from approximately 8 h to 3 h with a leaching rate of 0.0068 ± 0.00012 μg/min. The increased rate of leaching with decreased Ag(ImD) loading can likely be attributed to variances in the Donnan potential of the systems.[21] While this property has more commonly been applied to explain movement across an impermeable membrane that separates liquid media with differing ionic species and net ion concentrations, it is applicable to hydrocolloid materials and ionic liquids that can act as phase boundaries impeding or controlling ion movement. Because cationic Ag(ImD) interacts directly with the anionic carboxymethyl groups of the hydrocolloid frame essentially resists change and movement of external ions into the network with higher loading. In comparison the

0.5 % Ag(ImD)-loaded gel reach a dynamic state of ion movement much more quickly, as cationic species present in higher concentrations (relative to Ag(ImD) in the MRD solution move into the hydrocolloid frame and replace the cationic silver complex driving its movement out of the polymer network.

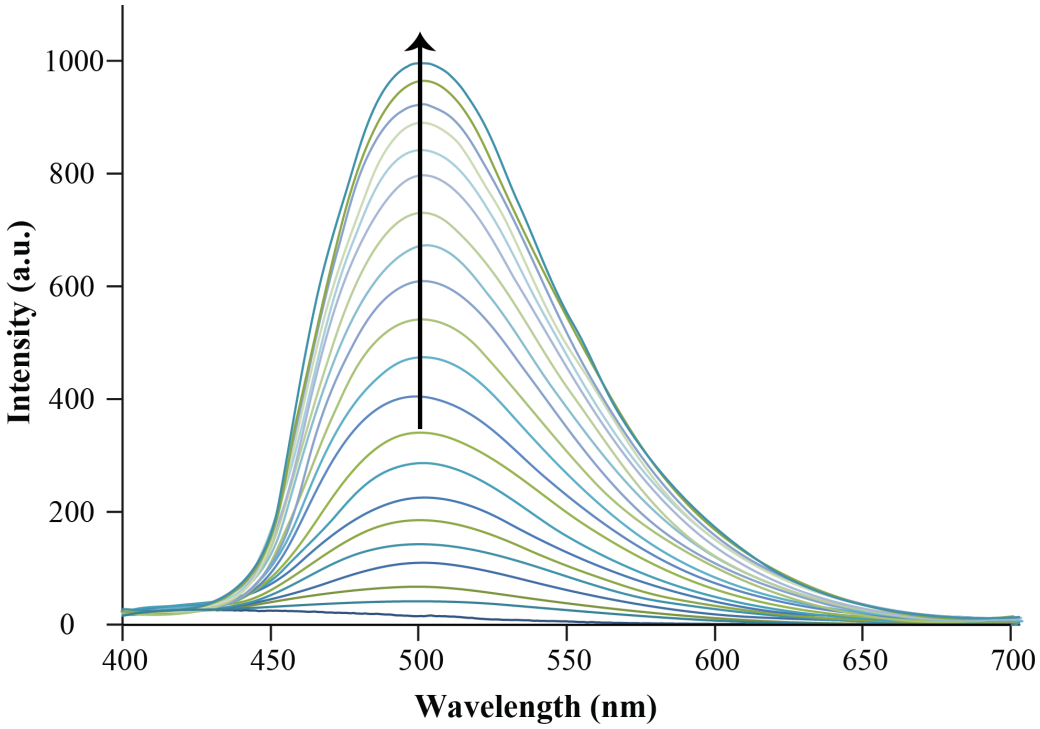

Figure B.7. Fluorescence spectra collected over 24 h, where $Ag(ImD)_{CMC}$ was incubated in MRD. Each curve represents a time point over the 24 h period. The linear increase corresponds to a linear release rate of Ag(ImD) from the carboxymethyl cellulose wound dressing frame.

Qualitative leaching studies conducted to observe the release of Ag(ImD) from $Ag(ImD)_{CMC}$ disc onto an agar surface revealed a visual movement of Ag(ImD) out of the hydrocolloid frame within the first 2 h of incubation, and a visually linear increase in fluorescence intensity at the agar surface with time. Careful examination of the

incubated agar plates showed that Ag(ImD) did not only move out of the CMC frame to the surface of the agar, but actually traversed laterally down into the agar matrix. Taken together these findings establish the tunability of therapeutic release from the designed $Ag(ImD)_{CMC}$ pad, where leaching rates and loading dosages for defined time intervals. *Such a feature could introduce the possibility of creating a wide spectrum of therapeutic dressings with leaching profiles tailored to control various levels and types of bioburden at wound sites.*

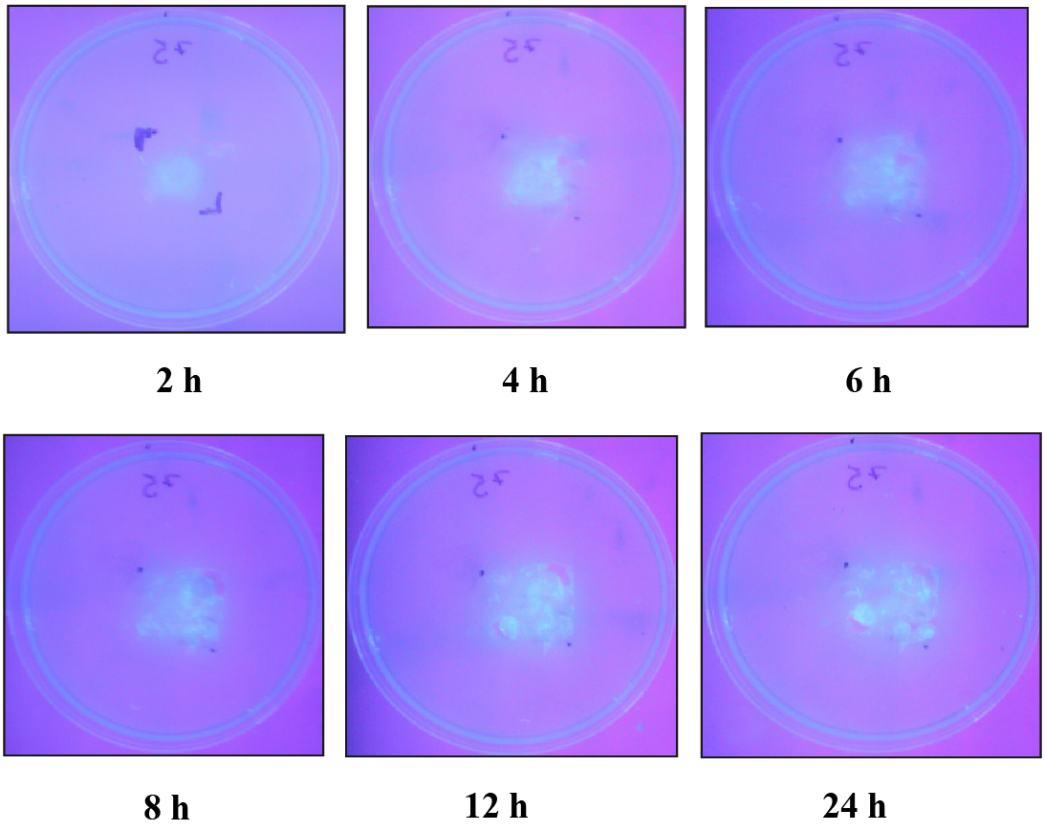

Figure B.8. Results from the qualitative leaching studies performed by applying a $Ag(ImD)_{CMC}$ pad onto a 5% agar plate surface and soaking with 100μL MDR. Moving from the top panel to the bottom panel, images collected over a 24 h incubation period are shown.

A final prototype was prepared be combining a 1 cm circular $Ag(ImD)_{CMC}$ disc pad, 1.5 cm sterile ultra-soft latex-free gauze square, and a 1.5 cm rayon-based Durapore ™ surgical tape square (Figure A2.6) $Ag(ImD)_{CMC}$ discs were first placed onto a pre-cut gauze surface and then the paired surgical tape piece was gently placed on top of the gel pad. Applying gentle pressure to the edges of the adhesive tape secured the layers together. All $Ag(ImD)_{CMC}$ discs were weighed prior to being incorporated into the dressing construct. The average disc weight was determined to be 75.6 mg and only discs weighing within the standard deviation were used.

Figure B.9. Prototype of the Ag(ImD)-loaded wound dressing.

B.1.5 Defining the Antibacterial Capacity of Ag(ImD) and the Ag(ImD)-loaded wound dressing

To establish the potential therapeutic capacity of Ag(ImD) minimal inhibitory concentration (MIC) experiments were completed against gram-positive and gram-negative bacterial strains commonly known to inoculate wound sites *E. Coli* (gram-negative) and *S. Aureus* (gram-positive).[3] After performing the MIC assay against the

respective strains in succession with corresponding controls it was established that Ag(ImD) displays an MIC of 2.3μg/mL and 4.7 μg/mL against *E. Coli* and *S. Aureus* respectively. The observed MIC values are very much comparable to those reported for similar silver (I) complexes[15,22,23] and display significantly enhanced antibacterial capacity compared to many silver colloid and Ag-NP options.[24,25] Enhanced efficacy of Ag(ImD) against the gram-negative strain is commonly observed in silver (I) complexes and has been hypothesized to be a function of the cell structure of the bacterium that features a thinner peptidoglycan layer of the cell wall in comparison to gram-positive strains.

Finally, bacterial experiments where performed using the prototype Ag(imD)-loaded wound dressing prototypes discussed above (1 cm diameter $Ag(ImD)_{CMC}$ gel disc between 2cm diameter Durapore™ tape and gauze squares, Figure A2.9) and applied to a skin and soft tissue infection (SSTI) model inoculated with *E. Coli*, which was shown to be more susceptible to Ag(ImD) based on the calculated MIC values. Incubation of the prototype dressing on the surface of the SSTI agar plate resulted in a bacterial clearance that overlays with the visible fluorescence demarcation indicating Ag(ImD) loading (Figure A2.10). These results confirm the potential of the designed Ag(ImD)-loaded hydrocolloid-based dressing to utilized as a trackable drug-delivery system. The ability to visually and spectrophotometrically monitor therapeutic release can be exploited to optimize rates of silver release from silver-based dressings and offer a level of detection for healthcare workers to visually observe therapeutic loading to a wound site and identify exhaustion of a dressing.

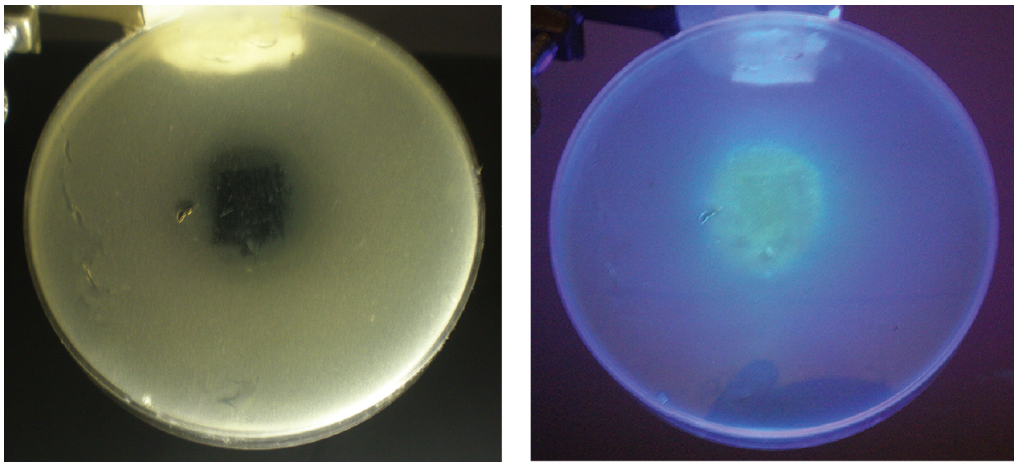

Figure B.10. SSTI agar plate observed after exposure to a Ag(ImD)-dressing prototype. The image on the left highlights bacterial clearance that overlays with the loading of fluorescent Ag(ImD) shown on the right.

B.1.6 Conclusion

Silver-based therapeutics have long been utilized as antiseptic options given the oligodynamic effect of ionized silver. Resurgence in the use of this noble metal as an antibacterial agent is fierce given the rapid onset of bacterial resistance towards traditional antibiotics. The application of topical silver agents and silver-loaded wound dressings in the control of bioburden at burn sites has been widely accepted, however progress in the mode of delivery and sources of silver have remained limited. The current work highlights the synthesis of silver(I) complex $[Ag(ImD)_2]ClO_4$ that affords two levels of therapeutic improvement with the ligation of the fluorescent ImD group to a Ag^+ center. The first level is through the effective caging bioactive Ag^+ that yields significantly lower MIC values against gram-positive and gram-negative bacteria compared to many Ag-NP-based drugs reported

previously. The second level introduces a unique feature of *therapeutic trackability* where release of fluorescent Ag(ImD) from a carboxymethyl cellulose-based hydrocolloid carrier can be visualized by simply shining a UV source over the site of delivery (such as a handheld UV wand). Given the diverse chemistry of silver, the options for future ligand design are expansive. The synthesis of silver complexes is just one contributing factor that can then be incorporated into a vast number of polymer frames to ultimately create "tunable" wound dressing collections.

B.1.7 Methods

Synthesis of $[Ag(ImD)_2]ClO_4$. The silver (I) complex was prepared after a concentrated solution of imidazole dansyl (ImD, 130 mg, 200 mmol) in dry acetonitrile (ACN) was added drop wise to a rapidly stirring solution of silver (I) perchlorate (27 mg, 100 mmol, $AgClO_4$) and allowed to stir for 3 h. A Deep orange microcrystalline solid formed after the reaction solution was concentrated to one-half the original volume and stored at 4° C for 24 h. The silver salt was recrystallized using a vapor diffusion crystallization method. The crude solid was dissolved in dry acetonitrile then kept under the vapor pressure of ether at 4° C, and orange single crystal qualities needles formed after 72 hours. ^{1}H NMR (Varian Unity, 500 MHz): 10.33 (d), 10.04 (d), 9.91 (d), 9.76 (s), 9.28 (m), 8.99 (s), 8.88 (d), 8.67 (s), 4.54 (s). IR (KBr disk): 786 cm^{-1} (s), 636 cm^{-1}, 1092 cm^{-1}, 1375 cm^{-1}, and 1462 $cm^{-}1$. Electronic spectroscopy (Carey 5000): λ_{max} = 360 nm (ε = 7735 $M^{-1}cm^{-1}$).

$Ag(ImD)_2]ClO_4$ photostability and biocompatibility assay. A silver complex solution was prepared by dissolving 10 mg Ag(ImD) into 700 mL deuterated acetonitrile (dMeCN). An initial ^1H NMR spectrum was acquired and defined as time 0 and then the sample was properly sealed to minimize solvent evaporation and left in ambient light. Subsequent ^1H NMR acquisitions were then collected at 8 h, 12 h and 24 h. Exposure intervals are defined strictly as the time of light exposure and do not include acquisition time. For qualitative comparison a $AgNO_3$ solution was also prepared by adding 5 mg $AgNO_3$ to 700 mL dMeCN. The sample was sealed and set directly adjacent to the Ag(ImD) solution under ambient light for equivalent time exposure. A secondary stability experiment was also performed where the a standard solution of Ag(ImD) was prepared in minimal recovery diluent (MRD) to establish the compatibility of the silver complex in biological media. Stability of the complex was determined by monitoring the emission band at 500 nm (in Varian Cary Eclipse fluorimeter) for 24 h.

Preparation of Ag(ImD)-loaded CMC gel pad. The silver-loaded hydrocolloid was prepared by adding 0.525 g of NaCMC (3.5 % w/v) and 0.750 g 2000 MW polyethylene glycol (PEG, 5% w/v) into a 50 mL beaker. To this mixture 13.5 g deionized MilliQ water were added dropwise. The slurry was allowed to stir until the solid was completely dissolved into the water and then a solution of Ag(ImD) (5 mg, in 0.954 mL ACN) was added dropwise under mild stirring. The final solution was transferred into a sterile culturing dish (60 mm), weighed, and placed into a desiccator to dry. Each pad was dried to 30 ± 1% its original weight (70 % solvent

loss by weight, q) to assure uniformity from batch to batch, calculated by the following equation: $q = \frac{(initial\ Ag(ImD)CMC\ gel\ weight\ (Wi) - dried\ Ag(ImD)CMC\ weight)}{Wi}$

Characterization of Ag(ImD) release from $Ag(ImD)_{CMC}$ pad into aqueous media. Because the designed silver salt Ag(ImD) displays absorption and fluorescent profiles, rate of its release from $Ag(ImD)_{CMC}$ pads was quantifiable by absorbance (Carey 5000) and fluorescence spectroscopy. Maximum recovery diluent (MRD, 1 g/L Peptone, 8.5 g NaCl, 0.01 M Phosphate buffer, pH 7.0) was selected as the solvent for all studies in attempts to provide milieu similar to media required for antibacterial studies, excluding biological molecules that characteristically absorb light and would complicate the spectroscopy studies. In each study pre-weighed circular $Ag(ImD)_{CMC}$ discs (1 cm diameter) were added to quartz cuvettes (10 mm Starna cuvette) containing 3mL MRD. In both absorption and fluorescence spectroscopy studies the cuvettes were kept stationary in the respective sample holders and spectral readings were taken every 20 min for 24 h. The leaching profile of $Ag(ImD)_{CMC}$ was established by converting the observed change in absorbance at 360 nm ($\varepsilon = 7735\ M^{-1}cm^{-1}$) to concentration by Beer's Law and plotting these values against the corresponding time. Leaching of Ag(ImD) from the hydrocolloid pad was also qualitatively observed by fluorescence spectroscopy.

Characterization of Ag(ImD) release from $Ag(ImD)_{CMC}$ pad onto agar surface. Agar plates (5 % Agar) were prepared in 100 mm culturing dishes, and to each plate 3 pre-weighed $Ag(ImD)_{CMC}$ discs (1 cm diameter) were placed into the agar surface.

MRD was added to the discs to initiate gelation of the disc and facilitate movement of Ag(ImD) out of the carboxymethyl cellulose frame. These plates were kept stationary and allowed to incubate for 24 h. The translocation of Ag(ImD) from $Ag(ImD)_{CMC}$ discs was visually evaluated at 2, 4, 6, 8, 12, and 24 h time points using a UV table top lamp (UVP® UV transilluminator, broad range 200-325 nm). At each time point, dressings were removed and the relative luminescence of the agar surface was noted photographically. In addition to the 1 % $Ag(ImD)_{CMC}$ pads, the same studies were conducted with 0.5 % $Ag(ImD)_{CMC}$ to probe changes in the rate of Ag(ImD) leaching from the hydrocolloid gel pad as a function of therapeutic loading.

Minimal Inhibitory Concentration (MIC) Assay. Gram-positive and gram-negative bacterial strains *E. coli* and *S. Aureus*, respectively, were grown up to 1.0 x 10^8 CFU mL from single colony growths in Müller-Hinton broth at 37° C. Thirty microliters of the stock solutions were then added to sterile round bottom culturing tubes (14 mL) to reach a final CFU of 1.0 x 10^6 in 3 mL total volume. Varied volumes of stock $[Ag(ImD)_2]ClO_4$ (15% ACN) and $AgNO_3$ solutions (10 mg/mL) were added to the prepared bacterial suspensions to achieve 0 μg/mL, 8 μg/mL, 4 μg/mL, 2 μg/mL silver concentrations. $AgNO_3$ solutions were kept in the dark to prevent photodegradation. The final suspensions were incubated at 37° C in a rotary mixer (40 rpm) for 18 h. Final sample suspensions were visually analyzed for bacterial growth and compared to control and standard suspensions.

Antibacterial assay. Effective therapeutic capacity of the Ag(ImD)-loaded occlusive wound dressing was studied using a skin and soft tissue infection (SSTI) model inoculated with *E. coli*, reported previously.[26] In short, 15mL of a 5% agar culturing solution was first plated into a 100 mm sterile culturing plate. To the solidified agar surface 10 mL of a 0.5 % agar solution inoculated with E. coli (final CFU 1.0 x 10^6 mL^{-1}) was added to form the *soft*, top layer. The final plates where then incubated at 37° C for 3 h to allow the top layer to slowly cool and solidify. After this incubation period the prepared wound dressings were applied to the soft agar surface and allowed to incubate for 21 h. Plates were then removed and compared to control samples that contained unloaded wound dressings. Leaching of Ag(ImD) out of the silver-loaded wound dressing was observable by placing SSTI plates on a UV table lamp at the end of therapeutic exposure.

Bacterial cell culture. Strains of *E. coli* ATCC® 25922™ and *S. Aureus* ATCC® 25923™ were employed in bacterial studies. Bacterial inoculants were taken from freeze-dried cultures and grown on Müller-Hinton agar surfaces and incubated for 24 h at 37° C. From these plates single colony growths were taken to prepare standard bacterial suspensions. Müller-Hinton broth solutions (5 mL) were inoculated with single colonies in 16 mm round bottom culturing tubes and incubated for 6 h at 37° C in a rotary mixer (40 rpm) to an OD_{600} between 0.6 and 0.9. From the standard suspensions stock cultures were prepared to 1.0 x 10^8 CFU/mL that were then incorporated into MIC or SSTI assays as described above.

B.1.7.1 Experimental Results: IR Spectra

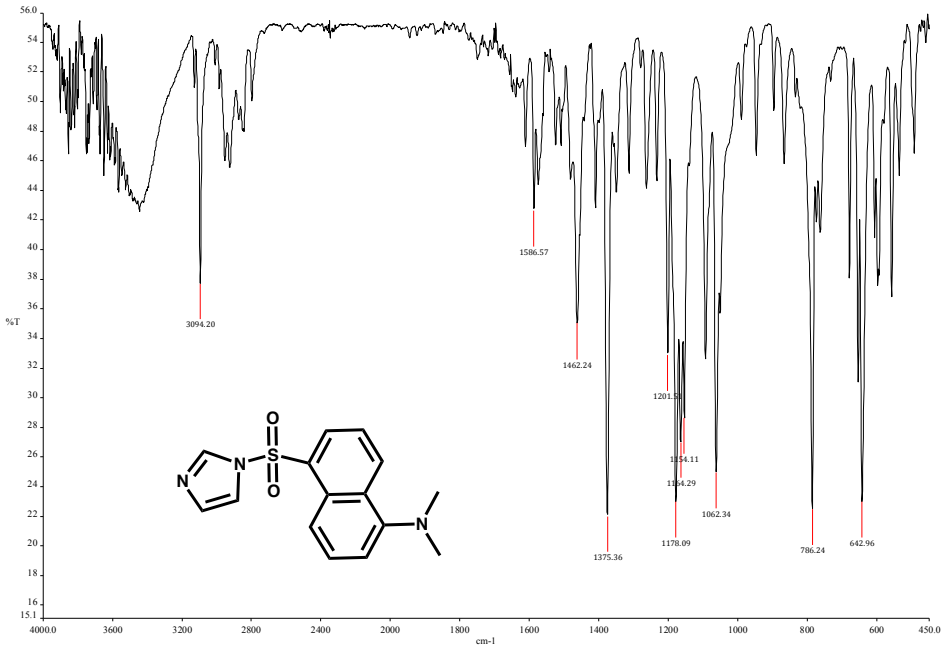

Figure B.11. IR spectrum of free ligand Im-Dansyl in KBr matrix.

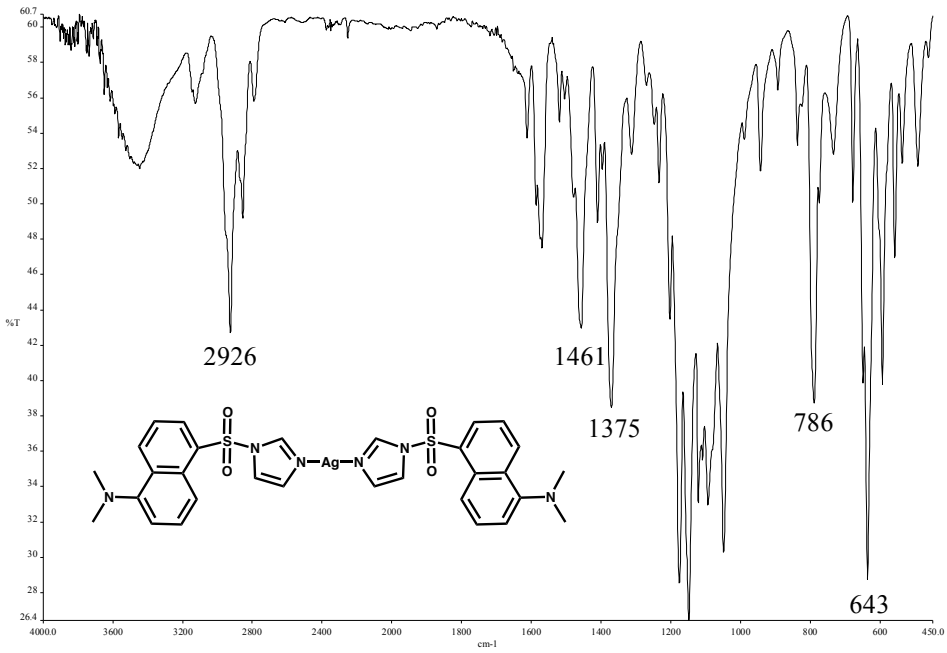

Figure B.12. IR spectrum of [Ag(ImD)]ClO_4 in KBr matrix.

B.1.8. References

1. Atiyeh, B.S.; Costagliola, M.; Kayek, S.N.; Dibo, S.A., *Burns*. **2007**, *33*, 139-148.
2. Lansdown, A.B., *J. Wound Care*, **2002**; *11*, 125-130.
3. Klasen, H.J., *Burns*, **2000**; *26*, 131-138.
4. Levy, S.B. and Marshall, B., *Nature Med*., **2004**, *10*, S122-S192.
5. Arias, C.A. and Murray B.E., *N. Engl. J. Med*., **2009**, *360*, 439-443.
6. Walsh C. Antibiotics: Actions, Origins, Resistance, **2003**, ASM Press
7. Marambio-Jones, C. and Hoek, E.M.V., *J. Nanopart. Res.*, **2010**, 12, 1531-1551.
8. Silver, S.; Phung, L.T.; Silver, G., *J. Int. Microbiol. Biotechnol*., **2006**; *33*, 627-34.
9. Martin P. *Science*. **1997**; *276*, 75-81.
10. Diegelmann, R.F.; Evans, M.C., *Front. Biosci.*, **2004**, *9*, 283-89.
11. Velnar, T.; Mailey, T.; Smrkolj, V., *J. Int. Med. Res.*, **2009**, *37*, 1528-42.
12. Field, C.K.; Kerstein, M.D., *Am J Surg.*, **1994**, *167*, 2S-6S.
13. Winter, G.D.; Scales, J.T., *Nature*. **1963**, *197*, 91-92.
14. Rai, M.; Yadav, A.; Gade, A., *Biotechnol Adv*., **2009**, *27*, 76-83.
15. Rowan, R.; Tallon, R.; Sheahan, A.M.; Curran, R.; McCann, M.; Kavangh, K.; Devereux, M.; McKee, V., *Polyhedron*, **2006**, *25*, 1771-1778.
16. Melaiye A, Sun Z, Hindi K, Milsted A, Ely D, Reneker D.H., Terrier CA, Youngs WJ., *J. Am. Chem. Soc.*, **2005**,*127*, 2285-2291.

17. Gray, W.R., *Method. Enzymol.,* **1967**, *11*, 139-51.

18. Ramli, N.A.; Wong, T.W., *Int. J. Pharm.*, **2011**, *403*, 73-82.

19. Hoffman, A.S., *Adv. Drug Deliver. Rev.*, **2002**, *54*, 3-12.

20. Peppas, N.A.; Torres-Lugo, M.; Lowman, A.M., *J. Control. Release.*, **1999**, *62*, 81-87.

21. Sannino, A.; Demitri, C.; Madaghiele, M., *Materials*. **2009**, *2*, 353-73.

22. Nomiya,, K.; Takahashi, S.; Noguchi, R.; Nemoto, S.; Takayama, T.; Oda, M., *Inorg. Chem*., **2000**, *39*, 3301-11.

23. Abu-Youssef MAM, Dey R, Gohar Y, Massoud AA, Öhrström MA, Lander V., *Inorg. Chem.*, **2007**, *46*, 5893-5903.

24. Chernousova, S.; Epple, M., *Angew. Chem. Int. Ed.*, **2013**, *52*, 1636-53.

25. Fayaz, A.M.; Balaji, K.; Gitilal, M.; Yadav, R.; Kalaichelvan, P.T.; Venketsan, R., *Nanomed-Nanotechnol.*, **2010**, *6*, 103-109.

26. Heilman, B.J.; Halpenny, G.M.; Mascharak, P.K., *J. Biomed. Mater. Res. B.*, **2011**, *99B*, 328-337.